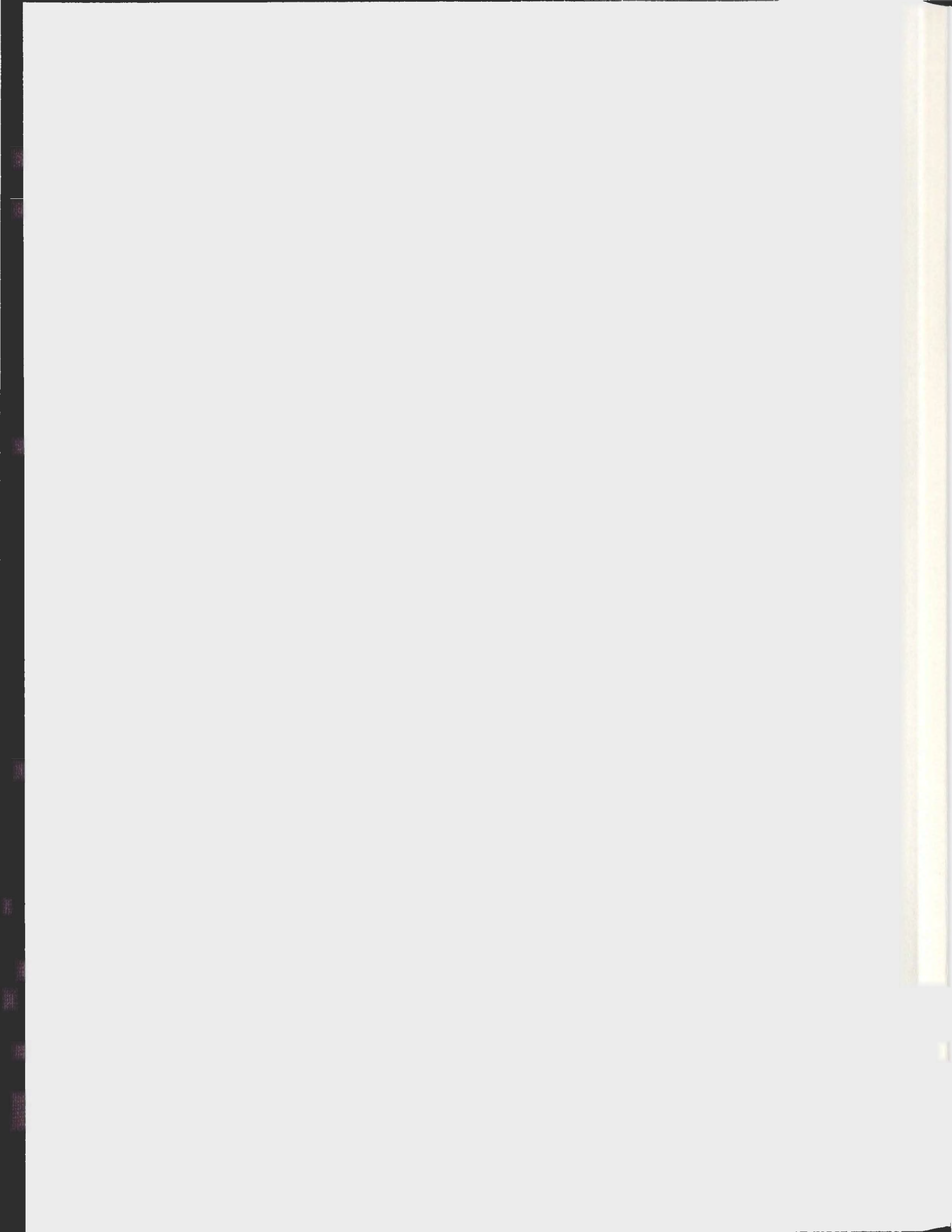


A FIRST LOOK AT SKEWNESS IN THE LABRADOR  
SEA WATER MASSES

J.L. McLARTY







**A First Look at Skewness in the Labrador Sea Water Masses**

by

© J. L. McLarty  
B.Sc (Physics, Mathematics)

A thesis submitted to the  
School of Graduate Studies  
in partial fulfillment of the  
requirements for the degree of  
Master of Science.

Department of Physics and Physical Oceanography  
Memorial University of Newfoundland

Aug 5th 2008

ST. JOHN'S

NEWFOUNDLAND

# Abstract

Hydrographic data from 1938 to 2006 in the Labrador Sea is used to calculate the geographical distribution of standard deviation ( $\delta$ ) and moment coefficient of skewness ( $\gamma_3$ ) of the salinity ( $S$ ) anomaly, potential temperature ( $\theta$ ) anomaly, and potential density anomaly ( $\sigma_\theta$ ) fields of the six major water masses. After removing the mean monthly signal, the data statistics are calculated in 22 separate regions and respectively defined at the region centres, thereby allowing us to interpolate the data to a  $0.5^\circ \times 0.5^\circ$  grid in the Labrador Sea for each water mass. While the  $\delta$  maps describe the geographical distribution of variability at all scales, we show that the skewness of the low-frequency  $S$  and  $\theta$  fields can be used to distinguish the mesoscale variability; mixing of  $\theta - S$  characteristics in the classic Labrador Sea processes are prominent in the  $S$  and  $\theta$  skewness maps. Sensitivity of skewness to the long-term variability is tested by calculating the  $\delta$  and  $\gamma_3$  maps for four shorter time periods: 1938-1984 and 1985-2006 in which sea-water properties are subject to different long-term variability (compared to 1938-2006), and 1963-1973 and 1989-1999 in which sea-water properties are nearly homogeneous. Although statistically insignificant skew dominates the distributions in 1963-1973 and 1989-1999, the results show remarkable similarity between the five  $\gamma_3(S)$  and  $\gamma_3(\theta)$  maps of the surface layer, Irminger Water layer, shallow Labrador Sea Water layer, and to some extent the deep Labrador Sea Water layer. We conclude the geographical distribution of  $S$  and  $\theta$  skewness does distinguish

the mesoscale variability in the Labrador Sea and likely does not exhibit interannual variability.

# Acknowledgements

I graciously thank my supervisors, Entcho Demirov and Brad de Young, who have made this thesis and experience possible. To old friends, new friends and family for all the quality time: Sara, Aaron, Brad, Greg, Rachel, Nicole, Charlie, Rob, Tristan, Dave, Lindsay, Graig, Jim, Will, Peng, Mom, Jim, Billie, Dad, little Ayla, and the rest.

# Contents

<b>Abstract</b>	<b>ii</b>
<b>Acknowledgements</b>	<b>iv</b>
<b>List of Tables</b>	<b>x</b>
<b>List of Figures</b>	<b>xvi</b>
<b>Acronyms</b>	<b>xvii</b>
<b>1 Ocean Processes and Variability in the Labrador Sea</b>	<b>1</b>
1.1 Labrador Sea Characteristics . . . . .	2
1.1.1 Geography . . . . .	2
1.1.2 Seasonal Variability . . . . .	3
1.2 The Convective Processes . . . . .	4
1.2.1 Surface layer thermohaline fluxes . . . . .	4
1.2.2 Subsurface thermohaline fluxes . . . . .	6
1.2.3 Labrador Sea Water . . . . .	7
1.3 The North Atlantic Oscillation Connection . . . . .	9
1.4 Outline of the Thesis . . . . .	10

<b>2</b>	<b>Data and Methodology</b>	<b>11</b>
2.1	The Data . . . . .	11
2.2	Defining the Regions of Analysis . . . . .	12
2.3	The Water Masses . . . . .	13
2.3.1	IW . . . . .	15
2.3.2	LSW . . . . .	15
2.3.3	Bottom Water Masses . . . . .	16
2.4	Removing the Mean Signal . . . . .	17
2.5	Anomaly Distributions . . . . .	17
2.5.1	Central Moments . . . . .	19
2.5.2	Moment coefficient of skewness . . . . .	19
2.5.3	Statistical significance of skewness . . . . .	20
2.6	Data Gridding . . . . .	20
<b>3</b>	<b>Statistics of the Hydrography: 1938-2006</b>	<b>21</b>
3.1	Water Mass Variability . . . . .	21
3.1.1	Surface Layer . . . . .	22
3.1.2	IW layer . . . . .	25
3.1.3	sLSW Layer . . . . .	26
3.1.4	dLSW Layer . . . . .	27
3.1.5	Bottom Water Masses . . . . .	28
3.2	Water Mass Skewness . . . . .	29
3.2.1	Surface Layer . . . . .	30
3.2.2	Intermediate Water Masses . . . . .	34
3.2.3	Bottom Water Masses . . . . .	36
3.3	Anomaly Probability Density Distributions . . . . .	38

3.3.1	$\chi^2$ test . . . . .	38
3.3.2	The Distributions . . . . .	39
3.4	Summary . . . . .	41
<b>4</b>	<b>Sensitivity of Skewness</b>	<b>45</b>
4.1	Regime Shift: 1938-1984 and 1985-2006 . . . . .	46
4.1.1	TS Diagrams . . . . .	47
4.1.2	Inference for the Difference between the Mean States . . . . .	49
4.2	Regime Shift: 1963-1973 and 1989-1999 . . . . .	50
4.3	Changes in Water Mass Variability . . . . .	51
4.3.1	Surface layer . . . . .	51
4.3.2	Intermediate layers . . . . .	52
4.3.3	Bottom water masses . . . . .	53
4.4	Changes in Water Mass Skewness . . . . .	53
4.4.1	Limitations to the Analysis . . . . .	54
4.4.2	Surface layer . . . . .	54
4.4.3	IW layer . . . . .	55
4.4.4	sLSW and dLSW layers . . . . .	56
4.5	Summary . . . . .	57
<b>5</b>	<b>Discussion and Conclusions</b>	<b>59</b>
5.1	Summary of Variability and Skewness . . . . .	59
5.2	Future Work and Recommendations . . . . .	61
5.3	Implications of the Project . . . . .	62
	<b>Bibliography</b>	<b>63</b>
	<b>Appendices</b>	<b>66</b>

<b>Appendix A: Probability Density Distributions</b>	<b>67</b>
<b>Appendix B: TS Diagrams</b>	<b>74</b>
<b>Appendix C: Standard Deviation of Anomalies</b>	<b>84</b>
<b>Appendix D: Skewness of Anomalies</b>	<b>93</b>

# List of Tables

2.1	The defined isopycnal boundaries of the surface, Irminger Water (IW), shallow Labrador Sea Water (sLSW), deep Labrador Sea Water (dLSW), Iceland-Scotland Overflow Water (ISOW) and Denmark Strait Overflow Water (DSOW) layers. . . . .	15
3.1	Maximum and minimum standard deviations of $S$ , $\theta$ and $\sigma_\theta$ corresponding to the normalized standard deviation extrema. . . . .	30
3.2	Maximum and minimum skewness of $S$ , $\theta$ and $\sigma_\theta$ corresponding to the normalized coefficient of skewness extrema. . . . .	37
.1	Maximum and minimum 1963-1973 and 1989-1999 standard deviation of $S$ , $\theta$ and $\sigma_\theta$ anomalies corresponding to the normalized standard deviation extrema. . . . .	91
.2	Maximum and minimum 1938-1984 and 1985-2006 standard deviation of $S$ , $\theta$ and $\sigma_\theta$ anomalies corresponding to the normalized standard deviation extrema. . . . .	92
.1	Maximum and minimum 1963-1973 and 1989-1999 skewness of $S$ , $\theta$ and $\sigma_\theta$ anomalies corresponding to the normalized skewness extrema. . . . .	100

- .2 Maximum and minimum 1938-1984 and 1985-2006 skewness of  $S$ ,  $\theta$  and  $\sigma_\theta$  anomalies corresponding to the normalized skewness extrema. 100

# List of Figures

2.1	Horizontal locations of all hydrographic data. The 22 defined regions of analysis are outlined. Ocean Weather Station <i>BRAVO</i> is marked by the green square in region 14. . . . .	14
3.1	Standard deviation of surface layer, Irminger and shallow Labrador Sea water anomalies: 1938-2006 . . . . .	23
3.2	Standard deviation of deep Labrador Sea, Iceland-Scotland Overflow and Denmark Strait Overflow water anomalies: 1938-2006 . . . . .	24
3.3	Skewness of surface layer, Irminger and shallow Labrador Sea water anomalies: 1938-2006 . . . . .	31
3.4	Skewness of deep Labrador Sea, Iceland-Scotland Overflow and Denmark Strait Overflow water anomalies: 1938-2006 . . . . .	32
3.5	Histogram and kernel density estimates of surface layer salinity in the northern Labrador Sea . . . . .	40
3.6	Kernel density estimates of surface water $\theta$ in the Labrador Current and IW $\theta$ in the southeast Labrador Sea during 1963-1973, 1989-1999, 1938-1984, 1985-2006 and 1938-2006 . . . . .	42

4.1 Annual mean potential temperature and salinity distributions in the CLS for the subsurface water masses. +’s and □’s are annual means during 1938-1984 and 1985-2006 respectively. In 1942-47 and 1982 there is no data for all water masses while some water masses also do not have data in other years. . . . . 48

.1 Histograms (40 bins) of 1938-2006 surface layer salinity, potential temperature and potential density anomalies respectively for NLS (a,b,c), WGC (d,e,f), CLS (g,h,i), LC (j,k,l) and SELS (m,n,o). Anomalies have been normalized by the maximum amplitude prior to binning. Thick black curves are the normal distributions having the same means and standard deviations as the histograms. The *non-normalized* anomaly moments,  $\chi^2$  statistic and associated p-value are shown. . . 68

.2 Histograms (40 bins) of 1938-2006 Irminger water salinity, potential temperature and potential density anomalies respectively for NLS (a,b,c), WGC (d,e,f), CLS (g,h,i), LC (j,k,l) and SELS (m,n,o). Anomalies have been normalized by the maximum amplitude. Thick black curves are the normal distributions having the same means and standard deviations as the histograms. The *non-normalized* anomaly moments,  $\chi^2$  statistic and associated p-value are shown. . . . . 69

- .3 Histograms (40 bins) of 1938-2006 shallow Labrador Sea water salinity, potential temperature and potential density anomalies respectively for NLS (a,b,c), WGC (d,e,f), CLS (g,h,i), LC (j,k,l) and SELS (m,n,o). Anomalies have been normalized by the maximum amplitude. Thick black curves are the normal distributions having the same means and standard deviations as the histograms. The *non-normalized* anomaly moments,  $\chi^2$  statistic and associated p-value are shown. . . . . 70
- .4 Histograms (40 bins) of 1938-2006 deep Labrador Sea water salinity, potential temperature and potential density anomalies respectively for NLS (a,b,c), WGC (d,e,f), CLS (g,h,i), LC (j,k,l) and SELS (m,n,o). Anomalies have been normalized by the maximum amplitude. Thick black curves are the normal distributions having the same means and standard deviations as the histograms. The *non-normalized* anomaly moments,  $\chi^2$  statistic and associated p-value are shown. . . . . 71
- .5 Histograms (40 bins) of 1938-2006 Iceland-Scotland Overflow water salinity, potential temperature and potential density anomalies respectively for NLS (a,b,c), WGC (d,e,f), CLS (g,h,i), LC (j,k,l) and SELS (m,n,o). Anomalies have been normalized by the maximum amplitude. Thick black curves are the normal distributions having the same means and standard deviations as the histograms. The *non-normalized* anomaly moments,  $\chi^2$  statistic and associated p-value are shown. . . 72

.6	Histograms (40 bins) of 1938-2006 Denmark Strait Overflow water salinity, potential temperature and potential density anomalies respectively for NLS (a,b,c), WGC (d,e,f), CLS (g,h,i), LC (j,k,l) and SELS (m,n,o). Anomalies have been normalized by the maximum amplitude. Thick black curves are the normal distributions having the same means and standard deviations as the histograms. The <i>non-normalized</i> anomaly moments, $\chi^2$ statistic and associated p-value are shown. . . . .	73
.1	Surface layer annual mean potential temperature and salinity distribution in the CLS where +’s and □’s are annual means during 1938-84 and 1985-06 respectively. No data exists in 1942-47 and 1982. . . . .	75
.2	Surface layer annual mean potential temperature and salinity distribution in the WGC where +’s and □’s are annual means during 1938-84 and 1985-06 respectively. No data exists in 1939-45, 1976, 1978, and 1982-83. . . . .	76
.3	Annual mean potential temperature and salinity distributions in the WGC for the subsurface water masses. +’s and □’s are annual means during 1938-84 and 1985-06 respectively. In 1939-45, 1947, 1976 and 1982-83 there is no data for all water masses while some water masses also do not have data in other years. . . . .	77
.4	Surface layer annual mean potential temperature and salinity distribution in the NLS where +’s and □’s are annual means during 1938-84 and 1985-06 respectively. No data exists in 1939-45. . . . .	78

.5	Annual mean potential temperature and salinity distributions in the NLS for the subsurface water masses. +'s and □'s are annual means during 1938-84 and 1985-06 respectively. In 1939-45 and 1947 there is no data for all water masses while some water masses also do not have data in other years. . . . .	79
.6	Surface layer annual mean potential temperature and salinity distribution in the LC where +'s and □'s are annual means during 1938-84 and 1985-06 respectively. No data exists in 1942-45 and 1947. . . . .	80
.7	Annual mean potential temperature and salinity distributions in the LC for the subsurface water masses. +'s and □'s are annual means during 1938-84 and 1985-06 respectively. In 1939-45 and 1947 there is no data for all water masses while some water masses also do not have data in other years. . . . .	81
.8	Surface layer annual mean potential temperature and salinity distribution in the SELS where +'s and □'s are annual means during 1938-84 and 1985-06 respectively. No data exists in 1938-40, 1942-46, 1949 and 1975-76. . . . .	82
.9	Annual mean potential temperature and salinity distributions in the SELS for the subsurface water masses. +'s and □'s are annual means during 1938-84 and 1985-06 respectively. In 1938-46,1949 and 1975 there is no data for all water masses while some water masses also do not have data in other years. . . . .	83
.1	Standard deviation of surface layer anomalies: 1963-73, 1989-99, 1938-84 and 1985-06 . . . . .	85

.2	Standard deviation of Irminger water anomalies: 1963-73, 1989-99, 1938-84 and 1985-06 . . . . .	86
.3	Standard deviation of shallow Labrador Sea water anomalies: 1963-73, 1989-99, 1938-84 and 1985-06 . . . . .	87
.4	Standard deviation of deep Labrador Sea water anomalies: 1963-73, 1989-99, 1938-84 and 1985-06 . . . . .	88
.5	Standard deviation of Iceland-Scotland Overflow water anomalies: 1963- 73, 1989-99, 1938-84 and 1985-06 . . . . .	89
.6	Standard deviation of Denmark Strait Overflow water anomalies: 1963- 73, 1989-99, 1938-84 and 1985-06 . . . . .	90
.1	Skewness of surface layer anomalies: 1963-73, 1989-99, 1938-84 and 1985-06 . . . . .	94
.2	Skewness of Irminger water anomalies: 1963-73, 1989-99, 1938-84 and 1985-06 . . . . .	95
.3	Skewness of shallow Labrador Sea water anomalies: 1963-73, 1989-99, 1938-84 and 1985-06 . . . . .	96
.4	Skewness of deep Labrador Sea water anomalies: 1963-73, 1989-99, 1938-84 and 1985-06 . . . . .	97
.5	Skewness of Iceland-Scotland Overflow water anomalies: 1963-73, 1989- 99, 1938-84 and 1985-06 . . . . .	98
.6	Skewness of Denmark Strait Overflow water anomalies: 1963-73, 1989- 99, 1938-84 and 1985-06 . . . . .	99

# Acronyms

**AO** Arctic Oscillation

**BIO** Bedford Institute of Oceanography

**CLS** Central Labrador Sea

**DWBC** Deep Western Boundary Current

**dLSW** deep Labrador Sea Water

**DSOW** Denmark Strait Overflow Water

**GSA** Great Salinity Anomaly

**ISOW** Iceland-Scotland Overflow Water

**IW** Irminger Water

**LC** Labrador Current

**LS** Labrador Sea

**LSW** Labrador Sea Water

**NADW** North Atlantic Deep Water

**NAO** North Atlantic Oscillation

**NLS** Northern Labrador Sea

**OWSB** Ocean Weather Station *Bravo*

**P-ALACE** Profiling Autonomous Lagrangian Circulation Explorer

**PEA** Potential energy anomaly

**SELS** Southeast Labrador Sea

**sLSW** shallow Labrador Sea Water

**SST** Sea surface temperature

**WGC** West Greenland Current

# Chapter 1

## Ocean Processes and Variability in the Labrador Sea

Circulation and water formation within the Labrador Sea (LS) are major components of the thermohaline circulation in the North Atlantic. As part of the North Atlantic current system, heat from low latitudes is transported northward and released to the atmosphere in the subpolar convective regions during winter. The LS is a major site of subpolar convective overturning and sea-water densification where the unique mid-depth watermass known as Labrador Sea Water (LSW) is formed during winter [1] and exported out of the LS in three main transport pathways to the *(i)* subtropics, *(ii)* Irminger Sea and *(iii)* West European basin [2]. Since LSW is central to North Atlantic Deep Water (NADW) formation in the Irminger Sea and Nordic Seas, variability in the LSW formation rates and processes is key to understanding the role of the LS in the climate system.

## 1.1 Labrador Sea Characteristics

### 1.1.1 Geography

In the Northwest corner of the Atlantic Ocean, the Labrador Sea (LS) is annually subject to cold and wind extremes, intense air-sea interaction, and freshwater and ice transports from the Canadian Arctic Archipelago and shelf-ice. The coldest and freshest basin in the subpolar North Atlantic, it is unique in the ocean process leading to intermediate-deep water formation. The LS is a semi-enclosed basin with two major boundary currents formed by two cold, fresh inflows arriving from the Arctic Ocean via the Davis Strait and around the southern coast of Greenland.

These strong cyclonic boundary currents, known as the Labrador and West Greenland Currents, are mainly baroclinic with a large salinity gradient separating the saline sea-water over the basin and fresher coastal sea-water over the shelves. The West Greenland Current (WGC) diverges from the West Greenland Coast over the 1000 – 3000 m isobaths and deflects west and south at the mouth of Davis Strait becoming the offshore part of the Labrador Current (LC) over the continental slope in the western LS. Outflow from Davis Strait joins the deflected WGC and in the southward flow, forms the inshore part of the LC over the continental shelf. Interior to the boundary currents, the mean general flow is weak and cyclonic, although mean anticyclonic circulation has been measured at mid-depths ( $\sim 700$  m) [3, 4] by subsurface P-ALACE floats and SOLO floats. The strong cyclonic boundary flow and the mean weak cyclonic interior flow essentially trap surface waters in the Central Labrador Sea (CLS), causing isopycnals to 'dome up' to the surface, exposing underlying layers to intense winter-time cooling.

The strong north-westerly continental winds in the winter provide the favourable

conditions needed for deep water formation in the LS. In the winter, LS surface waters are exposed to the cold and dry winds blowing off the ice covered Canadian Arctic. Thermal and haline fluxes at the air-sea interface result in an average winter heat loss exceeding  $300 \text{ W m}^{-2}$  (with peak values exceeding  $1000 \text{ W m}^{-2}$  off the sea-ice edge along the Labrador Coast) [5], and net annual evaporation-precipitation estimated to range between  $-0.05 \text{ m yr}^{-1}$  [6] to  $-0.5 \text{ m yr}^{-1}$  [7].

### 1.1.2 Seasonal Variability

The seasonal cycle of temperature and salinity within the Labrador Sea is mostly contained in the surface layer [8, 9] while the interannual changes predominate the subsurface layers [10]. A study done by Straneo [10] using 1964-1974 Ocean Weather Station Bravo (OWSB) hydrographic data and 1996-2000 P-ALACE float data within the 3300-m isobath of the CLS reveals two distinct periods in the mean seasonal cycle of heat content and salinity. Beginning around January, both the surface layer and lower layers cool, reaching a minimum heat content near the end of March. During this time, the salt content increases in the surface layer and decreases in the lower layers. Domed isopycnals in the CLS are exposed to the cold and dry continental winds, thereby experiencing a buoyancy loss to the atmosphere and exposing subsurface waters to the cold evaporation. The heat content increases from April to September. A surface decrease and subsurface increase in salt content occurs from April to December. Heat lost to the atmosphere at the ocean surface during winter is replenished by a subsurface convergence of heat from surrounding subsurface waters and advected upward through the water column. With the convergence of heat in the lower layers is a subsurface influx of saltier boundary water from the subsurface WGC and a surface influx of fresher water from the surface boundary currents and

sea-ice transport.

## 1.2 The Convective Processes

The subpolar gyre circulation and extreme heat losses during January-April in the LS contributes to production of some of the densest and deepest mixed layers in the North Atlantic, excluding the Nordic Seas and Baffin Bay [11]. The convective process can be separated into three phases: preconditioning, deep convection and restratification. Cyclonic gyre circulation, weak stratification from previous convection, and atmospheric forcing predispose a site to convectively overturn. Subsequent cooling at the air-sea interface initiates overturning in numerous 'plumes' which distribute the dense surface water in the vertical to depths dependent on the amount of preconditioning and intensity of subsequent atmospheric forcing. As atmospheric forcing diminishes, the convected layers restratify through heat and salt exchanges between the basin and surrounding boundary waters. Following convection, the gyre circulation exports the water mass products from the LS.

### 1.2.1 Surface layer thermohaline fluxes

Freshwater is advected into the surface CLS from the fresh surface boundary currents from April through December, while the layer experiences warming from insolation (warming may also be from inflow of warmer water in the southeastern Labrador Sea throughout the year) from April to September. The mean freshwater gain in the surface layer is equivalent to  $\sim 0.5$  m of freshwater mixed throughout the entire water column [8].

The entire surface layer is influenced by the atmospheric boundary layer through heat and moisture exchange at the atmosphere-ocean interface. The cyclonic circu-

lation around the basin sets the initial "doming up" of the isopycnals toward the ocean surface. In the CLS, but typically near the 3000 m isobath off the Labrador Coast [12, 13, 14], the surface layer stratification tends to be weakened from previous convective events. With the exposure of the weakly stratified, 'domed' layers to the cold, dry arctic winds off the Canadian landmass, large air-sea temperature differences result. This combined wind and buoyancy forcing further uplifts the isopycnals exposing subsurface density classes not typically exposed to the atmosphere, inducing large upward heat and moisture fluxes between the air-sea interface.

In the CLS, heat gained during the spring and summer months is lost to the atmosphere from September to April and freshwater fluxed in from the boundary currents is evaporated from roughly January to March. The mean surface heat loss from recalibrated National Centers for Environmental Protection-National Center for Atmospheric Research (NCEP-NCAR) reanalysis fields is of  $0.891 \times 10^9 \text{ J m}^{-2}$  [10]. The net annual evaporation-precipitation is estimated to range between  $-0.05 \text{ m yr}^{-1}$  [6] to  $-0.5 \text{ m yr}^{-1}$  [7]. The preconditioning of the region is on the large scale ( $\sim 50 - 100 \text{ km}$ ) and so simultaneous overturning of the surface layer cannot occur. Alternatively, the convective layer is formed when the large buoyancy fluxes over the preconditioned region result in local density increases of water at the ocean surface. These local density increases overturn, forming numerous small scale plumes  $O(\sim 1 \text{ km})$  which distribute the buoyancy loss over depths of up to  $\sim 2300 \text{ m}$  [5]. To offset the buoyancy loss at the surface, subsurface water is drawn upward around the plumes and is subject to the same surface heat and moisture fluxes.

### 1.2.2 Subsurface thermohaline fluxes

As subsurface water is drawn upward, replacing local buoyancy losses, the heat and salt content in subsurface layers decrease [10]. Vigorous horizontal mixing between the plumes of convected water and subsurface water produce a unique, nearly homogeneous water mass [5]. Both during, and consequent to the vigorous mixing, the subsurface heat and salt loss must be balanced by lateral exchanges with the warmer, saltier surrounding subsurface boundary current waters. The combined effects of gravity and the Earth's rotation compress the plumes of dense convected water, generating strong horizontal circulation by eddying on geostrophic scales. Upon the weakening of the atmospheric forcing around late March, the initial restratification of CLS, is relatively rapid spanning approximately 1 month [15]. Restratification through heat and salt exchange between the convectively mixed water and the boundary current water is thought to be dictated by the strong lateral currents associated with the geostrophic eddies (on the scale of the baroclinic deformation radius,  $O(10 \text{ km})$ ). Relatively few observations of these mesoscale eddies exist, but some notable observations have been made [1, 15, 16, 17].

Anticyclonic eddies may be the sole products of deep convection whereas both cyclonic and anticyclonic eddies may be products from the Irminger and/or West Greenland Currents. Anticyclonic eddies carrying properties of  $\theta - S$  minima (convected water), measured near *OWS Bravo* several months after the cessation of convection, suggest they were formed during the deep convective season [15, 16]. These eddies somehow insulate the core water from the restratification process and the core depth seems to be damped by the underlying stratification [16]. The cyclonic eddies were observed to carry warm, saline waters similar to that in the Irminger boundary current with the extent of the core reaching about 2000 m, much deeper than the

anticyclonic counterparts. Gascard and Clarke [1] concluded that an eddy observed post-convection in 1976 with Labrador Sea Water properties (see Section 1.2.3) was formed in the rim current of the convective region through baroclinic instability. It has also been speculated [9] that boundary current dynamics may influence the depth of convection through the interannual variability of the lateral heat flux, eddy generation and eddy kinetic energy in the boundary currents. It was found [9] that a roughly 200 m decrease in the depth of convection coincided with a maximum lateral heat flux, and an increase in eddy event activity near a large spike in eddy kinetic energy.

More stunning evidence is given by [17] in which a sea surface temperature image shows both cyclonic and anticyclonic eddies ejected from the West Greenland boundary current into the interior Labrador Sea. These eddies may be the product of the counterrotating currents off the Greenland shelf and may act to annually restratify the interior. The sea surface height variability here has a strong seasonal dependence with maximum levels between January to March [17]. If the variability depends on the eddy formation then the eddies will be ejected into the interior during the convective period. The transport of heat by the ejected eddies, which carry mixtures of Irminger water, is likely significant. Lilly *et al.* [9] estimated a contribution of  $18 \text{ MJ m}^{-2}$  to the Labrador Sea from just a single 20 km radius eddy. Although these 'Irminger eddies' appear to be important to the annual heat cycle, the frequency of the eddy formation has not yet been determined.

### 1.2.3 Labrador Sea Water

The plumes of convected water vigorously mix the water column producing a unique water mass whose water properties depend upon the depth the convective process

annually reaches. On a quasi-continuous basis, convective mixing reaches appropriate depths producing the unique intermediate water mass, commonly called Labrador Sea Water (LSW). As the convective depth varies, it is frequently useful and common practice to separate this water mass into upper Labrador Sea Water (uLSW) and deep Labrador Sea Water (dLSW) [18, 15, 14]. Interannually, the convective depth reaches sLSW potential density ( $\sigma_\theta$ ) classes and on a longer-term basis, the convective depth reaches dLSW  $\sigma_\theta$  classes. Several definitions exist for the sLSW and dLSW  $\sigma_\theta$  classes:  $27.68 < \sigma_\theta < 27.74$  [14],  $27.68 < \sigma_\theta < 27.72$  [18], and  $27.7 < \sigma_\theta < 27.77$  [15] have been used for sLSW and  $27.74 < \sigma_\theta < 27.80$  [14],  $27.72 < \sigma_\theta < 27.78$  [18], and  $27.77 < \sigma_\theta < 27.80$  [15] for dLSW. Recently, studies of LSW separate the water mass based upon the time period in which it was formed [11], such that each class can be classified and traced based upon its unique combination of sea-water properties as determined by its formation period.

After formation of LSW and restratification, the subsequent slower process of removal of the LSW through entrainment into the LC typically continues until new LSW is convectively formed. The three classical pathways of LSW export out of the LS basin initially presented by Talley and McCartney (1982) remain unchanged, however, recent studies [3, 4] indicate a new export pathway. The three classic exit routes [2] all branch off the LC near the Flemish Cap and flow: (1) eastward, entraining into the deep North Atlantic Current which splits into a part that passes into the Irminger Sea and a part that passes into the West European Basin after crossing the mid-Atlantic Ridge, (2) southward, after entrainment into the deep North Atlantic Current, some LSW flow is lost to the subtropics, and (3) southward, where LSW not entrained into the deep North Atlantic Current flows west around Grand Banks and into the subtropics. Talley and McCartney did find evidence suggesting some LSW circulated directly into the Irminger Sea from the convection area. This was recently

confirmed by Lavender *et al.* [3, 4], through discovery of a mean anticyclonic flow at mid-depths near  $\sim 700$  m.

### 1.3 The North Atlantic Oscillation Connection

Climate variability over the Labrador Sea region is largely dominated by the North Atlantic Oscillation (NAO), a regional representation of the Arctic Oscillation (AO). The NAO index typically defines the difference in normalized mean winter sea level pressure (SLP) between the anomalous Icelandic low and Azores high. A large pressure difference is equivalent to a high index, indicating above average strong westerly winds over the Labrador Sea while a decrease in intense winter conditions is indicative of a small pressure difference.

Intense deep convection is observed in winters corresponding to a high NAO index [5, 12, 19, 20]. The influence of the NAO index on the underlying ocean is seen in sea surface temperature (SST), surface heat fluxes, freshwater fluxes and surface stress changes. An increase in wind stress, and therefore an increase in latent and sensible heat flux is associated with a positive NAO index [19]. Depending upon the intensity of atmospheric forcing [12] deep convection ventilates the subsurface layers down to the dLSW, changing the vertical density structure and heat content of the CLS water column. These changes are manifested in the distribution of the potential energy anomalies (PEAs). A study by Curry and McCartney [21] shows correlation between the variability of the NAO and the circulation of the North Atlantic gyre. They construct a PEA based mass transport index between the North Atlantic sub-polar and subtropical gyres, an oceanic analogue to the SLP based NAO index, and find indication of the ocean transport signal reflecting the NAO. An increase in mass transport in the North Atlantic gyre beginning in the early 1980s seems to coincide

with the persistent positive NAO index through to 1995 but with a lag of roughly 1-2 years [21].

## 1.4 Outline of the Thesis

The data set and methodology used to provide the spatial distribution of variability and skewness in the hydrography of the Labrador Sea are described in Chapter 2. Using the standard deviation maps, skewness maps and frequency distributions of salinity, potential temperature and potential density, in Chapter 3 we preliminarily characterize the statistical state of the water mass properties during the entire hydrographic record. Chapter 4 provides evidence of independence between skewness and long-term variability. We summarize and discuss the implications of the results of this study in Chapter 5.

## Chapter 2

# Data and Methodology

The goal of this study is to document the geographical distribution of skewness in the hydrography of the Labrador Sea using the entire 1938-2006 hydrographic record of data. The data and their sources are described in Section 2.1. In Section 2.2, we justify separating the hydrographic data geographically by defining 22 separate regions for the analysis. In Section 2.3, we justify separating the data vertically by defining isopycnal boundaries of the six main water masses found in the Labrador Sea. The variability of the 1938-2006 record requires removal of its high frequency component. The method of removing the mean seasonal signal is described in Section 2.4 and in Section 2.5, we discuss the use of the resulting anomaly distributions and their statistical moments. The interpolation method to produce geographical maps of standard deviation and skewness is described in Section 2.6.

### 2.1 The Data

The dataset is derived from the Ocean Science Hydrographic Climate Database (Climate) maintained by the Bedford Institute of Oceanography (BIO; <http://www.mar.dfo->

[mpo.gc.ca/science/ocean/database/doc2006/clim2006app.html](http://mpo.gc.ca/science/ocean/database/doc2006/clim2006app.html)). Data sources include expendable, digital or mechanical bathythermographs, profiling floats, CTD casts, hydrographic bottles, and spatially and temporally averaged Batfish tows. All archived data have been subject to quality control tests by both the Marine Environmental Data Service (MEDS) and the BIO after an initial validation is performed by the originating organization (see above website for details). The spatial distribution of the chosen data from 1938-2006 is shown in Figure 2.1. We study the depth-independent hydrographic properties, salinity ( $S$ ), potential temperature ( $\theta$ ) and potential density ( $\sigma_\theta$ ) of water masses found in this region.

## 2.2 Defining the Regions of Analysis

The data is partitioned into 22 regions of varying size (Fig. 2.1). By defining these individual regions we attempt to account for the different processes and mean physical characteristics within the regions. In the analysis and discussion to follow, it will be useful to define five larger regions comprising the 22 smaller regions. These regions are the northern Labrador Sea (NLS; regions 1, 2, 3, 4), the West Greenland Current (WGC; regions 5, 10), the Central Labrador Sea (CLS; regions 7, 8, 9, 13, 14), the Labrador Current (LC; regions 6, 12, 15, 18, 19, 20) and the Southeastern Labrador Sea (SELS; regions 11, 16, 17, 21, 22).

Separation between coastal and open ocean waters is necessary due to coastal ice and boundary currents. An anticyclonic circulation has been observed at  $\sim 700$  m in the interior of the Labrador basin as opposed to the outermost general cyclonic boundary current flow [3, 4]. This clockwise flow is located in regions 8, 9 and 11 and the northwest corner of region 13. Region 11 was to be included in the WGC originally, but the observed anticyclonic flow led us to include region 11 in the SELS

instead where we see no dominant flow regime based upon the objectively mapped mean circulation at 700 m depth in [3, 4].

## 2.3 The Water Masses

In oceanography, water masses are characterized by their unique combinations of physical properties. Permanent contact between the ocean surface and atmosphere leads to non-conservative sea-water properties in the ocean surface layer. Subject to the continuous wind forcing, heat and moisture fluxes at the air-sea interface it is often referred to as the surface mixed layer. Below this layer, sea-water temperature and salinity can only be changed by mixing and by advection with surrounding sea-water. Temperature and salinity are therefore treated as conservative properties allowing water masses below the surface mixed layer (hereinafter called the surface layer) to be identified by their temperature-salinity ( $T - S$ ) characteristics. Water mass classification is used to emphasize the geographic location, geographic origin or depth of the sea-water. As water masses display different characteristics in different parts of the global ocean and at different times, a given definition of a water mass is therefore ambiguous.

There are six main water masses in the Labrador Sea, surface water, Irminger Water (IW), shallow Labrador Sea Water (sLSW), deep Labrador Sea Water (dLSW), Iceland-Scotland Overflow Water (ISOW) and Denmark Strait Overflow Water (DSOW). In this study, the six water masses are defined by the chosen isopycnal boundaries in Table 2.1. The isopycnal boundaries of IW, sLSW and dLSW are the boundaries used by [15], whereas the ISOW and DSOW boundaries are drawn from the study by [14].

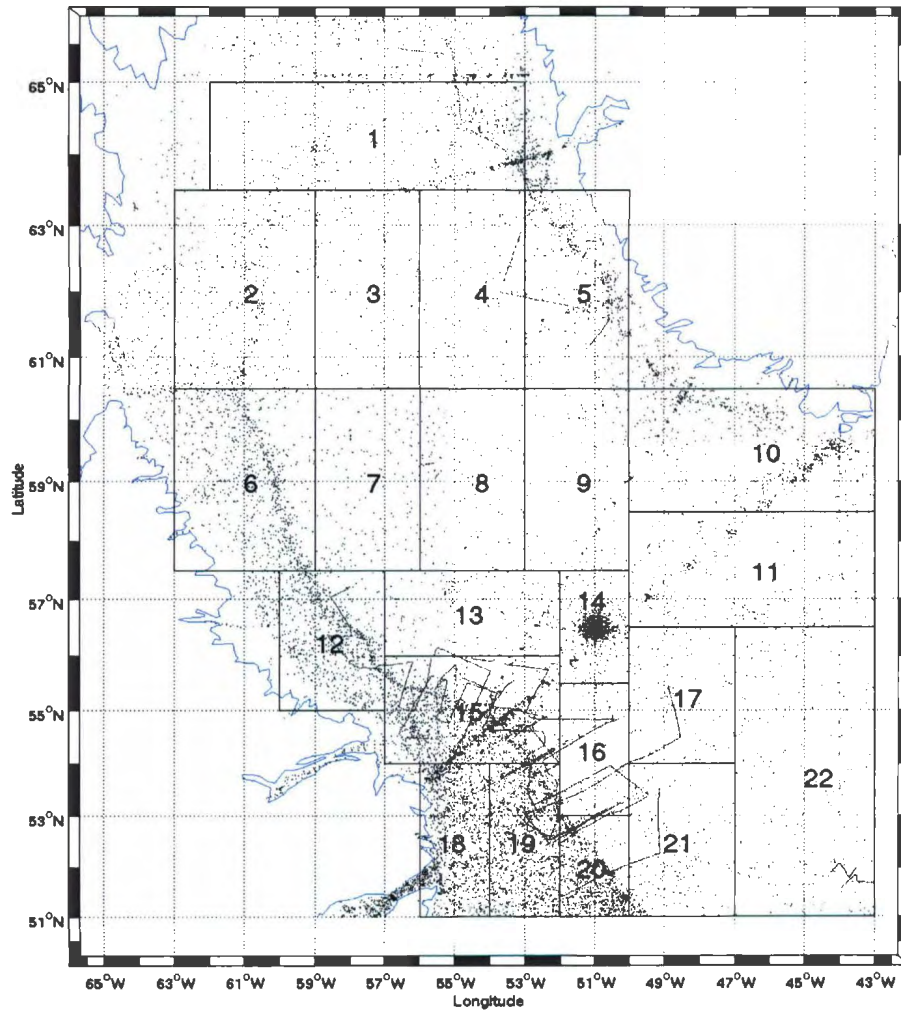


Figure 2.1. Horizontal locations of all hydrographic data. The 22 defined regions of analysis are outlined. Ocean Weather Station *BRAVO* is marked by the green square in region 14.

Water mass	$\sigma_\theta$ boundaries ( $\text{kg m}^{-3}$ )
Surface	$< 27.60$
IW	$27.60 - 27.70$
sLSW	$27.70 - 27.77$
dLSW	$27.77 - 27.80$
ISOW	$27.80 - 27.88$
DSOW	$> 27.88$

Table 2.1. The defined isopycnal boundaries of the surface, Irminger Water (IW), shallow Labrador Sea Water (sLSW), deep Labrador Sea Water (dLSW), Iceland-Scotland Overflow Water (ISOW) and Denmark Strait Overflow Water (DSOW) layers.

### 2.3.1 IW

Inflow from the Irminger Sea at mid-depths in the WGC is typically called Irminger Water (IW). It is characterized as warm and saline ( $\sim 4^\circ\text{C}$ ,  $\sim 34.95$  psu) water of subtropical origin. Typically, as in [15], it is classified as having potential densities,  $\sigma_\theta = 27.6-27.7 \text{ kg m}^{-3}$  (sea-water having potential densities less than 27.6 is classified as surface layer water).

### 2.3.2 LSW

Out of the six water masses, sLSW and dLSW are the only water masses whose entire production and transformation occurs in the Labrador Sea. Convectively formed water is readily identified as it colder and fresher than the surrounding water. Following the deepest convective mixing ever observed in the entire hydrographic record during

1990-1993, the LSW that was formed during this time had a core density of  $27.77 \text{ kg m}^{-3}$ , an approximate divider between shallow and deep LSW, in May 1994 [15]. These isopycnal boundaries are chosen in this study since they define the water product of the most vigorous deep convection ever observed in the LS. Due to variability in the convective depth during 1938-2006, however, different bounding isopycnals could have been chosen for different time periods, corresponding to the depths of convection.

### 2.3.3 Bottom Water Masses

The ISOW and DSOW respectively form the principal deep and bottom water masses of the subpolar North Atlantic ocean. Cold and fresh, ISOW enters the North Atlantic through the deep trenches in the Iceland-Scotland Ridge and increases in heat and salt content as it enters the LS, circulates the basin and exits in the southeast corner near the Flemish Cap. In the LS, the transformed ISOW, also known as Northeast Atlantic Deep Water and Charlie Gibbs Fracture Zone Water [22], is typically  $\sim 3^\circ\text{C}$  warmer and 0.02 saltier than the overflow entering the North Atlantic [23]. Having a salinity maximum, the bounding isopycnals of ISOW are  $27.80 - 27.88 \text{ kg m}^{-3}$ . Beneath the ISOW is the colder and fresher recirculated Atlantic Water, DSOW. This deepest water mass flows northward in the Atlantic Ocean, sinks to the bottom after passing Denmark Strait, and flows along eastern Greenland mixing with products of deep convection in the Iceland and Greenland Seas [24]. Forming the deepest LS boundary current, DSOW enters the LS along the southern tip of Greenland and exits the LS near the Flemish Cap.

## 2.4 Removing the Mean Signal

We are interested in skewness, a statistical descriptor, of the 1938-2006 hydrographic data set in the LS. The different scales of variability within this dataset all contribute to the observed signal that the data describe in space and time. We wish to remove the high frequency noise in the data, such that the lower-frequency (longer-term) variability in the data is better described. The high frequency signal is the hydrographic seasonal cycle discussed in Section 1.2, having a maximum amplitude in the surface layer which monotonically decreases over the subsurface layers. Additionally, the seasonal signal differs over the 22 regions since processes, and variability of the processes, differ from region to region. As such, in each water mass, the seasonal cycles of  $S$ ,  $\theta$  and  $\sigma_\theta$  must be removed correspondingly for each region.

Separating the data into the defined regions and water masses, the monthly means of the hydrographic properties ( $x$ ) are calculated and removed from the corresponding data. The hydrographic property anomaly ( $\hat{x}$ ) is the remaining signal. Thus the  $x$  anomaly is defined as

$$\hat{x} = \sum_{j=1}^{12} \left[ x^j - \frac{1}{N_j} \sum_{i=1}^{N_j} x_i^j \right] \quad (2.1)$$

where  $N_j$  is the total number of  $x^j$  data in the  $j$ th month (and in the respective region and water mass). Hereinafter, all discussion about the hydrographic properties are about the hydrographic property anomalies and any reference to the original hydrographic data will be explicit.

## 2.5 Anomaly Distributions

Normally distributed oceanographic data is a typical approximation in observational and modeling studies. This requires two fundamental assumptions:

1. The oceanographic data is a sufficiently large sample size<sup>1</sup>, in which the observations are independent and identically distributed. In theory, the distribution of the data sample tends toward normality as the sample size tends to infinity. In addition, each oceanographic measurement has a small, additive, stochastic component, independent of the other measurements.
2. The governing dynamical systems of the ocean processes are linear. By approximating a given distribution of oceanographic data as normal, it is assumed that positive and negative anomalies of any given amplitude occur with comparable frequency. This assumption also implicitly constrains distributions to another assumption regarding the geographical representation of distributions: that except for a reversal in polarity, a positive and negative anomaly at a given geographic location are associated with the same spatial structure. Normality in the oceanographic data is valid provided the anomalies describe a linear dynamical system in which the frequency distributions of the long-term (interannual and decadal) forcings are symmetric about the climatological mean forcing. This is of course a completely false assumption; the underlying physical ocean processes dictating the distributions of the observed anomalies, both geographically and temporally, are non-linear with interacting scales.

While mathematically it is convenient to assume normality for theoretical studies and statistical significance tests, observationally it is impractical if one is interested in understanding the stochastic dynamics inherent in the ocean, atmosphere and climate system. What is of interest, are the departures from a symmetric frequency distribution both geographically and temporally, which are exhibited by the statistics of the observed anomalies.

---

<sup>1</sup>Chebyshev's Theorem

### 2.5.1 Central Moments

We seek to statistically describe the hydrographic data in terms of the 3rd central moments of  $S$ ,  $\theta$  and  $\sigma_\theta$ . The  $k$ th central moment of the hydrographic property ( $x$ ) about its mean is given by

$$\mu_k(x) = \frac{1}{N} \sum_{i=1}^N (x_i - \bar{x})^k \quad (2.2)$$

where  $x_i$  is the  $i$ th observation,  $\bar{x}$  is the mean and  $N$  is the number of observations (in a region and water mass). Clearly, since  $S$ ,  $\theta$  and  $\sigma_\theta$  are now described in terms of their respective anomalies,  $\bar{S} = \bar{\theta} = \bar{\sigma}_\theta = 0$  with respect to 1938-2006. The central moments are therefore simply

$$\mu_k(x) = \frac{1}{N} \sum_{i=1}^N x_i^k. \quad (2.3)$$

The standard deviation of  $x$  is

$$\delta(x) = \mu_k^{1/2}(x) \quad (2.4)$$

and the skewness of  $x$  is

$$\mu_3(x) = \frac{1}{N} \sum_{i=1}^N x_i^3. \quad (2.5)$$

### 2.5.2 Moment coefficient of skewness

Skewness is a measure of the asymmetry of a frequency distribution about its mean value. If a distribution has an elongated tail of values greater than the mean, the distribution is said to be positively skewed. A distribution with an elongated tail of values less than the mean is negatively skewed. A normal distribution has zero skew.

We study skewness in the data using the moment coefficient of skewness (hereinafter referred to as skewness). It is defined as the normalized 3rd central moment

$$\gamma_3(x) = \frac{\mu_3(x)}{\delta(x)^3}, \quad (2.6)$$

where  $\mu_3(x)$  is the 3rd central moment of  $x$  and  $\delta(x)$  is the standard deviation of  $x$  as defined in Section 2.4.1.

### 2.5.3 Statistical significance of skewness

The standard error of moment coefficient of skewness is

$$SE = \left(\frac{6}{N}\right)^{1/2} \quad (2.7)$$

for large  $N$  [25]. The number of observations  $N$  are assumed to be statistically independent. The 95% confidence level of  $\gamma_3$  is twice the standard error. Skewness values outside the 95% confidence level are statistically significantly different from that of a normal distribution with  $N$  independent observations. Therefore skewness values falling within the 95% confidence bounds are not significantly different from zero.

## 2.6 Data Gridding

To obtain geographical maps of water mass  $S$ ,  $\theta$  and  $\sigma_\theta$  standard deviation and skewness, the calculated  $\delta$  and  $\gamma_3$  values in each region are interpolated to a uniform, horizontal grid of the Labrador Sea. The grid is a  $0.5^\circ \times 0.5^\circ$  grid with boundaries  $51^\circ$ - $65^\circ$ N,  $43^\circ$ - $63^\circ$ W. At the latitude and longitude of the region centers, the respective  $\delta$  and  $\gamma_3$  values are defined. These 22  $\delta$  and  $\gamma_3$  values and 22 grid points are interpolated to the  $0.5^\circ \times 0.5^\circ$  grid using a cubic Delauney triangulation gridding scheme<sup>2</sup>.

---

<sup>2</sup>interpolation of the data using the MatLab gridding function specifying the cubic Delauney triangulation method

## Chapter 3

# Statistics of the Hydrography: 1938-2006

This chapter provides a preliminary characterization of the statistical state of water mass properties during the entire hydrographic record in the Labrador Sea. The geographical distribution of the second and third moments of the salinity ( $S$ ), potential temperature ( $\theta$ ) and potential density ( $\sigma_\theta$ ) anomalies are given in Sections 3.1 and 3.2. In Section 3.3, normality of the anomalies is tested using the  $\chi^2$  distribution, resulting in non-Gaussian  $S$ ,  $\theta$  and  $\sigma_\theta$  probability distributions throughout the Labrador Sea. Section 3.4 summarizes the resulting statistics of water mass properties.

### 3.1 Water Mass Variability

The geographical distribution of standard deviation illustrates regions subject to strong variability. The standard deviation ( $\delta$ ) of salinity, potential temperature and potential density anomalies for surface water, Irminger water (IW) and shallow Labrador Sea water (sLSW) are mapped in Figure 3.1 and for deep Labrador Sea

water (dLSW), Iceland-Scotland Overflow water (ISOW) and Denmark Strait Overflow water (DSOW) in Figure 3.2. Each  $\delta$  map has been normalized by its respective maximum. Table 3.1 gives the actual  $\delta$  maxima and minima corresponding to the normalized extrema of 0 and 1 for each water mass. Since  $\delta$  is calculated from anomalies for 1938-2006, the  $\delta$  maps show regions having prominent interannual, decadal and mesoscale variability (hereinafter, variability is the combination of interannual, decadal and mesoscale variability unless stated otherwise).

### 3.1.1 Surface Layer

The entire surface layer of the ocean is subject to the long-term variability of dynamic and thermodynamic properties in the atmospheric boundary layer through heat and moisture exchanges at the atmosphere-ocean interface. While fluxes between the atmosphere and ocean impact the  $S$  and  $\theta$  of the entire surface layer, other processes may have a greater influence at the periphery of the Labrador Sea. Figures 3.1(a-c) show that surface  $S$  and  $\sigma_\theta$  variability is greatest in the boundary currents, whereas surface variability in  $\theta$  is strongest in the northern and southern Labrador Sea (LS). Sea-ice transport, and localized ice formation and melt are the primary influences of boundary current  $S$  variability. Winter sea-ice typically forms along the Labrador Coast and at the mouths of the Hudson and Davis Straits. Annual break-up and melt of sea-ice, if any, is transported through the Labrador Current. The interannual to decadal variability in the progression of winter sea-ice concentration anomalies (formed and transported sea-ice) in the eastern LS, from the northern Labrador Sea to the southern tip of Newfoundland, has been studied by Deser *et al.* [26]. Their study provides evidence of a correlation between the spring-summer surface  $S$  anomalies and sea-ice concentration anomalies off Fylla Bank (64°N, 54°W) and correlation,

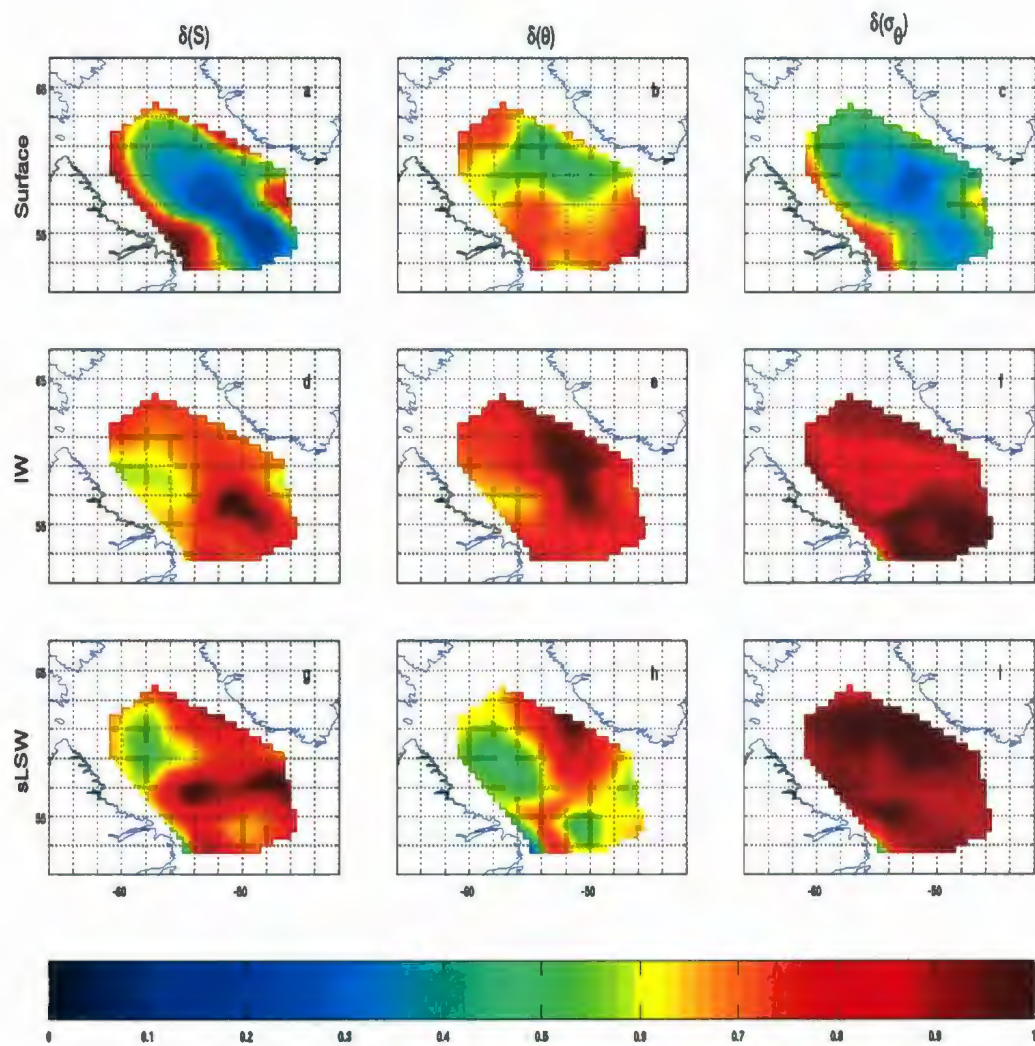


Figure 3.1. Standard deviation ( $\delta$ ) of the anomalies: surface layer (a) salinity, (b) potential temperature and (c) potential density; Irminger water (d) salinity, (e) potential temperature and (f) potential density; shallow Labrador Sea water (g) salinity, (h) potential temperature and (i) potential density. Each  $\delta$  map has been normalized by its maximum value.

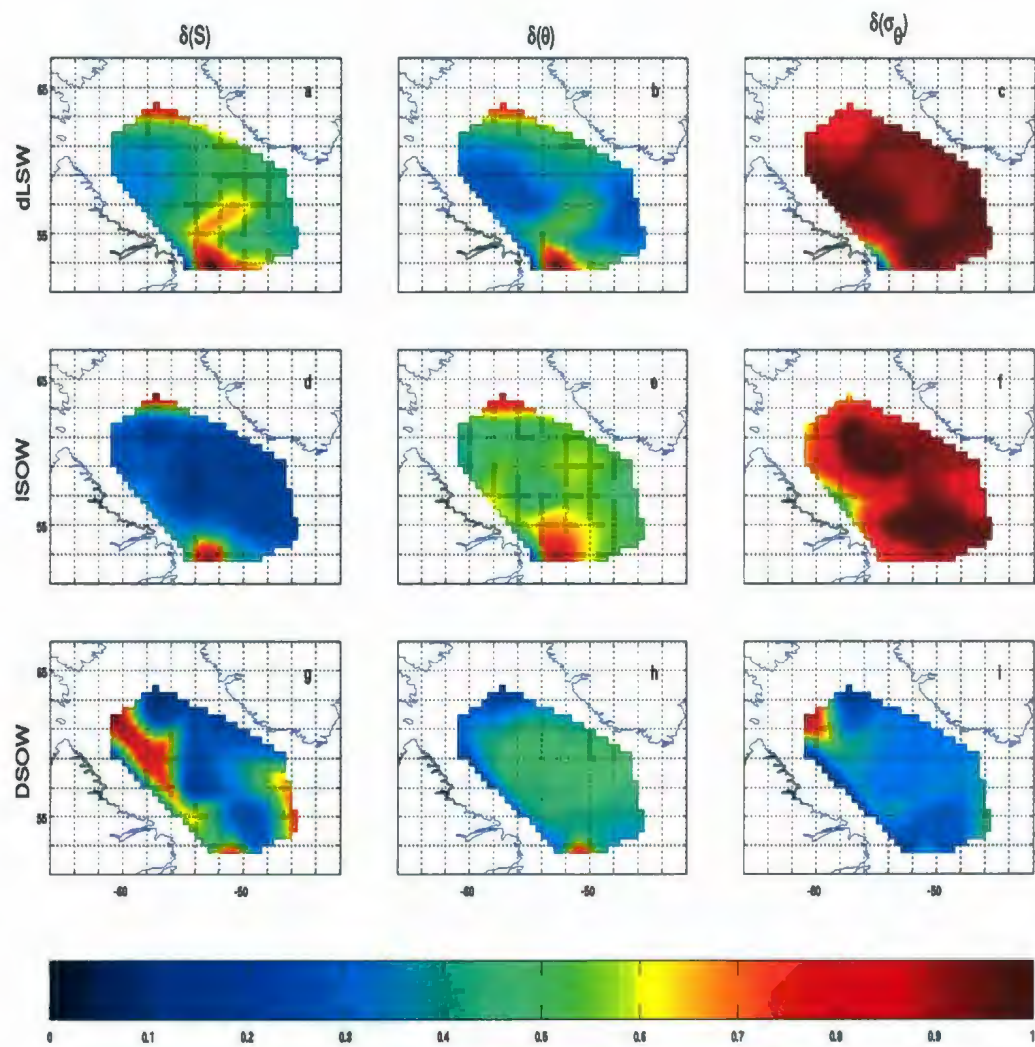


Figure 3.2. Standard deviation ( $\delta$ ) of the anomalies: deep Labrador Sea water (a) salinity, (b) potential temperature and (c) potential density; Iceland-Scotland Overflow water (d) salinity, (e) potential temperature and (f) potential density; Denmark Strait Overflow water (g) salinity, (h) potential temperature and (i) potential density. Each  $\delta$  map has been normalized by its maximum value.

with a 2 year lag, between sea-ice concentration in the LS and winter sea surface temperature anomalies in the subpolar North Atlantic gyre ( $50^{\circ} - 62^{\circ}\text{N}, 46^{\circ} - 12^{\circ}\text{W}$ ). In the  $\delta(\theta)$  map, 3.1(b), inflow from the southeast Labrador Sea and Hudson and Davis Straits clearly impacts the  $\theta$  variability more than the southward transport of ice along the Labrador coast.

### 3.1.2 IW layer

The variability of  $S$  and  $\theta$  in the IW layer depends upon the processes related to the major currents and water mass transport. Regions with enhanced eddy activity are often associated with baroclinically unstable regions, such as the West Greenland Current. Confinement of these instabilities by topographic variations results in some of the most interesting oceanographic features. Strongly localized eddy variability has been observed in the West Greenland Current near  $61.5^{\circ}\text{N}, 53^{\circ}\text{W}$  where the 3000 m isobath diverges from the West Greenland coast [3, 16, 13, 17]. The 3000 m isobath is observed by Lavender *et al.* [3] as a transition region between strong cyclonic flow along the 1000-3000 m continental slope and weaker anticyclonic flow in the basin interior. Strong eddy variability is apparent in the  $\delta(\theta)$  map, Figure 3.1(e), and is also somewhat seen in the  $\delta(S)$  map, Figure 3.1(d). This is expected in the IW layer since the water properties between the West Greenland Current and central LS differ mainly in  $\theta$ . The maximum  $\delta(\theta)$  occurs at the southward turn of the 3000 m isobath with near maximum  $\delta(\theta)$  extending southward to the central LS. Eddies shed near  $61.5^{\circ}\text{N}, 53^{\circ}\text{W}$  propagate not only westward with the cyclonic boundary flow, but also southward to the central LS with the mean background anticyclonic flow in the central basin. The eddies carry heat from the West Greenland Current into

the central LS<sup>1</sup>, typically during restratification, to balance surface heat loss at the ocean-atmosphere interface during convection.

Strong  $S$  variability in the IW layer coincides with the strong  $\theta$  variability in the northern LS and along the West Greenland Current, which is associated with eddy fluxes of saline (and warm) West Greenland Current water into the central LS. The maximum  $\delta(S)$  is also a result of processes involved in deep convection, although the feature is eastward of the location convection is typically observed. Deep convection can occur throughout the central LS, but the most intense convection typically occurs adjacent to the Labrador Shelf [5, 13], where the coldest and driest continental winds result in the greatest heat and moisture flux. The convective depth reaches the IW layer nearly annually and so smaller  $\delta(S)$  is expected if the variability were due solely to the deepening of the mixed layer. A mean anticyclonic circulation at 700 m depth is observed by Lavender *et al.* [3]. The maximum variation in  $S$  distinguishes variability of entrainment of shallow, convected water into the observed eastward mid-depth circulation along with the variability in the convective region and eddy variability from the West Greenland Current. While a combination of variability from both eddy activity and deep convection is observed in the  $\delta$  maps, variability from eddy activity is more prominent in  $\delta(\theta)$  and from deep convection in  $\delta(S)$ .

### 3.1.3 sLSW Layer

Similar  $\delta(S)$  and  $\delta(\theta)$  distributions, Figures 3.1(g, h), are observed in the sLSW layer. The eddy shedding from the West Greenland Current has strong impacts on both  $\delta(S)$  and  $\delta(\theta)$ . As in IW, eddy variability south of where the 3000 m isobath diverges from the West Greenland coast is still stronger than eddy variability in the

---

<sup>1</sup>This is further discussed in Sections 1.2.2 and 3.2.2

westward flow along the continental shelf. Deep convection is a remarkable feature in  $\delta(S)$  but is not well represented in  $\delta(\theta)$ . Deep convection down to the sLSW layer (and less frequently down to the dLSW layer) is interannual in period and typically seen slightly seaward of the 3000 m isobath (sometimes called the 'gyre product') but convection has also been observed shoreward of the 3000 m isobath directly in the Deep Western Boundary Current (DWBC) [13]. Convected water formed in the rim current, sometimes referred to as the "boundary product", is more readily injected into the DWBC. Both the sLSW gyre and boundary products, not entrained into the DWBC, will be entrained into the anticyclonic mid-depth circulation and exported out of the LS. The two pathways of sLSW export are clearly seen in  $\delta(S)$  and  $\delta(\theta)$ .

#### 3.1.4 dLSW Layer

In the dLSW layer,  $S$  and  $\theta$  variability is greatest from inflow through the Davis Strait and processes involved in deep convection, while some variability from eddy activity along the West Greenland Current is still distinguished (Figures 3.2(a, b)). Inflow from Davis Strait crosses the cyclonic flow around the LS basin. Variability in this influx of cold, fresh water mixing with the warmer, saltier deep West Greenland Current water is represented by the high  $S$  and  $\theta$  variability near  $64^\circ\text{N}$ ,  $57^\circ\text{W}$ . The most prominent  $\delta$  feature, however, is the single pathway of dLSW export. Deep Labrador Sea water is the product of deepest reaching convective events, to a maximum observed depth greater than 2200 m in 1992. Interannual events in which convection reaches this layer are even fewer than those reaching the sLSW layer and thus a lower frequency of export from the dLSW 'reservoir'. Also, the depth of this water mass prevents entrainment in the upper anticyclonic circulation observed in the IW and sLSW layers. Both the dLSW boundary and gyre products, that is, dLSW formed

both shoreward and seaward of the 3000 m isobath, are exported from the LS via the DWBC. This export through the DWBC is seen by the  $\delta(S)$  and  $\delta(\theta)$  maximum east of the Hamilton Bank along the continental slope near  $53^\circ\text{N}$ ,  $53^\circ\text{W}$  in Figures 3.2(a, b).

### 3.1.5 Bottom Water Masses

Salinity and potential temperature variability apparent in the ISOW and DSOW layers *appear* to be related to convective processes. The convective depth does not reach the ISOW layer but the increase in  $\delta(S)$  and  $\delta(\theta)$  near  $53^\circ\text{N}$ ,  $51.5^\circ\text{W}$  is mixing between the upper transport of dLSW through the DWBC along the 2000-3000 m continental slope. Vertical sections taken in 1996 and 2001 at  $53^\circ\text{N}$ , studied by Stramma *et al.* [14] show ISOW (Charlie Gibbs Fracture Zone Water, or GFZW, in their study) along the 2000-3000 m slope extending no further than  $51.5^\circ\text{W}$  at  $53^\circ\text{N}$ . The maximum  $\delta(S)$  and  $\delta(\theta)$  at  $53^\circ\text{N}$ ,  $53^\circ\text{W}$  is centered at region 19<sup>2</sup>. The northeast corner of region 19, defined in Figure 2.1, lies over a fraction of the continental slope. For region 19, since  $\sim 14\%$  of the measurements are at depths greater than 1000 m and only  $\sim 0.6\%$  are deeper than 1500 m, the majority of observations in region 19 must be of water properties of dense shelf and sea ice and not of the ISOW water mass (recall that the water masses are defined by  $\sigma_\theta$ ). Thus, the variability calculated in region 19 will be large from the differing  $S$  and  $\theta$  of shelf ice and ISOW. Despite the erroneous maximum variability at  $53^\circ\text{N}$ ,  $53^\circ\text{W}$ , there is still larger  $\delta(S)$  and  $\delta(\theta)$  in the DWBC along the continental slope. This larger variability represents the small amount of vertical mixing between ISOW and upper dLSW export. The same situation is seen in DSOW near  $52^\circ\text{N}$ ,  $51^\circ\text{W}$  centered at region 20, however, the larger variability is

---

<sup>2</sup>Regions are defined in Figure 2.1

not attributed to deep convection. The northeast corner of region 20 lies over an even smaller fraction of water deeper than 3000 m, the approximate minimum depth at which DSOW is observed. All DSOW measurements in region 19 are at depths 130.2 – 187.4 m and in region 20, there are only 11 measurements at depths greater than 2300 m. Therefore, the maximum at 52°N, 51°W should be discarded. In region 18 (located strictly over the Labrador Shelf), there are 18 observations of ISOW in the depth range 131.275 – 139.297 m. These measurements are assumed to be measurements of dense shelf ice. In fact, a closer look at the number of observations in each defined region, the variability maxima and the bounding depths of ISOW and DSOW show that the observed maxima are likely the result of insufficient data and poorly chosen regions of analysis for ISOW and DSOW. As ISOW and DSOW circulate the North Atlantic Current System, both water masses enter the Labrador basin in the deep WGC and exit through the DWBC. Initially, cold and dense ISOW enters the basin and transforms into a warmer, saltier product through vertical mixing with dLSW as it circulates the basin [23]. While DSOW is subject to even less vertical mixing than ISOW, both water masses have seen significant changes since the 1960s; respectively, ISOW and DSOW densities have decreased with estimated freshening equivalent to mixing a ~0.6 m and ~0.3 m freshwater layer into the ISOW and DSOW layers of 1964-1972 [23].

## 3.2 Water Mass Skewness

The geographical distribution of skewness ( $\gamma_3$ ) of hydrographic measurements provide insight into the location of thermohaline gradients. Skewness maps of  $S$ ,  $\theta$  and  $\sigma_\theta$  anomalies are given in Figure 3.3 for surface water, IW and sLSW and in Figure 3.4 for dLSW, ISOW and DSOW. The statistical significance of the skewness in each region

	Normalized $\sigma$	$\delta(S)$ (psu)	$\delta(\theta)$ ( $^{\circ}\text{C}$ )	$\delta(\sigma_{\theta})$ ( $\text{kg}/\text{m}^3$ )
Surface	0	0.1101	1.1252	0.2025
	1	0.8680	2.3909	0.8051
IW	0	0.0393	0.2743	0.0140
	1	0.0689	0.4402	0.0295
sLSW	0	0.0122	0.0566	0.0081
	1	0.0327	0.3539	0.0198
dLSW	0	0.0000	0.0000	0.0000
	1	0.0379	0.3482	0.0091
ISOW	0	0.0058	0.0297	0.0107
	1	0.0578	0.4529	0.0241
DSOW	0	0.0018	0.0261	0.0021
	1	0.0507	0.6864	0.0534

Table 3.1. Maximum and minimum standard deviations of  $S$ ,  $\theta$  and  $\sigma_{\theta}$  corresponding to the normalized standard deviation extrema.

was tested using (2.7). Regions in which the skew is statistically not significantly different from zero at the 95% confidence level are outlined in black. In each figure, skewness has been normalized by the maximum absolute value, preserving skewness polarity. The actual  $\gamma_3$  maxima and minima corresponding to the normalized extrema of -1 and 1 are given in Table 3.2. Here we speculate on distinguishing the classical Labrador Sea ocean processes in the skewness maps.

### 3.2.1 Surface Layer

Variability of surface heat fluxes and inflow are the primary sources of skewness in the surface  $\theta$  distribution. Straneo [10] and Lilly *et al.* [15] find good agreement between observed and estimated surface heat fluxes and conclude that surface layer heat content is strongly controlled by the surface heat flux. The majority of the  $\sim 1$

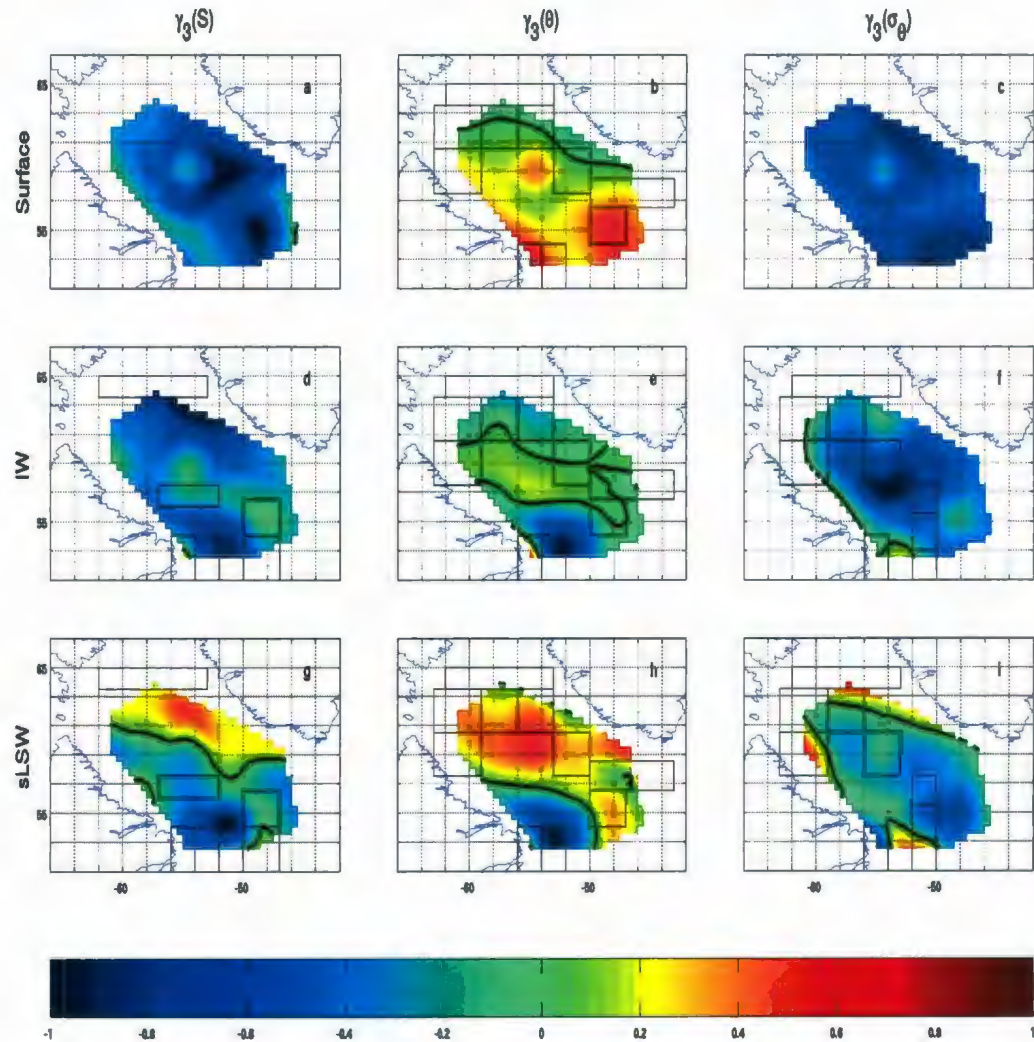


Figure 3.3. Skewness ( $\gamma_3$ ) of the anomalies: surface layer (a) salinity, (b) potential temperature and (c) potential density; Irminger water (d) salinity, (e) potential temperature and (f) potential density; shallow Labrador Sea water (g) salinity, (h) potential temperature and (i) potential density. Each  $\gamma_3$  map has been normalized by its maximum value. Zero contours are thickened black lines. Regions in which the skew is statistically not significantly different from zero are outlined.

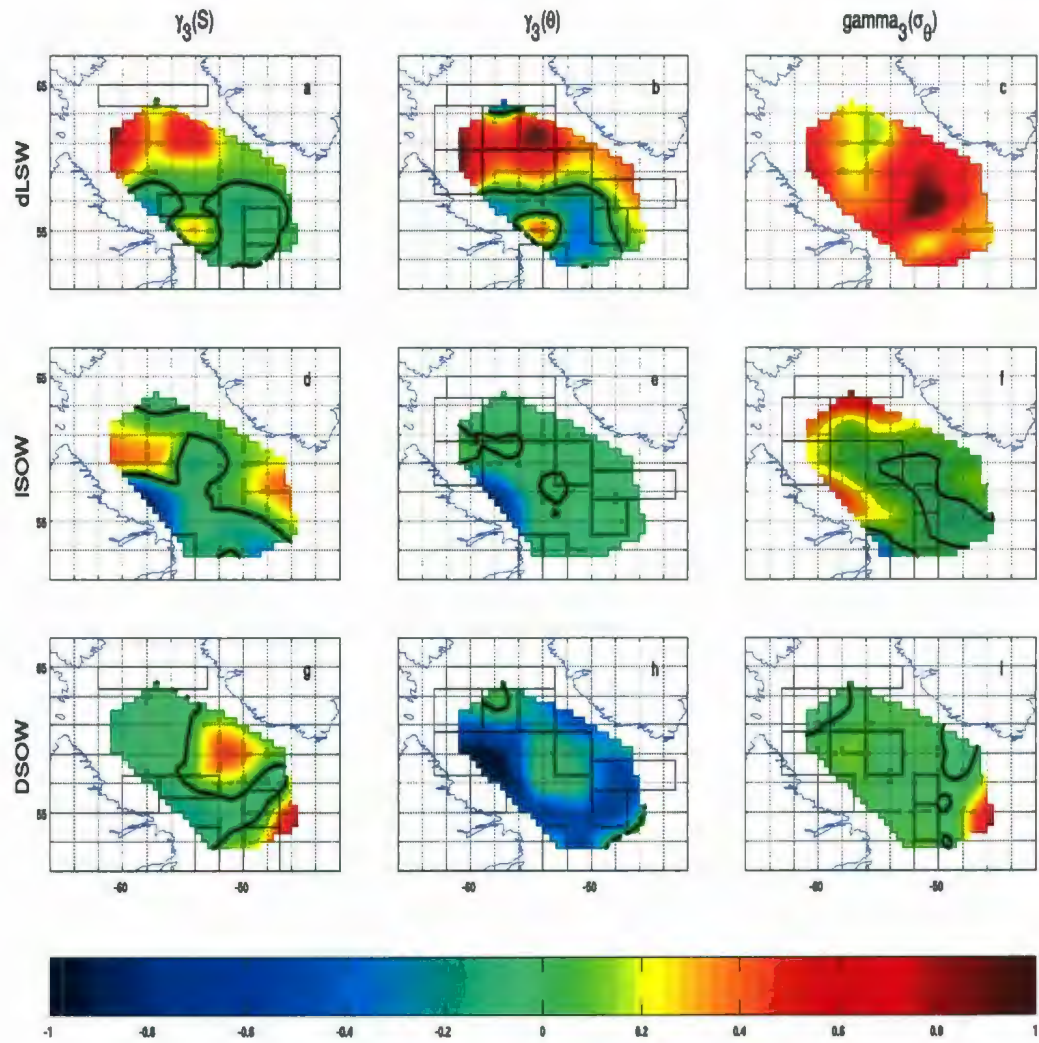


Figure 3.4. Skewness ( $\gamma_3$ ) of the anomalies: deep Labrador Sea water (a) salinity, (b) potential temperature and (c) potential density; Iceland-Scotland Overflow water (d) salinity, (e) potential temperature and (f) potential density; Denmark Strait Overflow water (g) salinity, (h) potential temperature and (i) potential density. Each  $\gamma_3$  map has been normalized by its maximum value. Zero contours are thickened black lines. Regions in which the skew is statistically not significantly different from zero are outlined.

GJ m<sup>2</sup> of heat annually lost to the atmosphere, occurs at the onset of, and during, active oceanic convection in the central LS. Mainly during restratification, the surface layer heat content is replenished by a subsurface convergence of heat in the IW, sLSW and dLSW layers from the West Greenland Current import of Irminger Water, which balances and often exceeds the surface layer heat loss. Interannual events in which the acquired heat is in excess of that lost to the atmosphere are balanced by a surface divergence of heat to the cold surface boundary currents. This interannual variability of excess heat exchange in the surface layer is distinguished by the dominant positive  $\gamma_3(\theta)$  in Figure 3.3(b). But what explains the tendency toward negative to small positive values in the northern LS and large positive values in the southern LS? As discussed in the previous section, the observed variability in the northern and southern LS is from colder Hudson and Davis Strait inflow and warmer southeastern inflow to the LS. Taking into account the relative temperature contrasts between these surface waters upon mixing, surface  $\gamma_3(\theta)$  can be explained. Interannual events of colder inflow mixing with the LS water give negative to small positive  $\gamma_3(\theta)$  in the northern LS and events of warmer inflow mixing with the LS water give positive  $\gamma_3(\theta)$  in the southern LS.

Explanation of the surface  $\gamma_3(S)$  is more complicated but can most likely be attributed to the interannual and decadal variability in the mesoscale variability of sea-ice formation, sea-ice melt, freshwater and sea-ice transport processes. During late spring and summer, over 0.5 m of freshwater accumulates in the surface central LS. A fraction of the accumulated freshwater is mixed downward during convection, while the remaining freshwater is both evaporated during convection by the cold, dry atmospheric forcing and laterally exchanged with the surface boundary current water. Roughly comparing the surface  $S$  variability and skewness in Figures 3.1(a) and 3.3(a), strong  $S$  variability has small skew and weak  $S$  variability has large

skew, except for the prominent pocket of larger  $\gamma_3(S)$  centered in Region 8 which will be discussed in the subsequent paragraph. The correlation coefficient ( $R$ ) of  $\delta(S)$  and  $\gamma_3(S)$  is 0.57 and excluding region 8, the correlation coefficient is 0.62. If the number of years having high sea-ice concentration anomalies balances the number of years having low anomalies then high  $\delta(S)$  and small  $\gamma_3(S)$  should be observed. High  $S$  variability and small skewness is expected and observed along the Labrador Current, since it is a major pathway for the transport of sea-ice and freshwater, and is subject to large variations in sea-ice formation and melt. There is also high  $\delta(S)$  and small negative  $\gamma_3(S)$  in the surface West Greenland Current near the southern tip of Greenland although the origin of this variability is unclear. In the central LS, neglecting region 8, several anomalous freshwater events would explain the strongly skewed  $S$  distribution and weak variability. Decadal pulses of freshwater in the surface layer, typically called Great Salinity Anomalies (GSAs), have been observed in the early 1970s, mid 1980s and mid 1990s [27]. The source of central LS freshwater are the LS boundaries. According to Houghton and Visbeck [27], a 20% increase of inflow from the boundaries or less convective mixing to depth could explain the quasi-decadal variation in the central LS surface  $S$  from GSAs.

### 3.2.2 Intermediate Water Masses

The subsurface convergence of heat responsible for the positive  $\gamma_3(\theta)$  tendency in the surface layer is distinguished in the IW, sLSW and dLSW  $\theta$  skewness maps, Figures 3.3(e,h) and 3.4(b). The intensity of convection mainly depends upon the intensity of atmospheric forcing and the depths convection reached in the prior years. Overturning in the surface layer will occur annually, reach the IW layer nearly annually, and the sLSW layer roughly interannually. Deep convection down to the dLSW

layer is least frequent. During restratification of the subsurface layers in the central LS, warm Irminger Sea Water is imported by eddies shed from the West Greenland Current. The increase in heat content of the CLS water column balances the heat loss to the atmosphere during the convection periods but often can exceed the loss [10]. Corresponding to the frequency convection reaches each subsurface layer, heat import and excess is expected to occur most frequently in the IW layer and least frequently in the dLSW. Indeed, in the central LS, the  $\theta$  skewness maps show a tendency toward increasing positive skew from IW to dLSW, distinguishing the frequency of heat import events in each layer. For example, near the center of region 8, the  $\gamma_3(\theta)$  values are  $\sim 0.1513$ ,  $\sim 0.5807$  and  $\sim 0.8452$  for IW, sLSW and dLSW respectively. The pocket of positive  $\gamma_3(\theta)$  in region 8 in the surface layer coincides with the large  $\gamma_3(\theta)$  in the LSW layers and could be the result of the interannual heat excess when the sLSW and dLSW layers are restratified.

The  $\gamma_3(S)$  maps, 3.3(d,g) and 3.4(a), are quite similar to the  $\gamma_3(\theta)$  maps, except in the sLSW layer where negative  $S$  skewness extends both further North and East than expected. The accumulated surface freshwater in the central LS that mixes downward during convection freshens the IW, sLSW and dLSW layers. During restratification, salt is imported with the heat import by eddies shed from the West Greenland Current, but in contrast to the  $\theta$  skewness, the reason for the observed  $S$  skewness in the central Labrador Sea IW, sLSW and dLSW is unclear. Interannual salt excess is expected to coincide with the interannual heat excess from the eddy imports, however,  $\gamma_3(S)$  in region 8 in the sLSW layer is mostly negatively skewed, which is representative of interannual freshening instead. Other studies [10] still cannot explain the lateral exchange of fresh and salty water during convection and restratification. Before attempting to explain  $S$  skewness in the central LS, the processes responsible for the salt budget need to be better understood.

A second striking coherent feature in  $\gamma_3(\theta)$  and  $\gamma_3(S)$  appears at the location of removal of the convectively formed LSW water into the North Atlantic current system. If convection reaches the IW layer, the newly ventilated water is flushed out of the central LS, near  $54^\circ\text{N}$   $52^\circ\text{W}$ , through entrainment with the southern Labrador Current. Variability of the cooler, fresher, convected water mixing with Labrador Current in the IW layer is apparent at the skewness minima in Figures 3.3(d,e). Similarly, upon interannual renewal of sLSW, typically near the 3000 km isobath off the Labrador Shelf [5, 13], export of the sLSW (near  $54^\circ\text{N}$ ,  $52^\circ\text{W}$  mixes with the LC (Figures 3.3(g,h)). Renewal and removal of dLSW occurs even less frequently and typically seaward of the 3000 km isobath [13], but with an additional pocket of positive skewness at  $55^\circ\text{N}$ ,  $54^\circ\text{W}$ . This prominent, positive  $\gamma_3(S)$  and  $\gamma_3(\theta)$  is thought to be upwelling of warmer, saltier ISOW into the dLSW layer over the deep 2000-3000 m continental slope in the LC, caused by the (interannual) horizontal divergence of dLSW<sup>3</sup>. As expected, upwelling of dLSW into the sLSW layer is not observed since  $S$  and  $\theta$  do not differ significantly between the two LSW layers.

### 3.2.3 Bottom Water Masses

Features in the ISOW and DSOW skewness maps are more difficult to interpret but likely result from long-term changes in the water masses [23] and variability in vertical mixing. Cold, fresh and dense ISOW initially enters the LS in the deep West Greenland Current, progressively warming and salinizing through small vertical mixing with dLSW as it circulates around the basin [23]. The transformation of ISOW is primarily seen in the  $\gamma_3(S)$  and  $\gamma_3(\theta)$  maps, (Figures 3.4(d, f)), however, its warming

---

<sup>3</sup>This is further discussed in Section 4.4.4

	Normalized $\gamma_3$	$\gamma_3(S)$	$\gamma_3(\theta)$	$\gamma_3(\sigma_\theta)$
Surface	-1	-2.7463	-0.3936	-1.9174
	1	0.2113	1.9966	-0.5173
IW	-1	-1.6534	-2.4679	-0.7681
	1	0.4255	1.5129	0.1625
sLSW	-1	-1.5294	-1.7306	-0.7216
	1	0.8311	1.1615	0.5091
dLSW	-1	-1.2582	-1.1614	0.0918
	1	3.4731	1.6904	0.6312
ISOW	-1	-8.4070	-11.1088	-1.1308
	1	3.6598	0.8329	1.7027
DSOW	-1	-2.3893	-0.7530	-1.2454
	1	11.9790	0.1614	14.0779

Table 3.2. Maximum and minimum skewness of  $S$ ,  $\theta$  and  $\sigma_\theta$  corresponding to the normalized coefficient of skewness extrema.

is not well represented in Figure 3.4(e). As ISOW circulates around the basin, initial mixing with saltier upper water in the West Greenland Current results in positive  $\gamma_3(S)$ . Mixing with cooler, fresher upper water in the Labrador Current follows, producing negative  $\gamma_3(S)$  and stronger negative  $\gamma_3(\theta)$ . A lack of data is attributed to the statistically insignificant, negative  $\gamma_3(\theta)$  in the West Greenland Current and northern LS where positive skewness was expected. Statistical insignificance is also prominent in the DSOW skewness maps (Figures 3.4(g-i)), but  $\gamma_3(S)$  shows the same general feature of mixing with the saltier ISOW in the West Greenland Current followed by mixing with the fresher ISOW in the northern LS and Labrador Current. Few observations in the most southeastern LS likely lead to  $S$  and  $\sigma_\theta$  skewness values greater than 10.

### 3.3 Anomaly Probability Density Distributions

Oceanographic data are typically approximated as having a normal distribution, but this is not always a valid assumption. As discussed in Chapter 2, a normal approximation of a distribution is appropriate in theory, assuming a sufficiently large sample size in which each observation has a small, additive, stochastic component. Every measurement of salinity, temperature and pressure has an associated random error, and so being expected, normality in oceanographic data is the only characteristic that need not be explained. The hydrographic properties,  $\theta = \theta(S, T, P)$  and  $\sigma_\theta = \sigma_\theta(S, T, P)$ , are non-linearly calculated from the data, implying non-Gaussian distributions. These properties are, however, intrinsic to sea water with only depth dependence removed, so indifferent to calculations used, normal distributions are expected. Results of the previous section show significantly skewed  $S$ ,  $\theta$  and  $\sigma_\theta$  distributions in many regions of the LS, and therefore regions in which the distributions significantly differ from normality. Maxima, minima and polarity changes in skewness coincide with known thermohaline gradients of Labrador Sea processes. Skewness is clearly representative of mesoscale variability but mesoscale variability is not independent of the interannual and decadal variability in the hydrographic properties. In this section, we look specifically at the distributions to clarify the variability.

#### 3.3.1 $\chi^2$ test

The  $\chi^2$ -test was used to test the null hypothesis of normal  $S$ ,  $\theta$  and  $\sigma_\theta$  distributions having estimated means and variances of the respective *non-normalized* anomalies. The test statistic ( $\chi^2$ ) and p-value for each region and water mass are given in the respective histograms. The null hypothesis is rejected at the 5% significance level with zero probability of observing the given statistic for all  $S$ ,  $\theta$  and  $\sigma_\theta$  distributions.

### 3.3.2 The Distributions

Histograms of salinity, potential temperature and potential density for each water mass in the NLS, WGC, CLS, LC and SELS are shown in Figures A.1-A.6. The histograms bin the normalized anomalies into 40 bins and are overlaid with normal probability distributions having the same means and standard deviations as the histograms. The appearance of bimodality in the histograms suggest possible superposition of normally distributed data with shifted mean states taken over shorter time periods.

Gaussian kernel density estimates of the probability density distributions were computed for each of the time periods 1938-06, 1963-73, 1989-99, 1938-84 and 1985-06<sup>4</sup>. The kernel density estimates for the shorter time periods do characterize the 1938-2006 bimodal behaviour but are also non-Gaussian. A clear example of this is seen in surface layer salinity in the northern LS; Figure 3.5(a) shows the histogram overlaid with a normal distribution having the same mean and variance as the histogram, and Figure 3.5(b) shows the kernel density estimates for the five time periods.

The bimodality of the northern LS  $S$  density estimates of 1938-84, 1985-06, 1963-73 and 1989-99 all match well with the bimodality of the 1938-06 density estimate. During each of the five time periods, there appear to be two regimes, a positive  $S$  anomaly regime and a negative, distinctly split by zero mean. In addition, two separate positive  $S$  modes are only observed in 1985-06 and 1989-99 which impact the 1938-06 distribution. Most interestingly, similar skewness is inherent in all five distributions despite changing the time span of the data, which also changes the northern LS  $S$  regimes. Moreover, no decadal variability and little interannual variability is

---

<sup>4</sup>Section 4.1 discusses 1938-1984 and 1985-2006, and Section 4.2 discusses 1963-1973 and 1989-1999

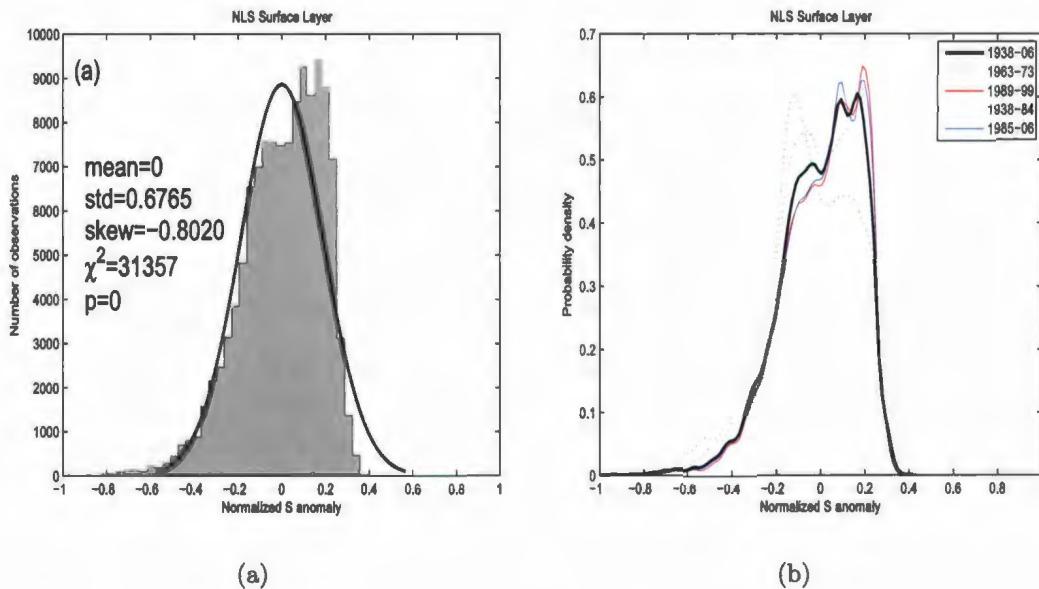


Figure 3.5. Surface layer salinity data during 1938-2006 in the northern Labrador Sea; (a) Histogram overlaid with normal probability distribution having the same mean and standard deviation as the histogram. Shown is the mean, standard deviation, skewness and  $\chi^2$ -test statistic with associated p-value for the *non-normalized* anomalies. (b) Probability density distribution estimated using a Gaussian kernel with a bandwidth (bw) of  $0.9An^{-1/5}$  where  $A$  is an adaptive estimate of spread and  $n$  is the number of observations (here,  $bw=0.0163$ ). The anomalies have been normalized by their maximum value in both the histogram and density distribution.

present during 1963-73 and 1989-99 [21] but the skewness, and main positive and negative mode remain. These same general characteristics are similarly seen in other distributions. Figure 3.6(a) is the kernel density estimate of the Labrador Current  $\theta$  distribution in the surface layer. All five time periods appear to have the same bimodal structure and skewness. Distributions in which the modal structure changes with a change in time span also tend to differ in skewness. This is seen in the kernel density estimates of the southeast LS  $\theta$  distributions in the IW layer (Figure 3.6(b)). It should be stated that skewness does differ between the 'time-period' distributions regardless of whether they have similar modes or not, but the polarity of skew remains the same. Modes in the 1963-73 and 1989-99 distributions represent variability less frequent than annual but more frequent than interannual. Provided the time periods all contain roughly similar variability, similar skewness is observed.

### 3.4 Summary

The  $\delta(S)$  and  $\delta(\theta)$  of the LS water masses depend on the interannual, decadal and mesoscale variability of  $S$  and  $\theta$ . It is a useful dimension which allows identification of the major processes responsible for the changes in the LS. Surface  $S$  is strongly influenced by the variability of sea-ice and transport in the Labrador Current. Variability of surface  $\theta$  mostly depends upon the water exchange through the northern and southeastern borders of the LS and less on the Labrador Current variability and surface fluxes. Compared to the surface layer, subsurface water masses are not directly influenced by sea-ice processes or atmosphere-ocean heat, evaporation and precipitation fluxes, but by exchanges between water masses, transport and major currents. In the IW layer, variability is strongly influenced by eddy shedding in the West Greenland Current and the export of shallow, convectively formed water in the

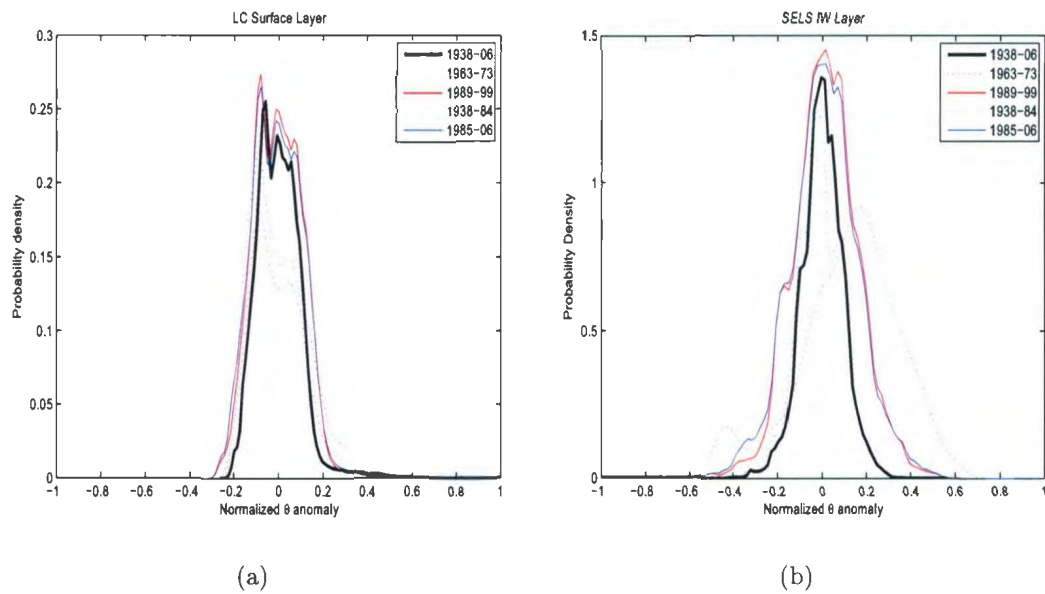


Figure 3.6. Probability density distribution estimated using a Gaussian kernel with a bandwidth (bw) of  $0.9An^{-1/5}$  where  $A$  is an adaptive estimate of spread and  $n$  is the number of observations. (a) Labrador Current  $\theta$  distributions in the surface layer with  $bw=0.09$  and (b) southeast LS  $\theta$  distributions in the IW layer with  $bw=0.0267$ . The anomalies have been normalized by their maximum value in both the histogram and density distribution.

subsurface anticyclonic circulation. Variability in the Labrador Sea water masses, sLSW and dLSW, is mainly related to deep convection and export of the convectively formed water. Primary influences of the variability in the two bottom water masses are difficult to distinguish due to the data and method used, but variability is the result of small vertical mixing as ISOW and DSOW enter, circulate, and exit the Labrador basin, and in particular, the decadal variability in the ISOW and DSOW properties.

Skewness of  $S$  and  $\theta$  of the LS water masses is another statistic that depends upon mesoscale variability and since the dataset spans 1938-2006, it also depends upon interannual and decadal variability. While interannual and decadal variability are ingrained in mesoscale variability, the skewness maps distinguish mixing between thermohaline gradients. Skewness in the surface layer  $\theta$  is mostly dependent upon interannual variability of vertical heat fluxes at the atmosphere-ocean interface and lateral heat fluxes in the subsurface layers. Interannual and decadal variability in ice and freshwater transport mainly influences surface  $\gamma_3(S)$ , and in particular, the main impact on the central LS surface  $\gamma_3(S)$  seems to be the GSAs. The primary influence of skewness in the intermediate layers is variability of lateral heat and salt exchange in processes associated with deep convection. In the bottom water masses, the main contribution to skewness is likely small vertical mixing and decadal variability.

Probability distributions aid in understanding the effects variability can have on skewness. Distributions of anomalies during different time spans can be compared to distinguish whether skewness is a function of long-term variability. The non-Gaussian  $S$ ,  $\theta$  and  $\sigma_\theta$  probability distributions are statistically significant, bimodal and skewed. The variability of a distribution is a superposition of temporal and spatial variability. Skewness is thought to signify spatial variability. In this study, skewness should distinguish mesoscale variability, however, the mesoscale variability also has intrinsic

temporal variability due to the interannual and decadal variations of  $S$  and  $\theta$  during 1938-2006. Separating the data into shorter time periods should therefore not change the general skewness polarity if the time periods have similar variability.

## Chapter 4

### Sensitivity of Skewness

If skewness in hydrographic data indicates regions of mixing between water masses, the general features of thermohaline gradients in the skewness maps of the 1938-2006 hydrographic data will remain if the span of the time period is changed. A change in the hydrographic mean state should not affect skewness. In Section 4.1, we choose two time periods with significantly different mean states. A shift from the 1938-1984 mean state to a significantly different mean state during 1985-2006 is first hypothesized and confirmed. To remove long-term variability, two one-decade periods with roughly homogeneous properties and different mean states are considered in Section 4.2. In Section 4.3 maps of  $S$ ,  $\theta$  and  $\sigma_\theta$  variability for the four time periods are presented and compared to the variability maps of the entire record. Similarly, Section 4.4 discusses the skewness maps of all five time periods and the sensitivity of skewness to interannual and decadal variability. The results are summarized in Section 4.5.

## 4.1 Regime Shift: 1938-1984 and 1985-2006

The Labrador Sea water (LSW) properties have changed remarkably during the record of deep measurements [28, 29, 11]. During the 1990s the LSW was the freshest and coldest, and during the 1960s, the warmest and saltiest than at any other time since 1938 (see Plate 7.3.6 in [30]). Two separate regimes of the CLS water column can be hypothesized based on Plate 7.3.6 in [30]: the water masses during 1938-84 appear to be warmer and saltier on average than those over the 1985-06 period.

A change in the mass transport of the North Atlantic gyre nearly coincides with the change in sea-water properties in the central Labrador Sea. Depending upon the intensity of atmospheric forcing [12] deep convection ventilates the subsurface layers down to the dLSW, changing the vertical density structure and heat content of the central Labrador Sea water column. These changes are manifested in the distribution of the potential energy anomalies (PEAs). Curry and McCartney [21] construct a PEA based mass transport index between the North Atlantic subpolar and subtropical gyres, an oceanic analogue to the SLP based NAO index, and find indication of the ocean transport signal reflecting the NAO. They show an increase in mass transport in the North Atlantic gyre beginning in the early 1980s coinciding with the persistent positive NAO index through to 1995 however lacking direct covariance.

In this sensitivity study, the periods 1938-1984 and 1985-2006 were chosen since (1) very roughly, 1938-1984 and 1985-2006 contain a similar number of observations for each water mass, (2) changes in the production and characteristics of the sLSW and dLSW in the central Labrador Sea appear to split near 1985 [30], (3) changes in the PEA transport index [21] are driven by changes in vertical density structure and heat content, (4) there is an increase in mass transport in the North Atlantic gyre [21] and (5) the mass transport increase and transition to NAO<sup>+</sup> roughly coincide around

the early 1980s (although there is no direct covariance between the increase and NAO transition) [21]. The hypothesis of the 1938-1984 mean state being significantly different than the 1985-2006 mean state is tested in Section 4.1.2.

### 4.1.1 TS Diagrams

The annual mean  $\theta$ - $S$  distributions exhibit a mean shift from warm, salty water during the 1938-1984 period to cooler, fresher water during 1985-2006 in the subsurface layers. In each region except the central Labrador Sea this mean shift is seen in the sub-Irminger water layers (Figures B.3, B.5, B.7 and B.9) while in the central Labrador Sea this mean shift is observed in the water masses below sLSW (Figure 4.1). If the density profiles do not change annually, the mean layer depths do not change, independent of any fluctuations in temperature and salinity profiles. Consecutive annual variations in temperature compensated by an opposite effect in salinity variation result in consecutive years of nearly constant core density of a given water mass. Years in which the density deviates from the core density indicate periods in which salinity and potential temperature are non-compensating.

In the central Labrador Sea during 1992 and 1995, non-compensating temperature and salinity effects decreased the ISOW density resulting in mixing with the dLSW. Figure 4.1 shows the average  $\theta - S$  of ISOW in 1992 and 1995 near the lower bounding isopycnal of dLSW,  $\sigma_\theta = 27.77 \text{ kg m}^{-3}$ . These years correspond with the 4-year period, 1990-1993, of deepest convection observed on record [6] with convection penetrating deeper than 2200 m in 1993 [5]. The volume of LSW reached a maximum thickness of 1700 m in 1992-1994, reducing thickness to only 200 m by 1999 [6]. The depth range of LSW calculated by Yashayaev [11] in 1994 is 500-2400 m, with LSW defined slightly differently by  $36.86 < \sigma_2 < 36.88$  ( $\sigma_2$  is the potential density

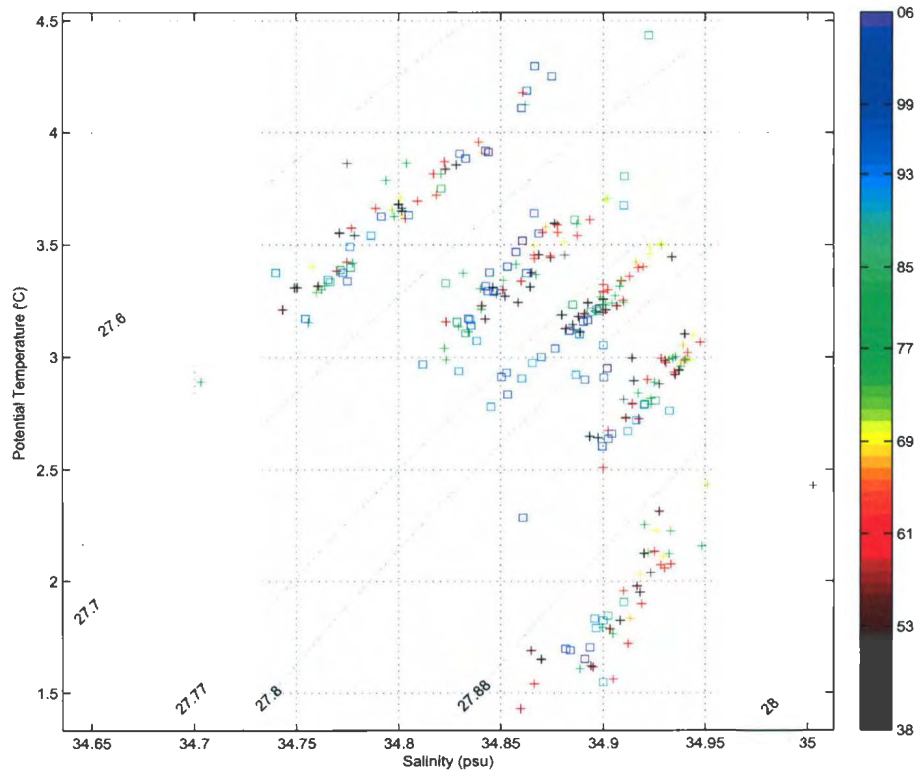


Figure 4.1. Annual mean potential temperature and salinity distributions in the CLS for the subsurface water masses. +'s and □'s are annual means during 1938-1984 and 1985-2006 respectively. In 1942-47 and 1982 there is no data for all water masses while some water masses also do not have data in other years.

anomaly referenced to 2000 dbar). Regarding the central Labrador Sea  $\theta$ - $S$  diagram in Figure 4.1, the mixing of ISOW with dLSW in 1992 is the onset of convection penetrating the ISOW layer, and in 1995 the mixing is the onset of ISOW upwelling from the horizontal divergence of the newly formed dLSW.

### 4.1.2 Inference for the Difference between the Mean States

Hypothesis testing between two independent, normally distributed populations having equal means and unequal variances forms the Behrens-Fisher problem. To infer a difference between two samples means,  $\bar{x}_1$  and  $\bar{x}_2$ , an approximate solution to the distribution of the Behrens Fisher statistic

$$T = \frac{\bar{x}_1 - \bar{x}_2}{\sqrt{s_1^2/n_1 + s_2^2/n_2}} \quad (4.1)$$

where  $s_1$  and  $s_2$  are the standard deviations of the two samples having sizes  $n_1$  and  $n_2$ , is found using Welch's t-test. Using this method allows for comparison of the approximated test statistic of  $T$  with the corresponding quantiles of the Student's t-distribution.

For each water mass in the northern LS, West Greenland Current, central LS, Labrador Current and southeast LS, the null hypothesis of 1938-1984 and 1985-2006 *non-normalized*  $S$ ,  $\theta$  and  $\sigma_\theta$  anomalies having equal means (but unequal variances) was tested using Welch's method. Although *a priori*, the water mass properties during the late 1980s will be influenced by the water mass properties of the early 1980s, the relatively long span of the two time periods, and constant water mass circulation and mixing within the basin, allow the assumption of independency. For ease of analysis in the hypothesis testing we must assume normality; although a stochastic system we must approximate it as deterministic. The null hypothesis is rejected at the 5% significance level with zero probability of observing the given Behren Fisher statistic

( $T$ ) for all  $S$ ,  $\theta$  and  $\sigma_\theta$  distributions.

## 4.2 Regime Shift: 1963-1973 and 1989-1999

We seek two time periods during which the sea-water properties are nearly homogeneous, with a time span such that there is a sufficient amount of data, but short enough such that there is no influence of decadal variability. Relative homogeneity in sea-water properties over one decade should be sufficient to essentially remove most long-term variability. Any remaining interannual variability should be somewhat similar in each period. Two 10-year, homogeneous periods are clear in vertical sections of  $S$ ,  $\theta$  and  $\sigma_\theta$  in the central LS during 1958-2002 as shown in [30] (Plate 7.3.6). During both 1963-1973 and 1989-1999, all subsurface water masses are nearly homogeneous with different mean states, and each contains one of the two most vigorous convective events on record.

In 1963-1973, the NAO index was predominantly negative [12], with very little subsurface convective renewal [8]. With no ventilation down to the sLSW and dLSW layers, the water masses in the central LS were isolated from mixing with the upper layers and ceased transporting excess heat to the surface layer. The LSW water was warming and salinifying by lateral mixing and exchange with surrounding water such as the subsurface West Greenland Current. This warm and saline period ended with the second most intense convective period on record with mixing deeper than 1500 m during the 1972-1973 winters [8].

During 1989-1999, the entire central LS water column was at its coldest and freshest state ever observed [6, 14, 23, 30]. The four year period of deep convection, 1990-1993, ended with the deepest convection ever observed on record in the winter of 1993 reaching depths greater than 2200 m [15, 6, 5]. Fresh, cold surface water

penetrated down to the ISOW layer (Figure 4.1) mixing with IW, sLSW, dLSW and ISOW in the process, producing the coldest and freshest central LS water column on the record. In 1994, the LSW (both sLSW and dLSW) reached a maximum thickness of  $\sim 1700$  m [6], or 1900 m [23] depending upon the defined hydrography of LSW. Following the cessation of convection after 1993, the LSW continually thinned from its 1994 maximum thickness to a minimum thickness of  $\sim 200$  m by 1999 [6] as the LSW was exported out of the basin. Consequent to the lateral divergence of dLSW, upwelling of ISOW began in 1995 (Figure 4.1).

### 4.3 Changes in Water Mass Variability

The  $\delta$  maps of the water masses for 1963-1973, 1989-1999, 1938-1984 and 1985-2006 are presented in Figures C.1-C.6. Including the  $\delta$  maps for 1938-2006 in the comparison, all five time periods clearly have differing  $S$  and  $\theta$  variability in the subsurface layers and similar variability in the surface layer. The calculated variability is a combination of temporal and spatial variability. The  $\delta$  maps are expected to be different in each time period since temporal variability is stochastic and each period is subject to different long-term variations in  $S$  and  $\theta$ .

#### 4.3.1 Surface layer

The boundary currents have large surface  $S$  variability, compared to the interior Labrador Sea, regardless of the time span. Most notably, the surface boundary currents have higher  $S$  variability in 1985-2006 (Figure C.1(j)), particularly in 1989-1999 (Figure C.1(d)), than in 1938-1984 (Figure C.1(g)). This suggests that interannual variability during 1989-1999, when convection switched from strong to weak, is the major contributor to the 1985-2006 variability. In the early and late 1990s, the central

LS was capped by a saltier surface layer and in roughly 1993-1996, a fresher layer [30]. Lateral exchange with boundary currents is the main source of  $S$  in the surface central LS [10], and therefore the boundary current salt content must have increased in the early and late 1990s. Since the primary influence of boundary current  $S$  variability is sea-ice/freshwater transport, and ice formation and melt, the LS experienced two interannual events of decreased freshwater influx from ice melt, and the Hudson and Davis Straits during 1989-1999.

The  $\delta(\theta)$  maps of the four shorter time periods imply most of the southeast LS and northern LS  $\theta$  variability during 1938-2006 (Figure 3.1(b)) is from interannual  $\theta$  variability during 1985-2006. This interannual variability is likely the result of the steady warming of the central LS surface layer from 1995 to 2005 [23]. Strong  $\theta$  variability is observed throughout the the LS except the northern LS in 1985-2006. It is noted in the northern LS, shoreward of the West Greenland Current, variability is minimal in all five  $\delta$  maps.

### 4.3.2 Intermediate layers

In the IW, sLSW and dLSW layers,  $S$  and  $\theta$  variability in 1938-1984 is distinctly different than the variability in 1985-2006. In the IW and sLSW layers, the 1985-2006  $\delta(S)$  and  $\delta(\theta)$  maps in Figures C.2(j,k) and C.3(j,k) most strongly resemble the respective 1938-2006  $\delta(S)$  and  $\delta(\theta)$  maps in Figures 3.1(d,e,g,h). In the dLSW layer, similarities are difficult to distinguish due to localized  $\delta(S)$  and  $\delta(\theta)$  maxima near  $53^\circ\text{N}$ ,  $53^\circ\text{W}$  in 1938-1984 (Figures C.4(g,h)) and near  $64^\circ\text{N}$ ,  $57^\circ\text{W}$  in 1985-2006 (Figures C.4(j,k)). The strength of these maxima essentially drowns out the variability signal throughout the LS. A lack of observations in region 1 during 1985-2006 is suggested for the cause of the  $\delta(S)$  and  $\delta(\theta)$  maxima in the northern LS dLSW

layer since (1) they overpower expected maxima at 53°N, 53°W from 1989-1999, and (2) they are not observed in the other time periods. However, a second source could be a significant, simultaneous increase or decrease in  $S$  and  $\theta$  from Davis Strait outflow after 1999.

### 4.3.3 Bottom water masses

Similar to the intermediate layers, the 1938-1984  $\delta(S)$  and  $\delta(\theta)$  in both bottom water masses differ from the variability in 1985-2006. Again, local maxima in the boundary currents drown out the signal in the rest of the LS, making it difficult to distinguish variability in the basin.

## 4.4 Changes in Water Mass Skewness

Figures D.1- D.6 in Appendix D show the water mass  $\gamma_3$  maps for 1963-1973, 1989-1999, 1938-1984 and 1985-2006. Thermohaline gradients within water masses, caused by mixing of sea-water properties, are described by the geographical distribution of  $S$  and  $\theta$  skewness. The mesoscale variability represented by the 1938-1984 and 1985-2006  $S$  and  $\theta$  skewness is influenced by the interannual and decadal variability of  $S$  and  $\theta$ . The mesoscale variability represented by the 1963-1973 and 1989-1999  $S$  and  $\theta$  skewness, however, is not influenced by long-term variability. The general  $\gamma_3(S)$  and  $\gamma_3(\theta)$  features generally remain throughout the five time periods, but most of the skewness in the 1963-1973 and 1989-1999 maps is statistically insignificant.

### 4.4.1 Limitations to the Analysis

Nearly all 1963-1973 and 1989-1999  $\gamma_3(S)$  and  $\gamma_3(\theta)$  maps have too many regions in which the skew is statistically insignificant, thus not allowing for proper analysis during these decades. Insignificant  $S$  and  $\theta$  skewness is particularly constraining in the subsurface layers. In the surface, IW, sLSW and dLSW water masses, the processes responsible for the prominent 1938-2006  $\gamma_3(S)$  and  $\gamma_3(\theta)$  (Figures 3.3) can be generally inferred in the 1963-1973 maps (Figures D.1(a,b), D.2(a,b), D.3(a,b) and D.4(a,b)) and in the 1989-1999 maps (Figures D.1(d,e), D.2(d,e), D.3(d,e) and D.4(d,e)) despite the insignificant skew. During both 1938-1984 and 1985-2006, the  $\gamma_3(S)$  and  $\gamma_3(\theta)$  features closely resemble the 1938-2006 features in the surface, IW and sLSW layers. Regions with significant  $\gamma_3(S)$  and  $\gamma_3(\theta)$  can be properly analyzed using stochastic dynamics, but we focus on only qualitatively describing the general observations.

Most of the variability in the ISOW and DSOW is temporal and long-term, rendering it difficult to interpret  $\gamma_3(S)$  and  $\gamma_3(\theta)$ . Decreasing the span of the time periods decreases the amount of available data, further adding to the difficulty in the interpretation. The  $S$  and  $\theta$  skewness in the ISOW and DSOW is mostly statistically insignificant and therefore the ISOW and DSOW  $\gamma_3$  maps for the shorter time periods will not be discussed.

### 4.4.2 Surface layer

The characteristic mesoscale variability described by the 1938-2006 surface  $\gamma_3(S)$  and  $\gamma_3(\theta)$  maps in Figures ??(a, b) is also observed during 1963-1973 and 1989-1999 (Figures D.1(a,b,d,e)) and during 1938-1984 and 1985-2006 (Figures D.1(g,h,j,k)). The  $\gamma_3(\theta)$  of the shorter time periods still capture the mixing of the northern LS and

southeast LS inflows with the central LS surface divergence of excess heat acquired from the subsurface layers.

The surface layer  $S$  is still dominated by negative skewness. As discussed in Section 3.2.1, the negative  $\gamma_3(S)$  and tendency toward stronger negative  $\gamma_3(S)$  in the basin is due to the influx of freshwater from the boundary currents. Also discussed was the observed relationship between  $S$  variability and skewness. In 1989-1999 and 1985-2006, the surface Labrador Current  $S$  is highly variable with a small magnitude skew. Large variations in sea-ice/freshwater transport, and sea-ice formation and melt occurred during 1989-1999. Mentioned in Section 4.3.1, the Labrador Current  $S$  increased during the early and late 1990s and decreased in the mid 1990s. More numerous higher  $S$  events act to shift the skewness away from any strong negative salinity events, causing the low magnitude, negative  $\gamma_3(S)$  during 1989-1999 (and in 1985-2006) in the Labrador Current.

#### 4.4.3 IW layer

Much of the IW  $\gamma_3(\theta)$  during each of the shorter time periods is statistically insignificant, yet a  $\gamma_3(\theta)$  distribution similar to that in 1938-2006 (Figure 3.3(e)) generally remains. In Figures D.2(e,k), positive  $\gamma_3(\theta)$  is prominent in the central LS during 1989-1999 and 1985-2006. As in the 1938-2006  $\gamma_3(\theta)$  map, the positive skew is the subsurface convergence of heat from the West Greenland Current bringing in warmer Irminger Sea Water. Each  $\gamma_3(S)$  map is also remarkably similar to the complete geographical  $\gamma_3(S)$  distribution shown in Figure 3.3(d). In the basin, the magnitude of the negative  $\gamma_3(S)$  is small compared to the magnitude in the LS boundaries. Simultaneous to eddy heat influx from the West Greenland Current, saltier waters are exchanged into the basin. The small magnitude  $\gamma_3(S)$  may indicate a continual con-

vergence of salt in the IW layer rather than the variable convergence of heat during the periods of restratification in the central LS. The lateral salt exchange between the basin and boundary currents during convection and restratification, however, has yet to be understood [10].

At the site of removal of convectively formed water near  $54^{\circ}\text{N}$   $52^{\circ}\text{W}$ , the strong negative  $\gamma_3(S)$  in 1938-2006 is only clearly observed in 1938-1984 and 1985-2006. In all  $\gamma_3(\theta)$  maps (Figures D.2(b,e,h,k)), this location is clearly distinct. During 1989-1999 and 1985-2006, a remarkably large  $\gamma_3(\theta)$  gradient separates large heat convergences in the basin as the cold convected water entrains in the warmer Labrador Current and exits the LS. This  $\gamma_3(\theta)$  feature is exclusive to 1989-1999 and 1985-2006 and is likely a mark of the intense deep convection during 1990-1993.

#### 4.4.4 sLSW and dLSW layers

As in the IW layer, the same feature of water removal is coherent near  $54^{\circ}\text{N}$   $52^{\circ}\text{W}$  in every  $\gamma_3(S)$  map (Figures D.3(a,d,g,j)) and in every  $\gamma_3(\theta)$  map (Figures D.3(b,e,h,k)) in the sLSW layer, regardless of time span. During 1963-1973 this site is still inferred but nearly all  $S$  and  $\theta$  skewness is statistically insignificant. The small negative skew is likely from the export of sLSW formed prior to 1963 since no convection reached this layer during 1963-1973 until 1972-1973. In the dLSW layer, the location of LSW export is also clear. The location is curiously prominent in Figure D.4(d,e) but not in Figures D.4(a,b). Deep convection down to the dLSW layer in 1993 produced an abundance of dLSW which was exported out of the basin in consequent years, whereas in 1963-1973, dLSW product was not formed until 1972-1973.

The positive dLSW  $\gamma_3(S)$  and  $\gamma_3(\theta)$  near  $55^{\circ}\text{N}$ ,  $54^{\circ}\text{W}$  in the 1938-2006  $\gamma_3$  maps is not observed in either the 1989-1999 or 1985-2006  $\gamma_3$  maps. In Section 3.2.2, it was

hypothesized that this localized positive skew was representative of ISOW upwelling following intense convective events, specifically since the most intense convective period ever observed in 1990-93 led to ISOW upwelling in 1995 (Figure 4.1). If this were the case, however, some indication of the feature is expected in both the 1989-1999 and 1985-2006  $\gamma_3$  maps. The feature is instead relatively distinct in the 1963-1973  $\gamma_3$  maps. In the late 1960s - early 1970s, there was no ISOW upwelling. The LSW layer had a thickness of only  $\sim 600$  m [23] and was not even penetrated by convection until 1972-1973. The cause of the localized positive  $\gamma_3(S)$  and  $\gamma_3(\theta)$  is therefore unclear and not attributed to ISOW upwelling.

## 4.5 Summary

The  $\delta(S)$  and  $\delta(\theta)$  maps of the LS water masses show that each of the time periods 1938-2006, 1938-1984, 1985-2006, 1963-1973 and 1989-1999 have a different spatial distribution of variability, except in the surface layer  $S$  and  $\sigma_\theta$ . In each period, the climatological  $S$  forcing in the LS greatly impacts the surface boundary currents and warm inflow from the Atlantic Ocean impacts the southern LS. This indicates each period has similar temporal variability in the surface layer since the distribution of mesoscale variability should not change. The geographical distributions of variability are increasingly different as water mass density increases. Although the stochastic nature of temporal variability implies a different distribution in each time period, the large local maxima in the dLSW, ISOW and DSOW in 1938-1984 and 1985-2006 make it difficult to properly analyze the changes in the dLSW, ISOW and DSOW  $\delta$  maps.

In all five time periods, the geographical distribution of  $\gamma_3(S)$  and  $\gamma_3(\theta)$  for the surface layer, IW layer and sLSW layer show similar thermohaline gradients within

the water masses, resulting from mixing of  $\theta - S$  characteristics. The characteristic mesoscale variability during 1938-2006 is clear in each of the shorter-periods  $\gamma_3$  maps. In the surface layer, dominant negative  $\gamma_3(S)$  and mixing of the colder northern LS and warmer southeast LS inflows with the central LS waters is remarkable in each  $\gamma_3$  map. Negative  $\gamma_3(S)$  also dominates the IW layer, and in the IW  $\gamma_3(\theta)$  maps, the central LS  $\theta$  continues to exhibit a tendency toward positive skewness. Near  $54^\circ\text{N}$   $52^\circ\text{W}$  in both the IW and sLSW layers, the site of removal of convectively formed water is coherent in nearly all the  $\gamma_3(S)$  and  $\gamma_3(\theta)$  maps. In the IW 1963-1973 and 1989-1999  $\gamma_3(S)$  maps and sLSW 1963-1973  $\gamma_3(S)$  and  $\gamma_3(\theta)$  maps it is not prominent.

Accuracy in estimating skewness and its statistical significance is dependent upon a sufficiently large data set. The number of observations generally decrease with depth and further decrease in shorter time spans. These limitations are apparent in the 1963-1973 and 1989-1999  $\gamma_3$  maps in which nearly every region has statistically insignificant  $S$  and  $\theta$  skewness. With respect to the 1938-2006 distributions of skewness, the shorter-period distributions are increasingly different over water mass depth, showing the effect of data sparsity on the skewness estimator ( $\gamma_3$ ).

# Chapter 5

## Discussion and Conclusions

The goal of this study is to analyze the geographical distribution of variability in the hydrography of the Labrador Sea using the 2nd and 3rd statistical central moments of salinity ( $S$ ), potential temperature ( $\theta$ ), and potential density ( $\sigma_\theta$ ).

### 5.1 Summary of Variability and Skewness

We have shown that the skewness of the low-frequency salinity and potential temperature fields in the Labrador Sea can be used to distinguish the mesoscale variability. The location of ocean processes subject to strong long-term temporal variability are well known within the Labrador Sea. *A posteriori* knowledge of this mesoscale and temporal variability aid us in our attempt to interpret what  $S$  and  $\theta$  skewness represents.

Analysis of the standard deviation ( $\delta$ ) maps of 1938-2006, 1938-1984, 1985-2006, 1963-1973 and 1989-1999 shows how the geographical distribution of variability changes for different time periods. The  $\delta$  maps describe the combination of spatial and temporal  $S$ ,  $\theta$  and  $\sigma_\theta$  variability and are therefore different in each of the five periods.

The distribution of variability is similar in each of the surface layer  $\delta(S)$  and  $\delta(\theta)$  maps; in each period, the surface boundary currents are the most influenced by  $S$  variations, and in the central/southern Labrador Sea,  $\theta$  variations are greatest from warmer inflow in the southeastern Labrador Sea. The similarity in the surface  $\delta$  maps is likely from a near-annual signal, longer than the seasonal signal but shorter than interannual-type signals. The geographical distributions of variability do become increasingly different among the five time periods as the water mass density increases. This is expected since long-term variability is mostly contained in subsurface layers [10].

To test the temporal dependency of  $\gamma_3$  we calculate the  $\gamma_3$  maps for (1) 1938-1984 and 1985-2006, in which  $S$  and  $\theta$  are subject to different long-term variability compared to in 1938-2006, and for (2) 1963-1973 and 1989-1999, in which sea-water properties are nearly homogeneous and essentially not subject to interannual variability. In the surface, IW, sLSW and dLSW layers, the geographical distribution of  $\gamma_3(S)$  and  $\gamma_3(\theta)$  in the four shorter periods are remarkably similar to  $\gamma_3$  distributions of 1938-2006:

- Negative  $\gamma_3(S)$  dominates the surface layer and IW layer.
- In the surface layer,  $\gamma_3(\theta)$  exhibits the relative temperature contrast between the colder northern LS and warmer southeast LS inflows mixing with the central LS waters.
- The convergence of heat toward the central LS from the boundary currents is distinguished in the IW layer.
- Coherent  $S$  and  $\theta$  skewness near  $54^\circ\text{N } 52^\circ\text{W}$  in the IW, sLSW, and dLSW layers represents the location in which the product of (deep) convection is exported

from the Labrador Sea into the North Atlantic current system.

In the 1963-1973 and 1989-1999 maps, however, the skewness in most of the 22 regions is statistically insignificant. Thus, we cannot conclude that skewness is independent of interannual and decadal variability, but rather we state it is *likely* that mainly mesoscale variability is represented in the spatial distribution of  $S$  and  $\theta$  skewness.

## 5.2 Future Work and Recommendations

The 3rd central moment is not a robust estimator of skewness. Higher-order central moments are sensitive to extreme values and outliers. In oceanography, many regions of the ocean are infrequently sampled leading to frequent outliers and extreme values in data. This is of utmost importance in the deep and abyssal ocean where hydrographic measurements are infrequent and widely separated.

A lack of data is a fundamental concern in this analysis. Many regions within the Labrador Sea are sparsely sampled, particularly depending upon the year, season and depth. Comparing the geographical distribution of skewness during four shorter time periods suitable for the purpose of this study is difficult. The amount of available data during 1963-1973 and 1989-1999 compared to the entire data set is the main cause for the resulting insignificant skewness in most of the Labrador Sea during these decades. Future studies should involve other methods to estimate skewness.

Other estimators of skewness have been postulated and studied. The method of  $L$ -moments [31] are analogous to central moments but use linear combinations of order statistics (hence the prefix  $L$ ).  $L$ -moments are less subject to bias in estimation and approximate their asymptotic normal distribution more closely [31]. The analog to the 3rd moment is  $L$ -skewness. Being more robust from the effects of sampling variability, greater accuracy in the geographical distributions of salinity and potential

temperature skewness can be obtained, particularly in the deep ocean.

### 5.3 Implications of the Project

In both observational and modeling applications, it is mathematically convenient to assume normally distributed sea-water properties. It is implicit to this assumption (1) that the governing dynamical systems of the ocean processes are linear and (2) the types of statistical significance tests used in statistical analysis of hydrographic data are of a normal distribution. Both observationally and theoretically it is impractical to assume normality if one is interested in understanding the stochastic dynamics inherent in the ocean, atmosphere and climate system.

The classically known mesoscale features in the Labrador Sea are distinguished in the geographical distribution of salinity skewness and potential temperature skewness. These features are associated with salinity and potential temperature frequency distributions significantly different from a normal distribution. The statistically significant departure from normality implies changing the treatment of salinity and potential temperature in both statistical circulation models of the Labrador Sea and statistical significance tests of hydrographic data.

## Bibliography

- [1] J. Gascard and R. Clarke. The formation of labrador sea water. part ii: Mesoscale and smaller-scale processes. *Journal of Physical Oceanography*, 13:1779–1797, 1983.
- [2] L. Talley and M. McCartney. Distribution and circulation of labrador sea water. *Journal of Physical Oceanography*, 12:1189–1205, 1982.
- [3] K. Lavender; R. Davis and W. Owens. Mid-depth recirculation observed in the interior labrador and irmindere seas by direct velocity measurements. *Nature*, 407:66–68, 2000.
- [4] K. Lavender; W. Owens and R. Davis. The mid-depth circulation of the subpolar north atlantic ocean as measured by subsurface floats. *Deep Sea Research I*, 52:767–785, 2005.
- [5] The Lab Sea Group. The labrador sea deep convection experiment. *Bulletin of the American Meteorological Society*, 79:2003–2058, 1998.
- [6] J. Lazier; R. Hendry; A. Clarke; I. Yashayaev and P. Rhines. Convection and restratification in the labrador sea, 1990-2000. *Deep Sea Research I*, 49:1819–1835, 2002.

- [7] S. Sathiyamoorthy and G. Moore. Buoyancy flux at ocean weather station bravo. *Journal of Physical Oceanography*, 32:458–474, 2002.
- [8] J. Lazier. Oceanographic conditions at ocean weather ship *Bravo* 1964-1974. *Atmosphere-Ocean*, 18:227–238, 1980.
- [9] J. Lilly; P. Rhines; F. Schott; K. Lavender; J. Lazier; U. Send and E. D’Asaro. Observations of the labrador sea eddy field. *Progress in Oceanography*, 59:75–176, 2003.
- [10] F. Straneo. Heat and freshwater transport through the central labrador sea. *Journal of Physical Oceanography*, 36:606–628, 2006.
- [11] I. Yashayaev. Hydrographic changes in the labrador sea, 1960-2005. *Progress in Oceanography*, 73:242–276, 2007.
- [12] J. Marshall and F. Schott. Open-ocean convection: Observations, theory, and model. *Reviews of Geophysics*, 37:1–64, 1999.
- [13] R. Pickart; D. Torres and R. Clarke. Hydrography of the labrador sea during active convection. *Journal of Physical Oceanography*, 32:428–457, 2002.
- [14] L. Stramma; D. Kieke; M. Rhein; F. Schott; I. Yashayaev and K. Koltermann. Deep water changes at the western boundary of the subpolar north atlantic during 1996-2001. *Deep Sea Research I*, 51:1033–1056, 2004.
- [15] J. Lilly; P. Rhines; M. Visbeck; R. Davis; J. Lazier; F. Schott and D. Farmer. Observing deep convection in the labrador sea during winter 1994/1995. *Journal of Physical Oceanography*, 29:2065–2098, 1999.
- [16] J. Lilly and P. Rhines. Coherent eddies in the labrador sea observed from a mooring. *Journal of Physical Oceanography*, 32:585–598, 2002.

- [17] M. Prater. Eddies in the labrador sea as observed by profiling rafos floats and remote sensing. *Journal of Physical Oceanography*, 32:411–427, 2002.
- [18] R. Pickart; M. Spall and J. Lazier. Mid-depth ventilation in the western boundary current system of the sub-polar gyre. *Deep-Sea Research I*, 44:1025–1054, 1997.
- [19] J. Marshall; Y. Kushnir; D. Battisti; P. Chang; A. Czaja; R. Dickson; J. Hurrell; M. McCartney; R. Saravanan and M. Visbeck. North atlantic climate variability: Phenomena, impacts and mechanisms. *International Journal of Climatology*, 21:1863–1898, 2001.
- [20] R. Greatbatch. The north atlantic oscillation. *Stochastic Environmental Research and Risk Assessment*, 14:213–242, 2002.
- [21] R. Curry and M. McCartney. Ocean gyre circulation changes associated with the north atlantic oscillation. *Journal of Physical Oceanography*, 31:3374–3400, 2001.
- [22] R. Dickson and J. Brown. The production of north atlantic deep water: Sources, rates and pathways. *Journal of Geophysical Research*, 99:2319–2341, 1994.
- [23] I. Yashayaev. Changing freshwater content: Insights from the subpolar north atlantic and new oceanographic challenges. *Progress in Oceanography*, 73:203–209, 2007.
- [24] C. Mauritzen. Production of dense overflow waters feeding the north atlantic across the greenland-scotland ridge. part 1: Evidence for a revised circulation scheme. *Deep-Sea Research I*, 43:769–806, 1996.
- [25] C. Brooks and N. Carruthers. *Handbook of Statistical Methods in Meteorology*. Her Majesty's Stationary Office, 1978.

- [26] C. Deser; M. Holland; G. Reverdin and M. Timlin. Decadal variations in labrador sea ice cover and north atlantic sea surface temperatures. *Journal of Geophysical Research*, 107:3.1–3.13, 2002.
- [27] R. Houghton and M. Visbeck. Quasi-decadal salinity fluctuations in the labrador sea. *Journal of Physical Oceanography*, 32:687–701, 2002.
- [28] R. Dickson; J. Lazier; J. Meincke; P. Rhines and J. Swift. Long-term coordinated changes in the convective activity of the north atlantic. *Progress in Oceanography*, 38:241-295, 1996.
- [29] B. Dickson; I. Yashayaev; J. Meincke; B. Turrell; S. Dye and J. Holfort. Rapid freshening of the deep north atlantic ocean over the past four decades. *Nature*, 416:832–836, 2002.
- [30] B. Dickson; J. Hurrell; N. Bindoff; A. Wong; B. Arbic; B. Owens; S. Imawaki and I. Yashayaev. The world during woce. In G. Siedler; J. Church and J. Gould, editors, *Ocean Circulation & Climate: Observing and Modelling the Global Ocean*. Academic Press, 2001.
- [31] J. Hosking. L-moments: Analysis and estimation of distributions using linear combinations of order statistics. *Journal of the Royal Statistical Society B*, 52:105–124, 1990.

# Appendix

## Appendix A: Probability Density Distributions

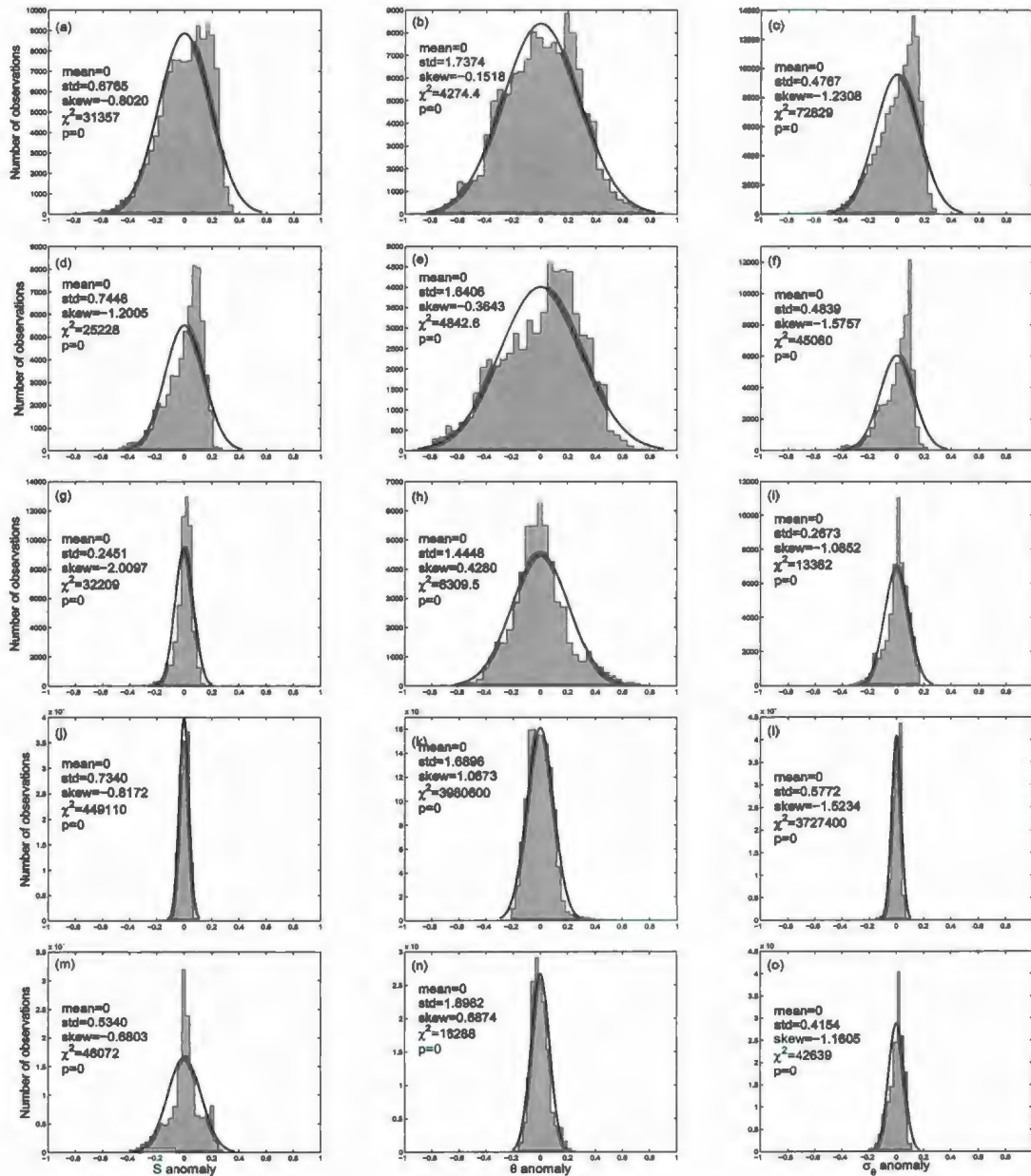


Figure .1. Histograms (40 bins) of 1938-2006 surface layer salinity, potential temperature and potential density anomalies respectively for NLS (a,b,c), WGC (d,e,f), CLS (g,h,i), LC (j,k,l) and SELS (m,n,o). Anomalies have been normalized by the maximum amplitude prior to binning. Thick black curves are the normal distributions having the same means and standard deviations as the histograms. The *non-normalized* anomaly moments,  $\chi^2$  statistic and associated p-value are shown.

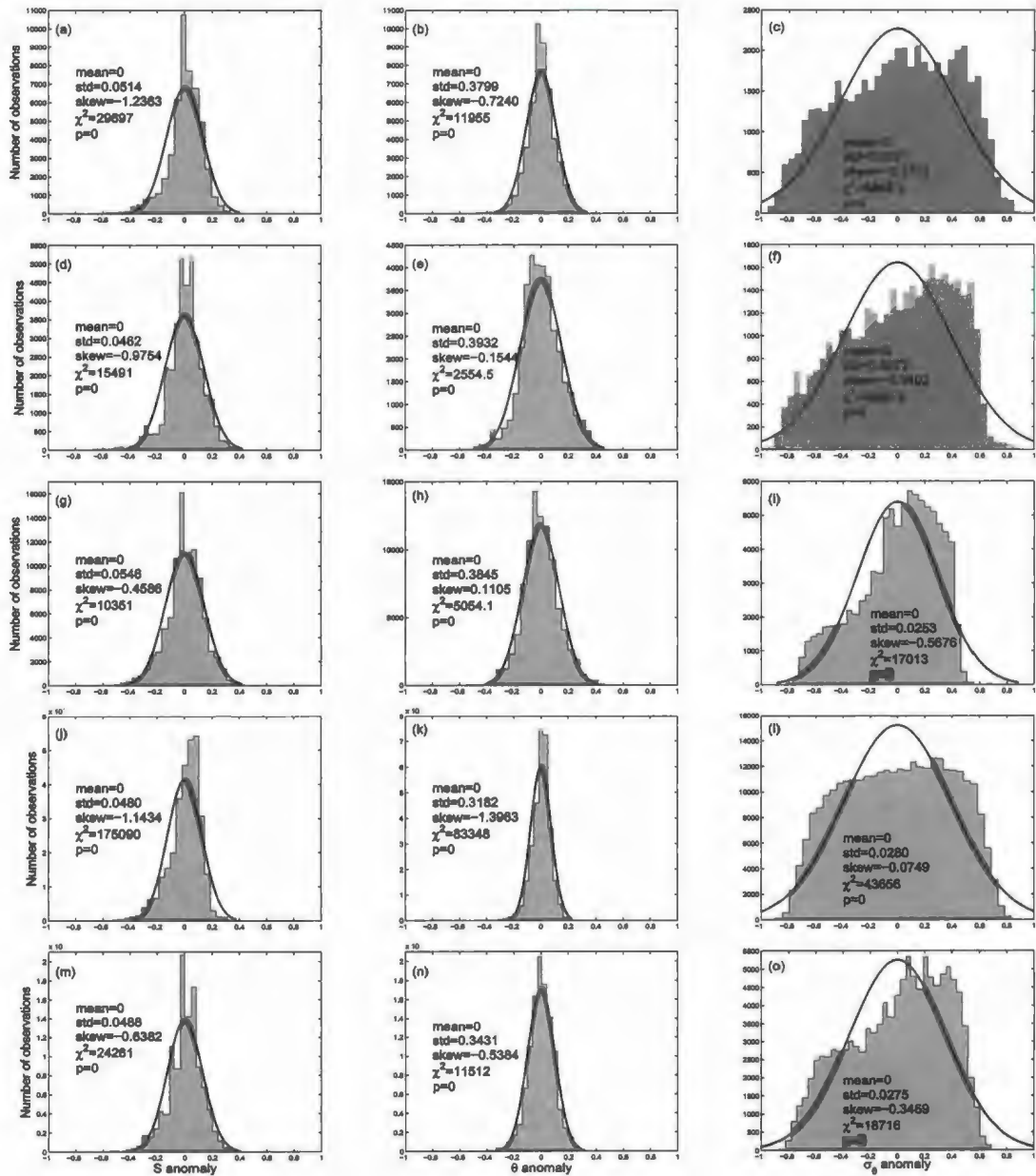


Figure .2. Histograms (40 bins) of 1938-2006 Irminger water salinity, potential temperature and potential density anomalies respectively for NLS (a,b,c), WGC (d,e,f), CLS (g,h,i), LC (j,k,l) and SELS (m,n,o). Anomalies have been normalized by the maximum amplitude. Thick black curves are the normal distributions having the same means and standard deviations as the histograms. The *non-normalized* anomaly moments,  $\chi^2$  statistic and associated p-value are shown.

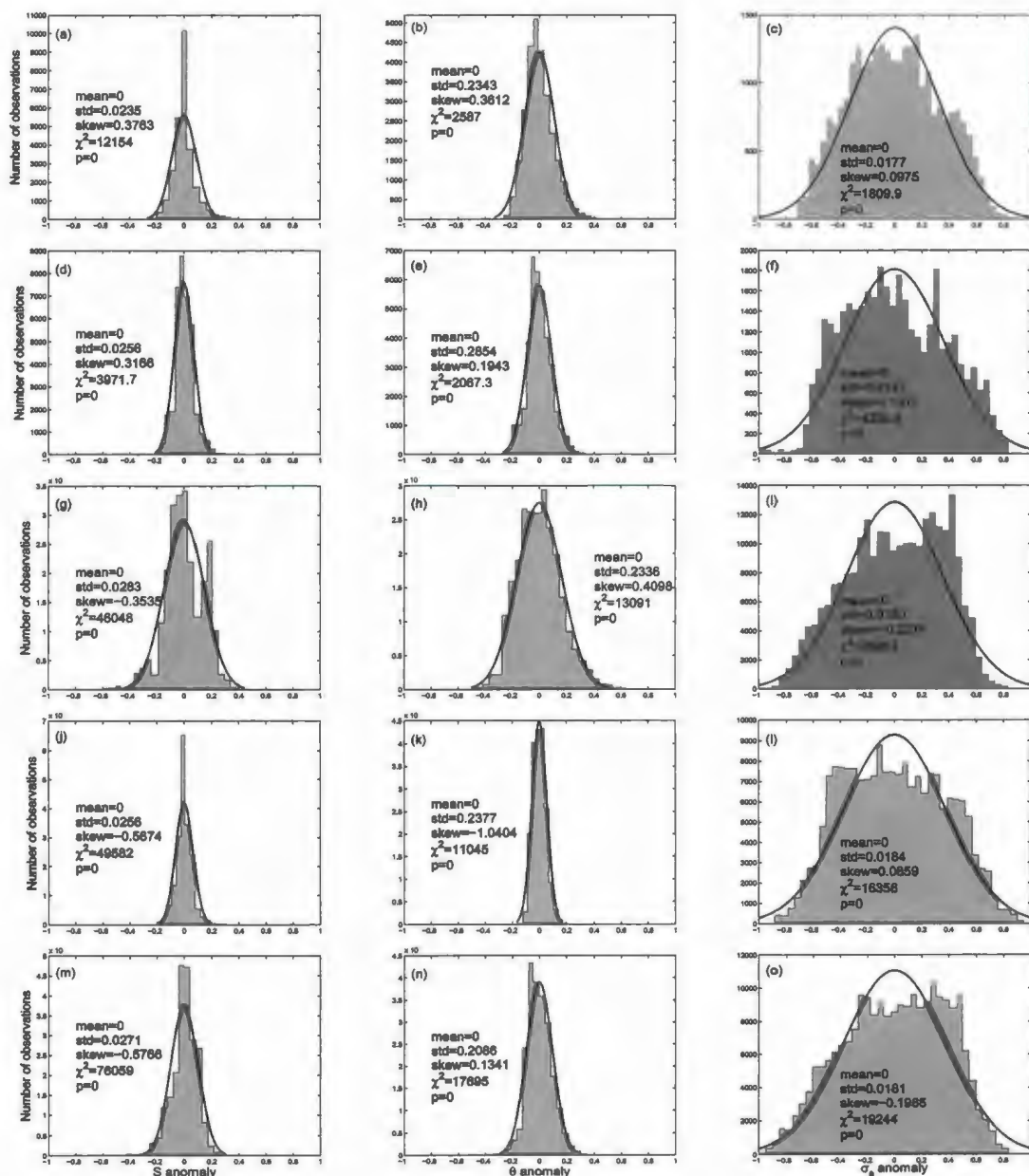


Figure .3. Histograms (40 bins) of 1938-2006 shallow Labrador Sea water salinity, potential temperature and potential density anomalies respectively for NLS (a,b,c), WGC (d,e,f), CLS (g,h,i), LC (j,k,l) and SELS (m,n,o). Anomalies have been normalized by the maximum amplitude. Thick black curves are the normal distributions having the same means and standard deviations as the histograms. The *non-normalized* anomaly moments,  $\chi^2$  statistic and associated p-value are shown.

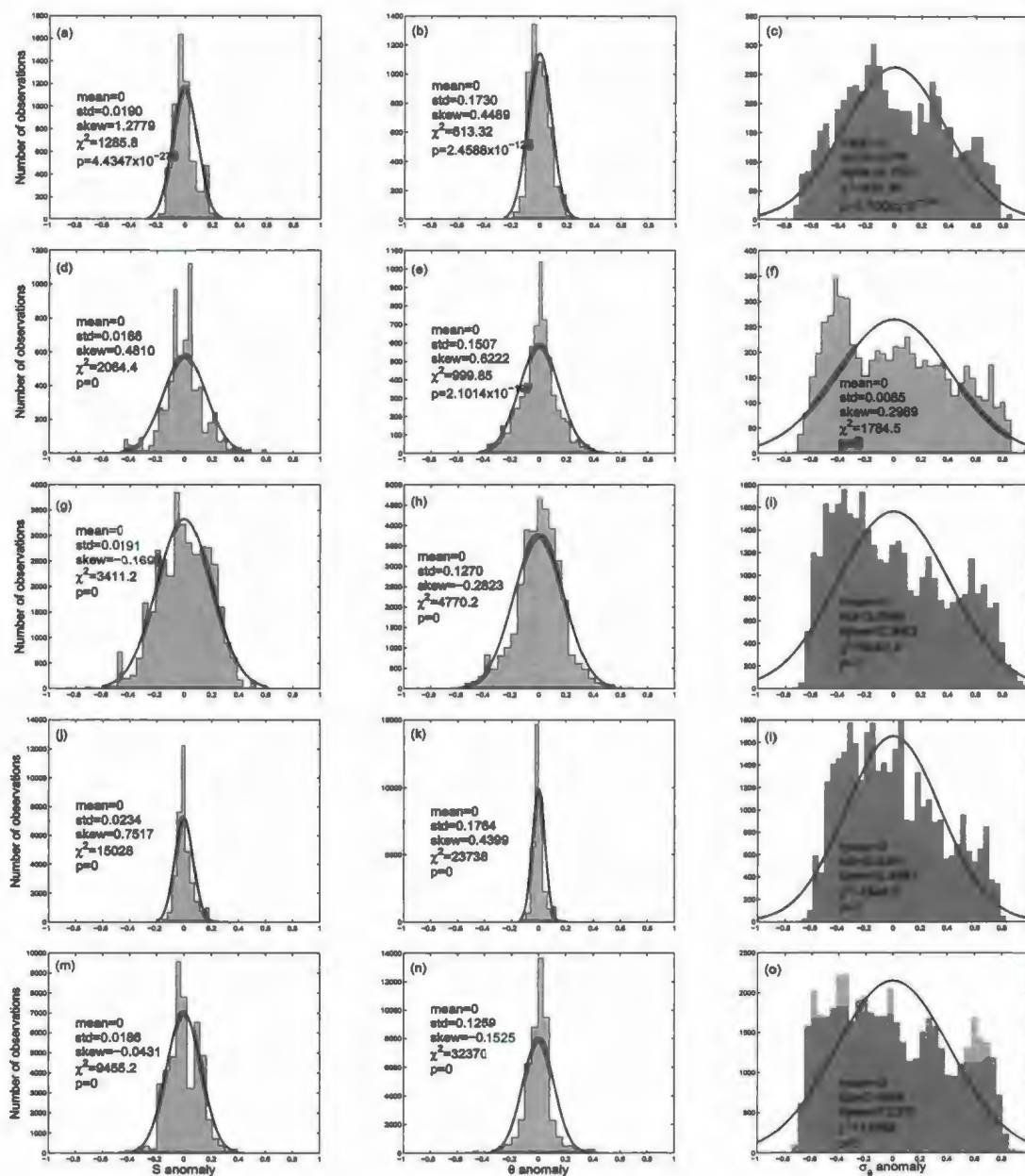


Figure .4. Histograms (40 bins) of 1938-2006 deep Labrador Sea water salinity, potential temperature and potential density anomalies respectively for NLS (a,b,c), WGC (d,e,f), CLS (g,h,i), LC (j,k,l) and SELS (m,n,o). Anomalies have been normalized by the maximum amplitude. Thick black curves are the normal distributions having the same means and standard deviations as the histograms. The *non-normalized* anomaly moments,  $\chi^2$  statistic and associated p-value are shown.

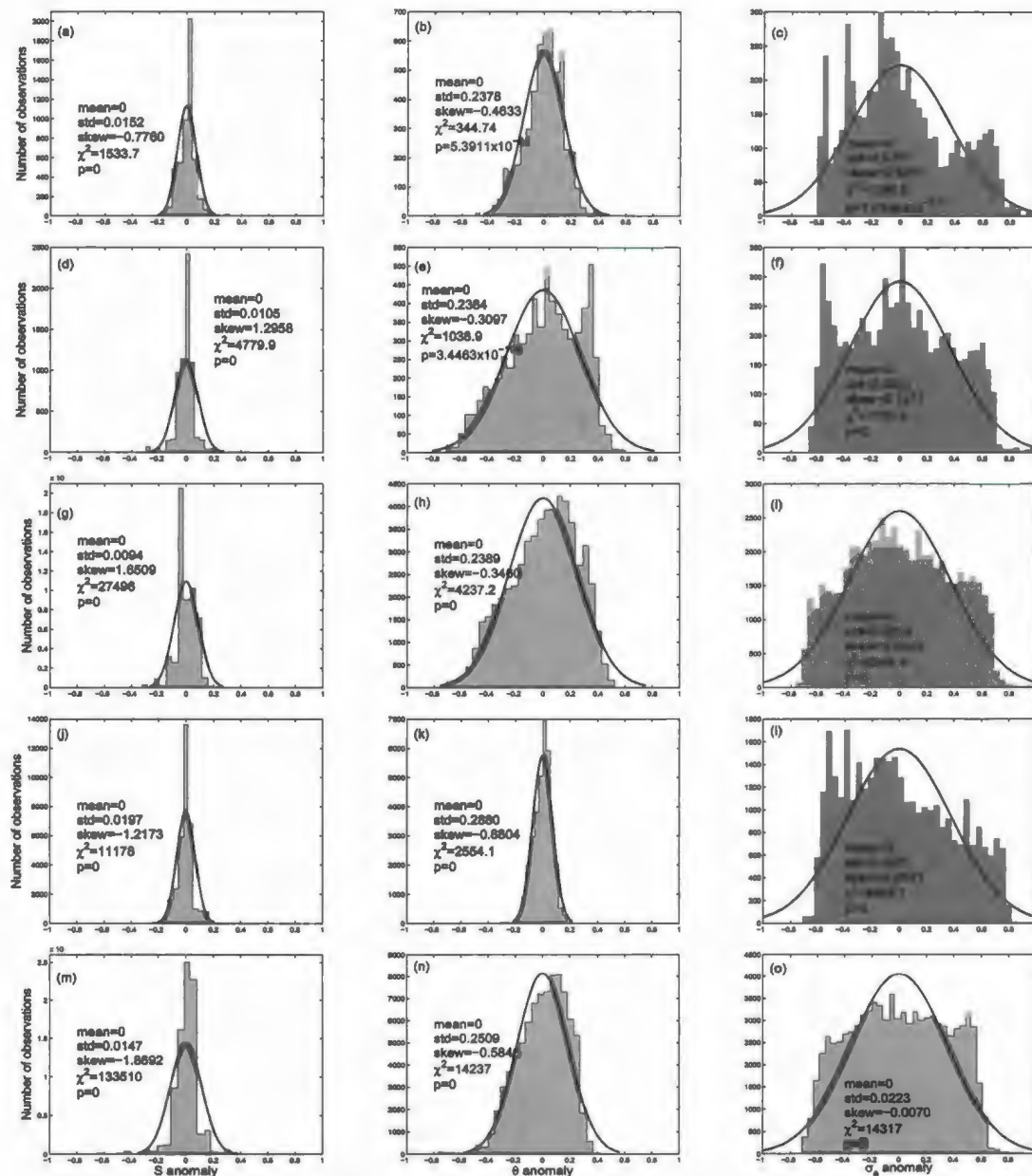


Figure 5. Histograms (40 bins) of 1938-2006 Iceland-Scotland Overflow water salinity, potential temperature and potential density anomalies respectively for NLS (a,b,c), WGC (d,e,f), CLS (g,h,i), LC (j,k,l) and SELS (m,n,o). Anomalies have been normalized by the maximum amplitude. Thick black curves are the normal distributions having the same means and standard deviations as the histograms. The *non-normalized* anomaly moments,  $\chi^2$  statistic and associated p-value are shown.

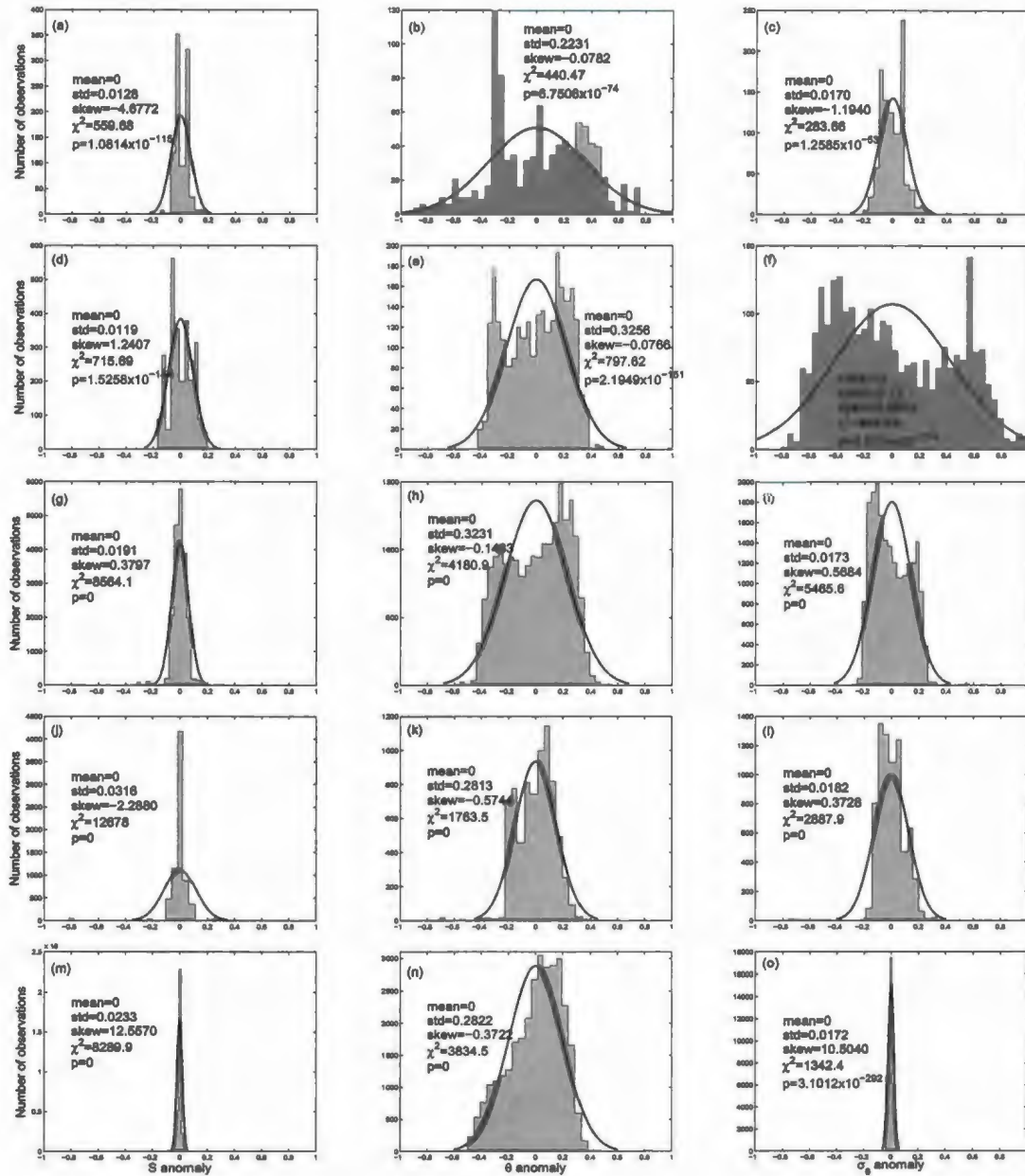


Figure .6. Histograms (40 bins) of 1938-2006 Denmark Strait Overflow water salinity, potential temperature and potential density anomalies respectively for NLS (a,b,c), WGC (d,e,f), CLS (g,h,i), LC (j,k,l) and SELS (m,n,o). Anomalies have been normalized by the maximum amplitude. Thick black curves are the normal distributions having the same means and standard deviations as the histograms. The *non-normalized* anomaly moments,  $\chi^2$  statistic and associated p-value are shown.

# Appendix

## Appendix B: TS Diagrams

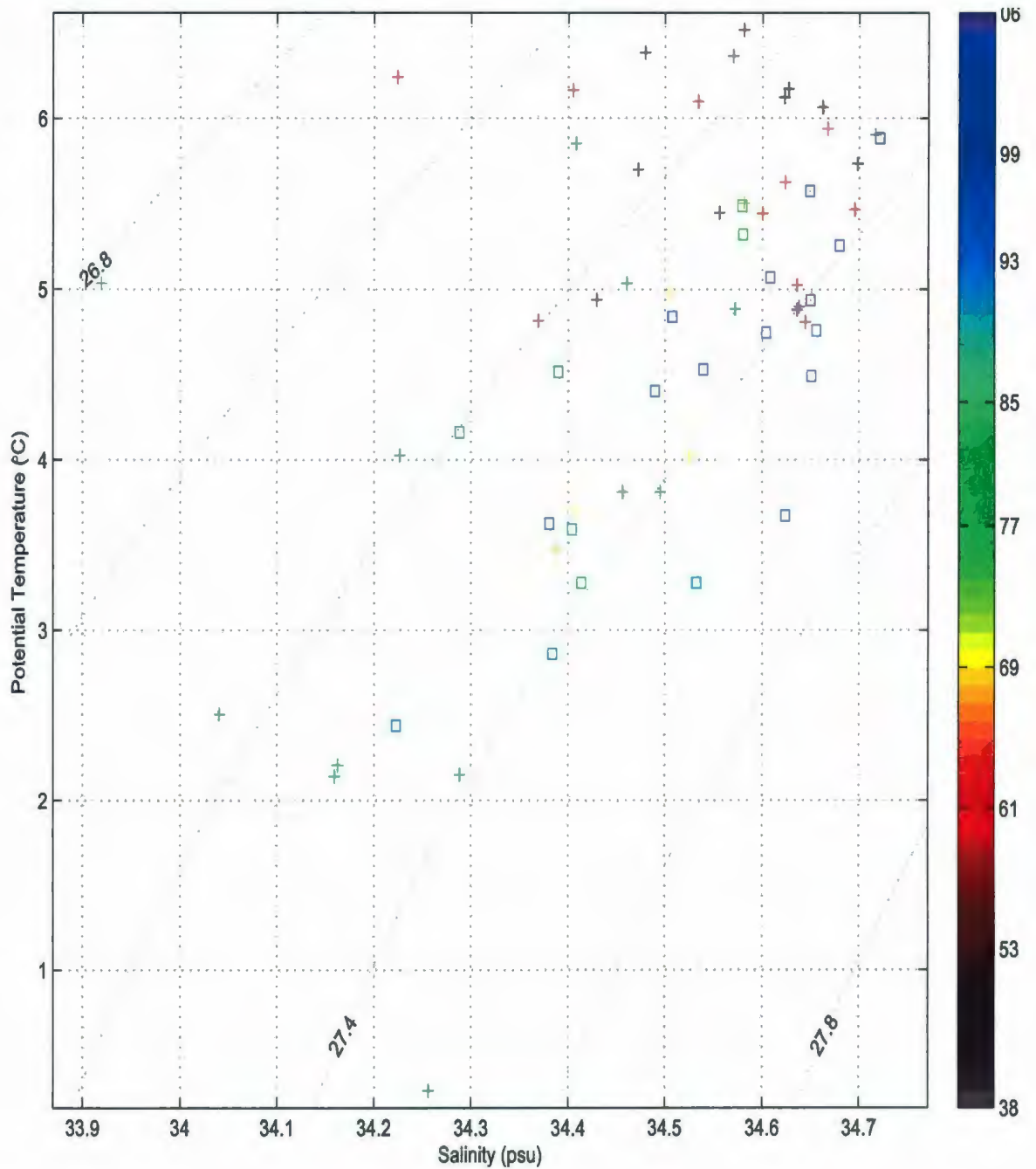


Figure .1. Surface layer annual mean potential temperature and salinity distribution in the CLS where +’s and □’s are annual means during 1938-84 and 1985-06 respectively. No data exists in 1942-47 and 1982.

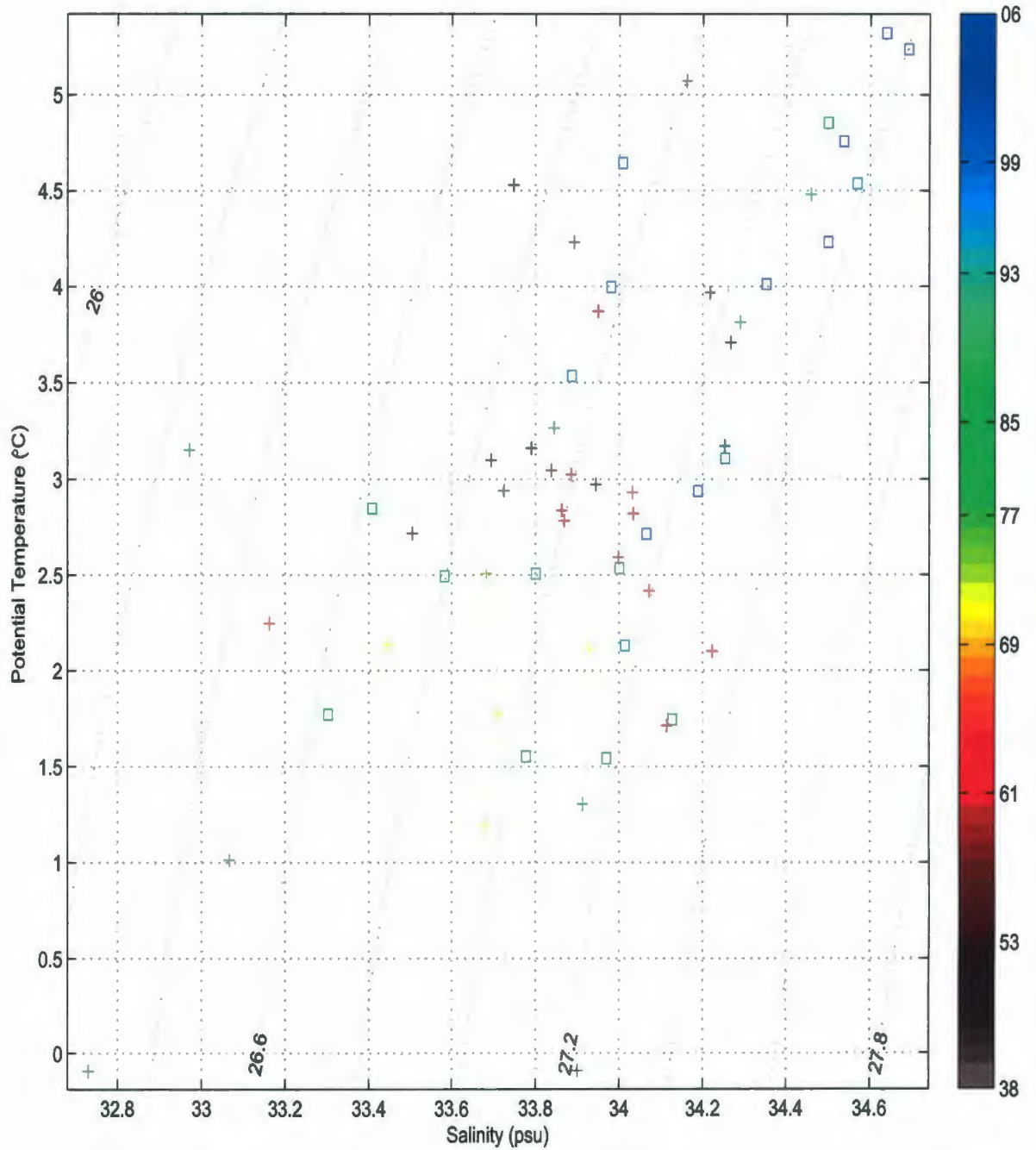


Figure .2. Surface layer annual mean potential temperature and salinity distribution in the WGC where +’s and □’s are annual means during 1938-84 and 1985-06 respectively. No data exists in 1939-45, 1976, 1978, and 1982-83.

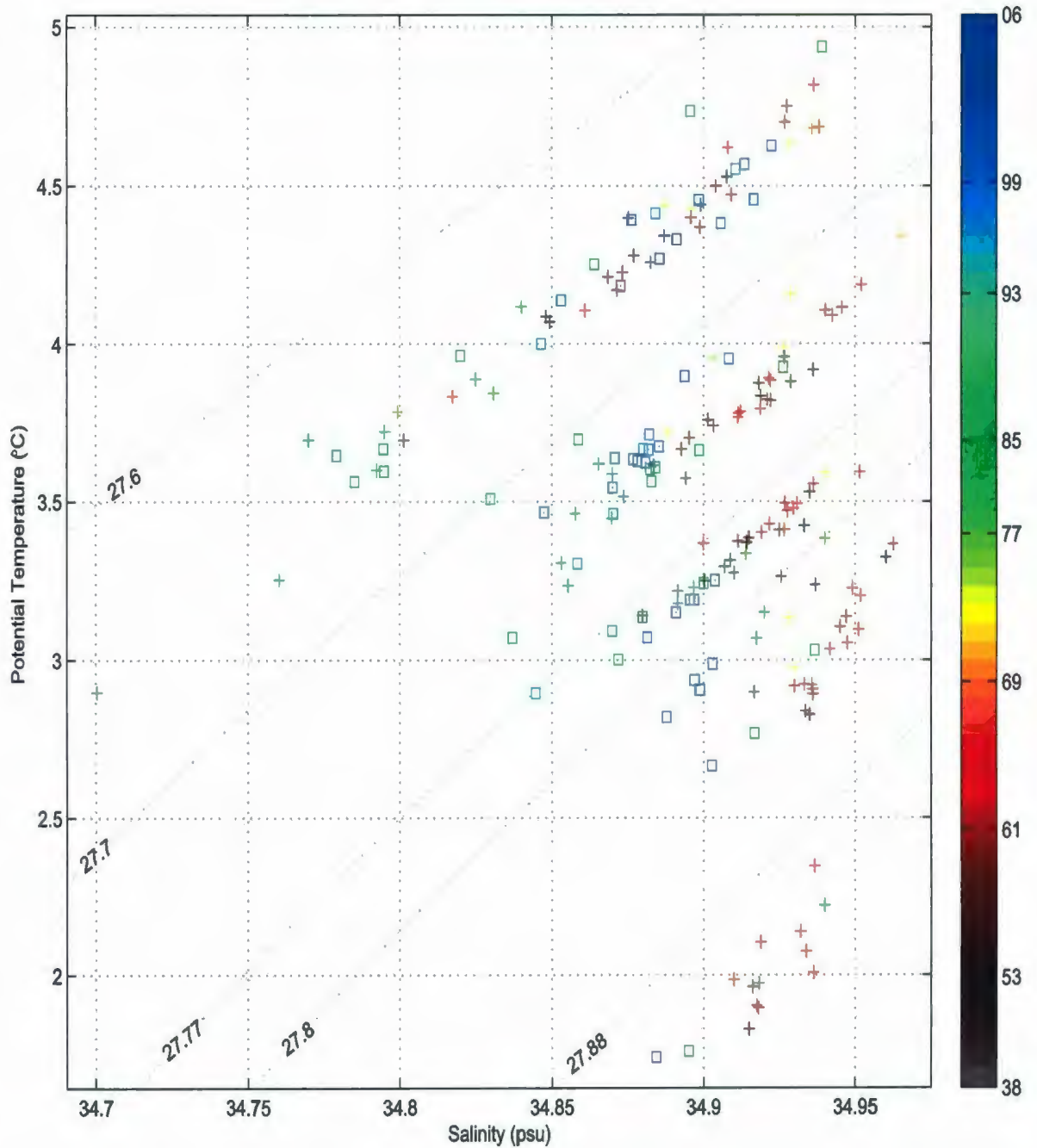


Figure .3. Annual mean potential temperature and salinity distributions in the WGC for the subsurface water masses. +’s and □’s are annual means during 1938-84 and 1985-06 respectively. In 1939-45, 1947, 1976 and 1982-83 there is no data for all water masses while some water masses also do not have data in other years.

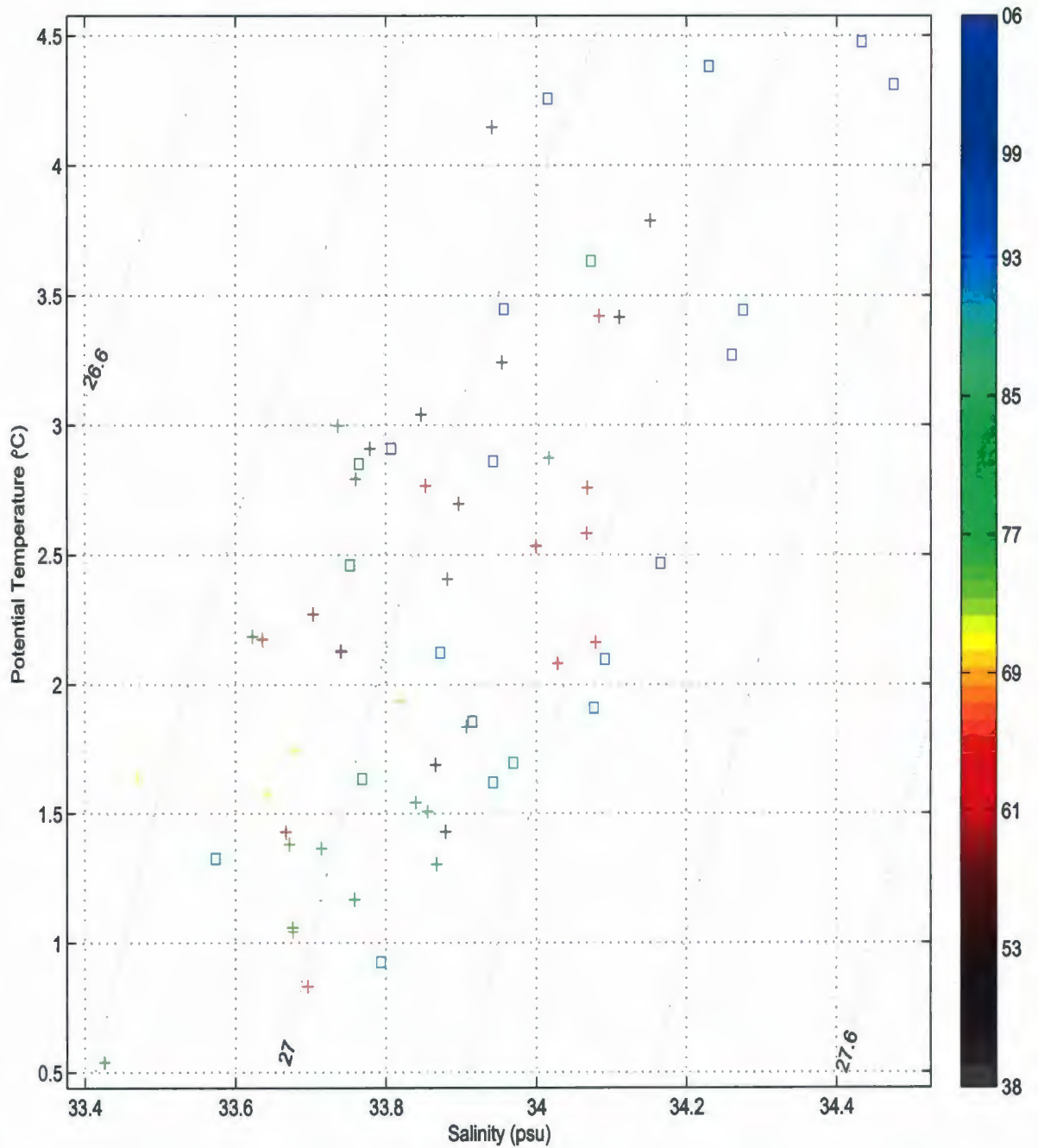


Figure .4. Surface layer annual mean potential temperature and salinity distribution in the NLS where +’s and □’s are annual means during 1938-84 and 1985-06 respectively. No data exists in 1939-45.

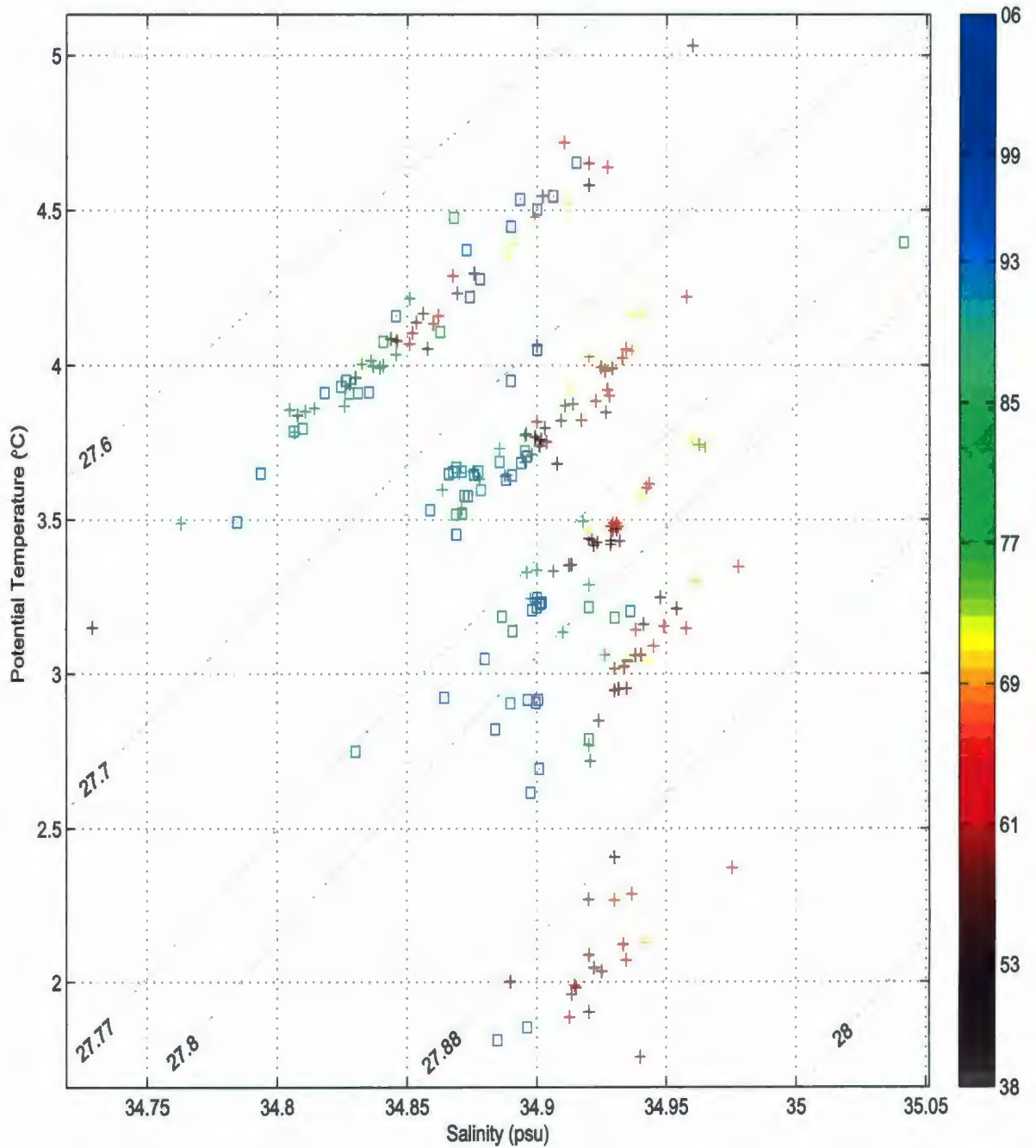


Figure .5. Annual mean potential temperature and salinity distributions in the NLS for the subsurface water masses. +'s and □'s are annual means during 1938-84 and 1985-06 respectively. In 1939-45 and 1947 there is no data for all water masses while some water masses also do not have data in other years.

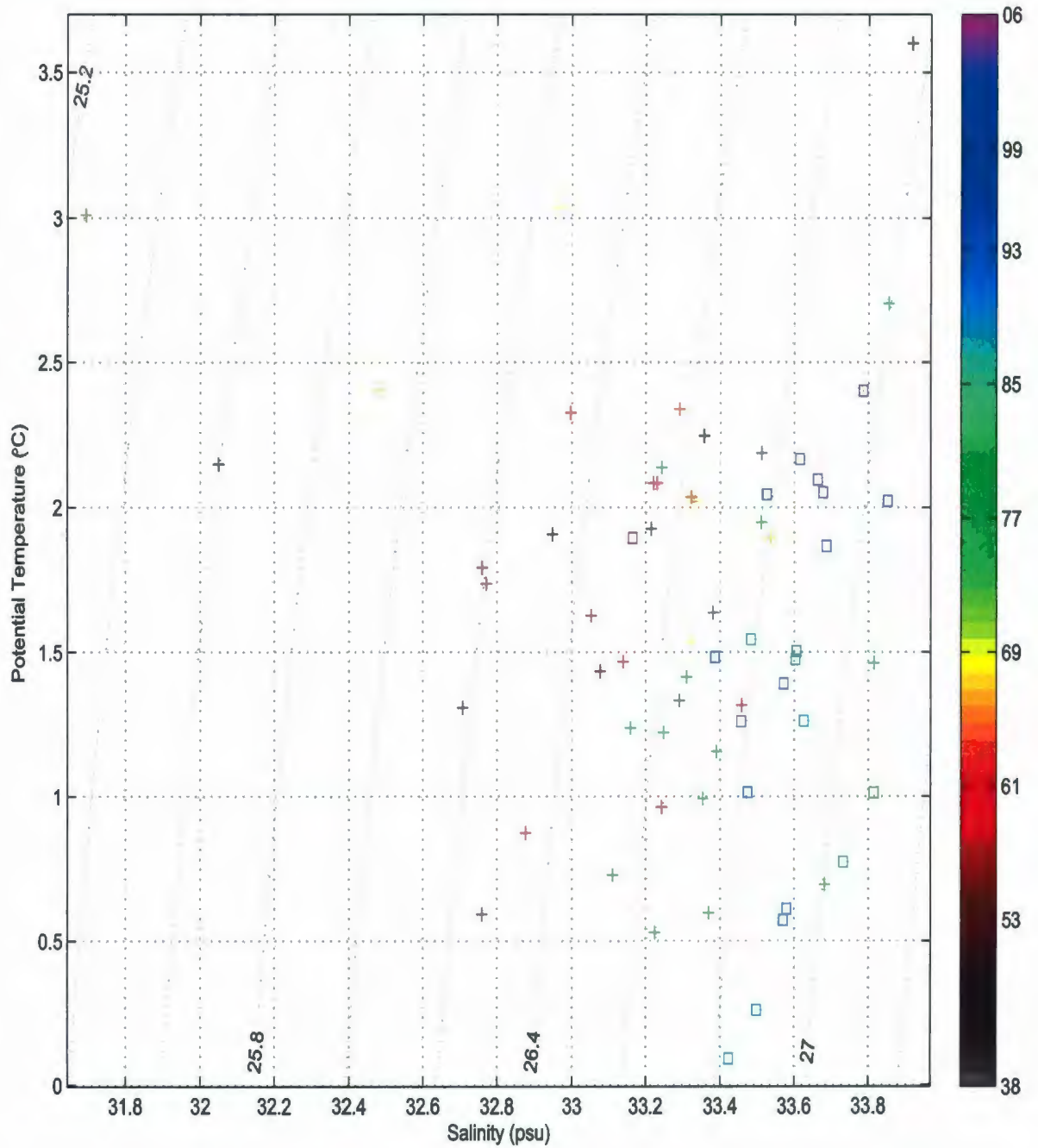


Figure .6. Surface layer annual mean potential temperature and salinity distribution in the LC where +'s and □'s are annual means during 1938-84 and 1985-06 respectively. No data exists in 1942-45 and 1947.

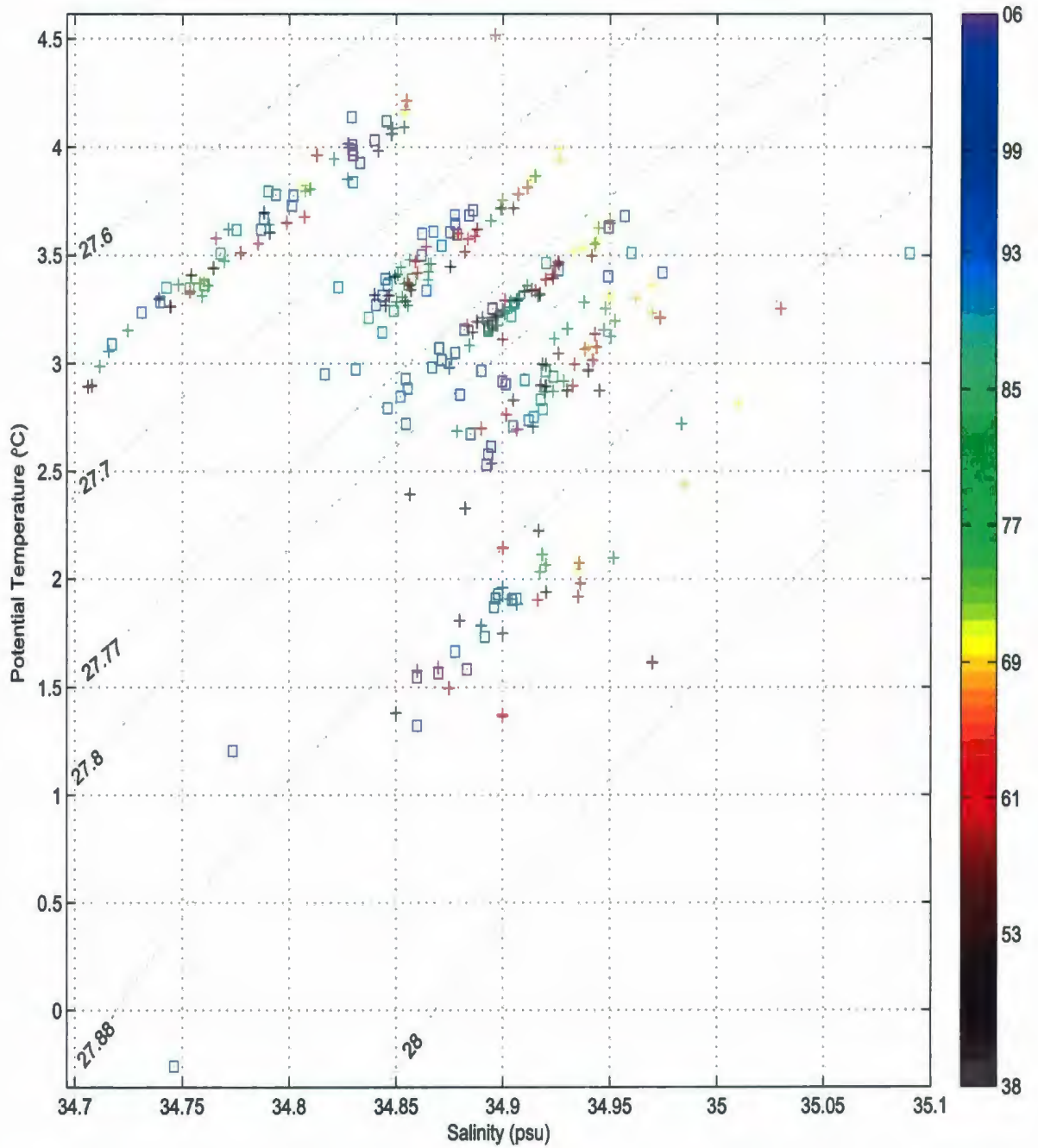


Figure .7. Annual mean potential temperature and salinity distributions in the LC for the subsurface water masses. +'s and □'s are annual means during 1938-84 and 1985-06 respectively. In 1939-45 and 1947 there is no data for all water masses while some water masses also do not have data in other years.

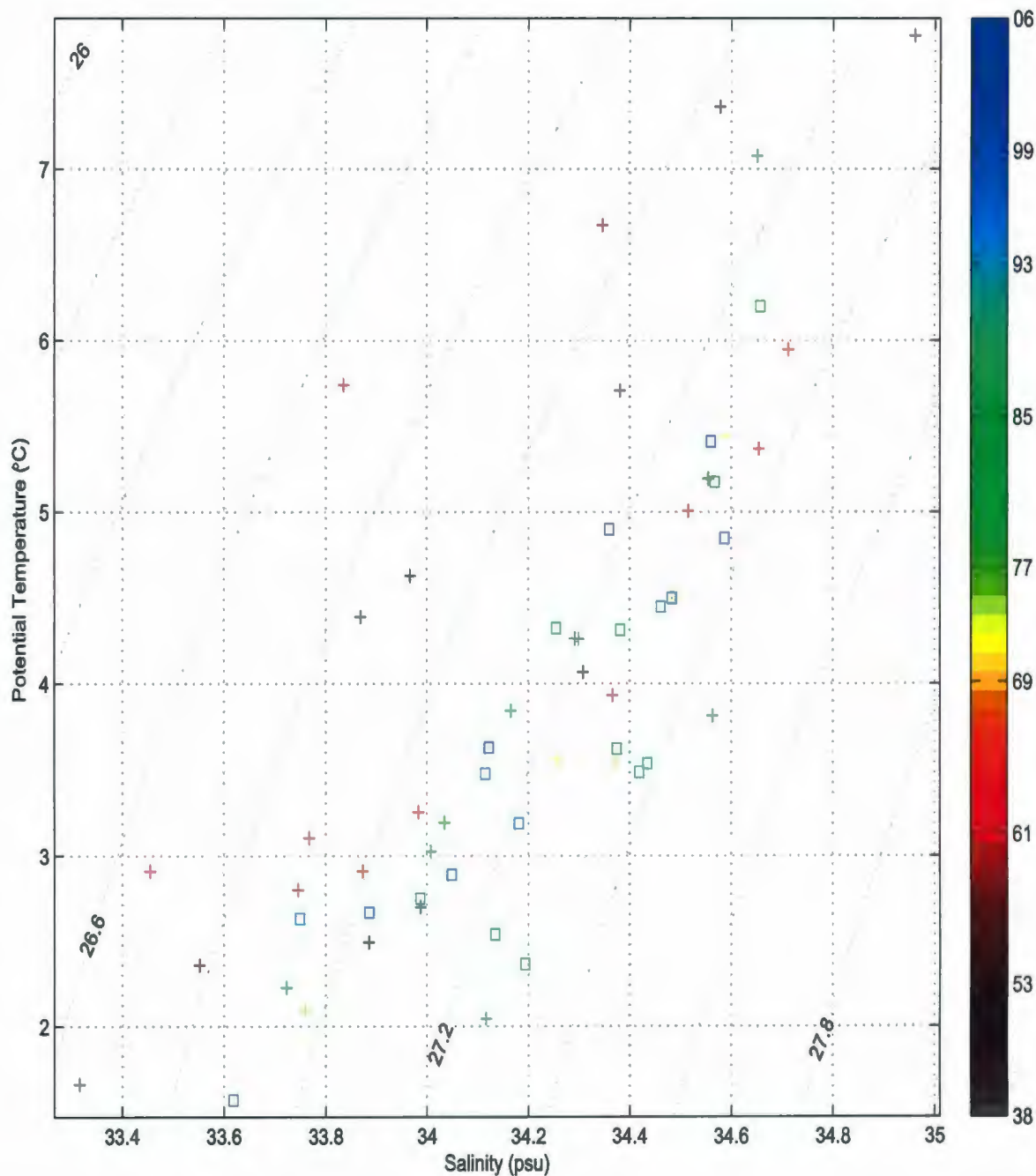


Figure .8. Surface layer annual mean potential temperature and salinity distribution in the SELS where +’s and □’s are annual means during 1938-84 and 1985-06 respectively. No data exists in 1938-40, 1942-46, 1949 and 1975-76.

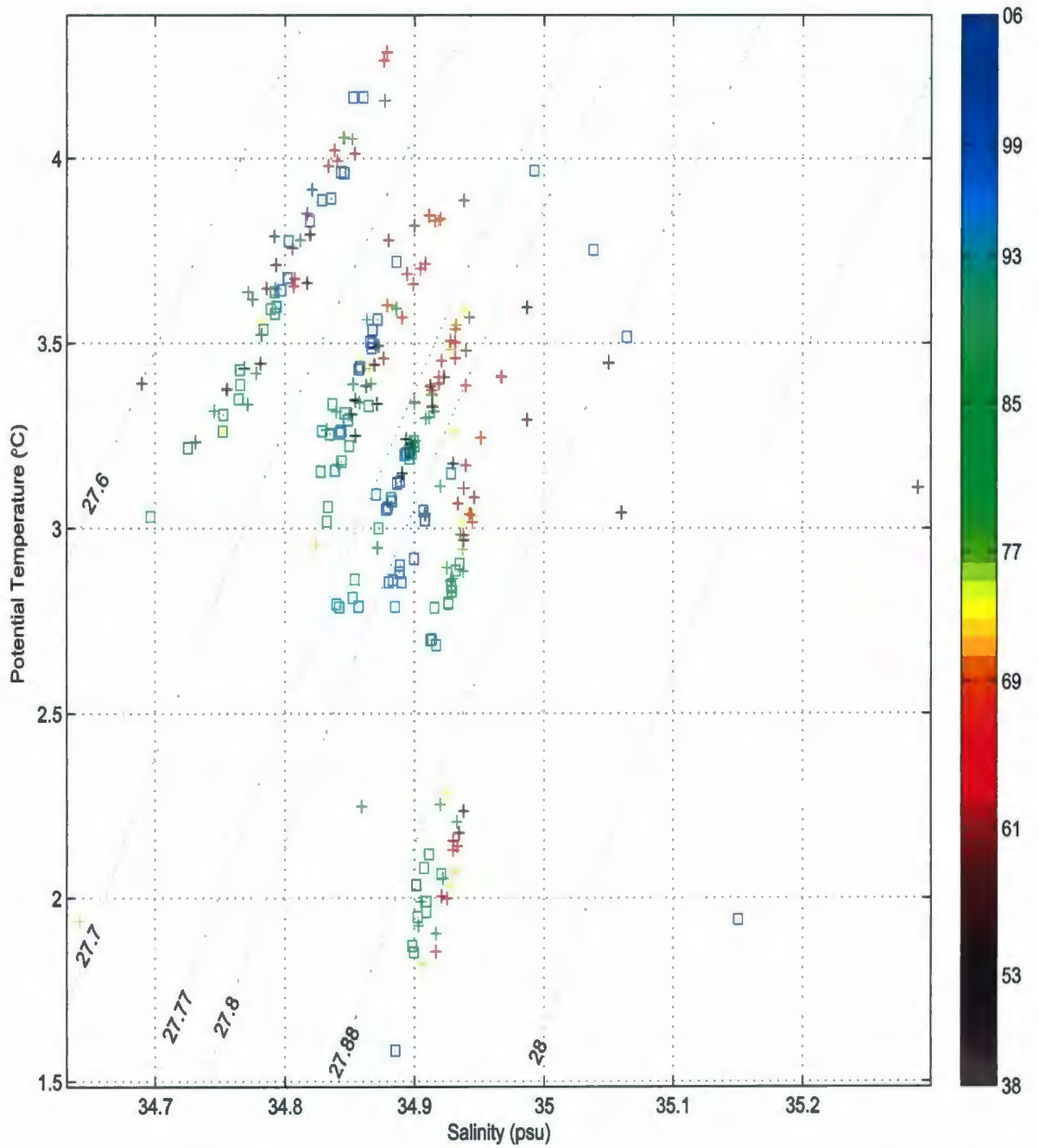


Figure .9. Annual mean potential temperature and salinity distributions in the SELS for the subsurface water masses. +'s and □'s are annual means during 1938-84 and 1985-06 respectively. In 1938-46,1949 and 1975 there is no data for all water masses while some water masses also do not have data in other years.

## Appendix

### Appendix C: Standard Deviation of Anomalies

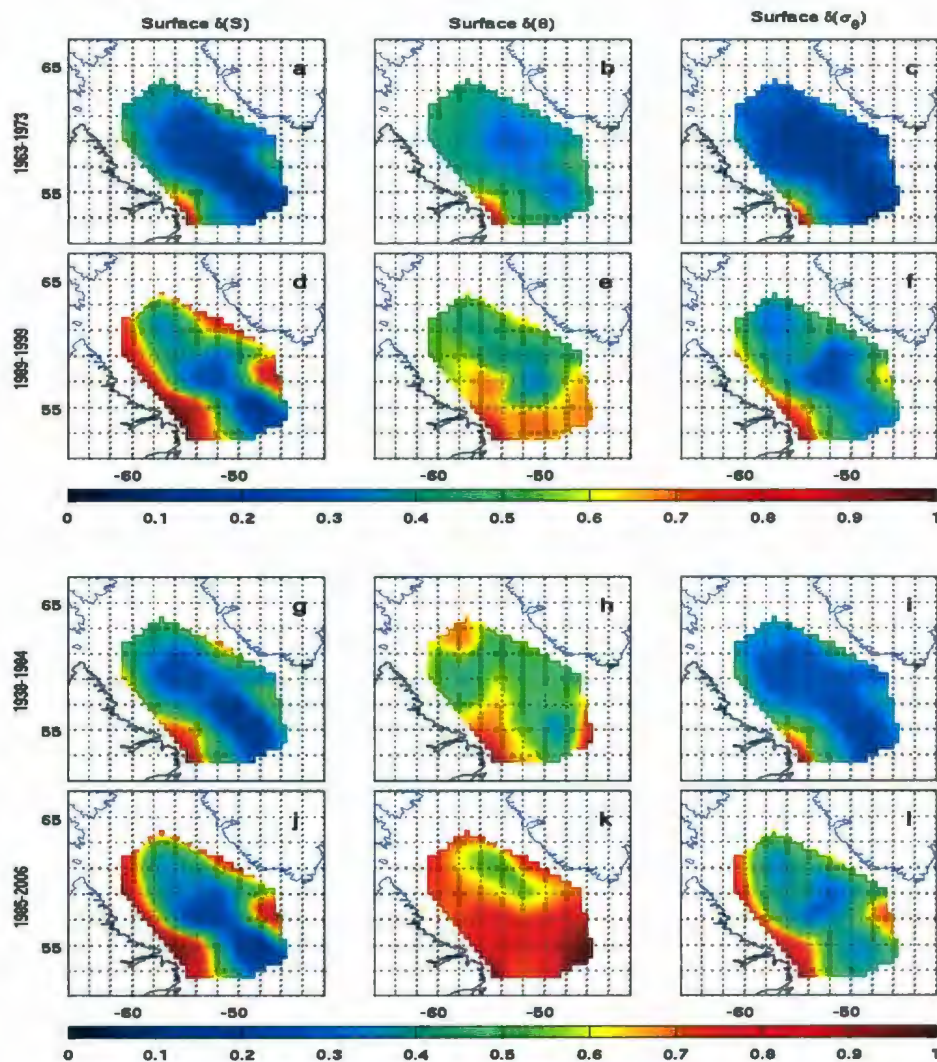


Figure .1. Standard deviation ( $\delta$ ) of surface layer anomalies for salinity (first column), potential temperature (second column) and potential density (third column). The time periods are 1963-1973 (first row), 1989-1999 (second row), 1938-1984 (third row), and 1985-2006 (fourth row). Each  $\delta$  map has been normalized by its maximum value.

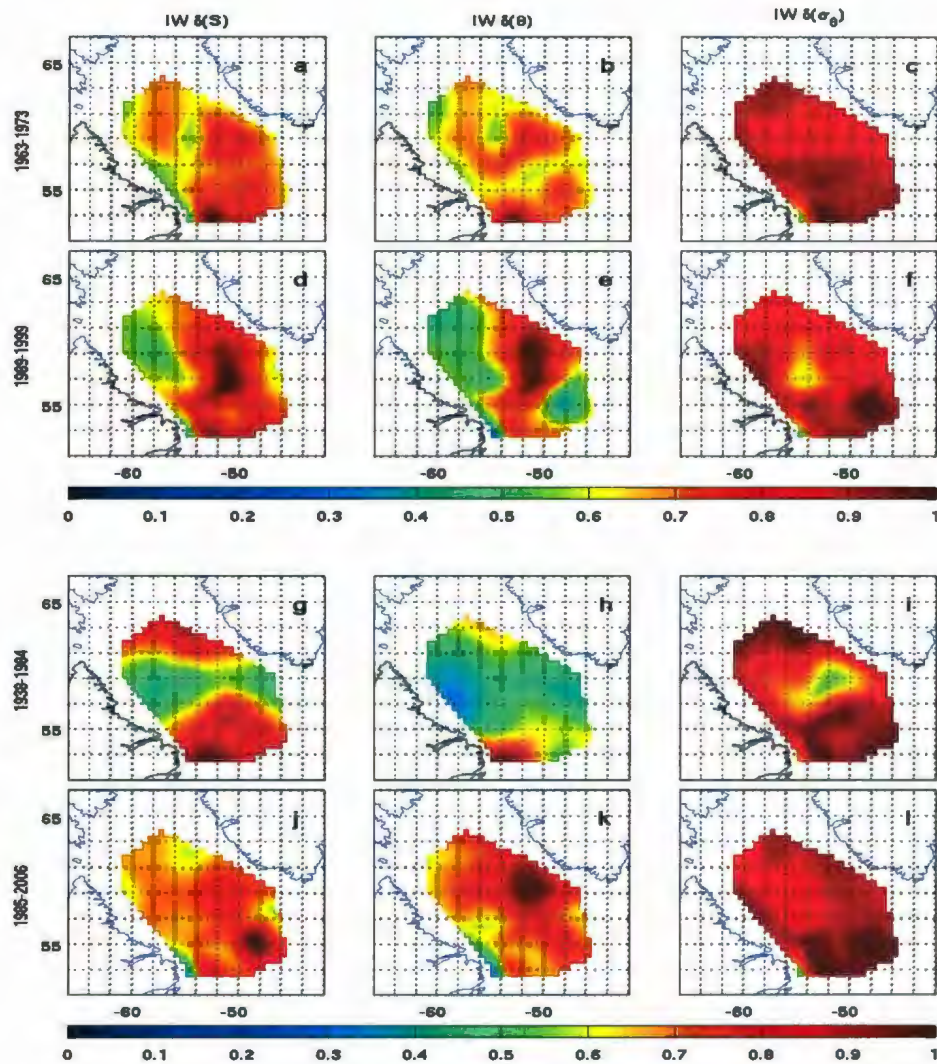


Figure .2. Standard deviation ( $\delta$ ) of IW layer anomalies for salinity (first column), potential temperature (second column) and potential density (third column). The time periods are 1963-1973 (first row), 1989-1999 (second row), 1938-1984 (third row), and 1985-2006 (fourth row). Each  $\delta$  map has been normalized by its maximum value.

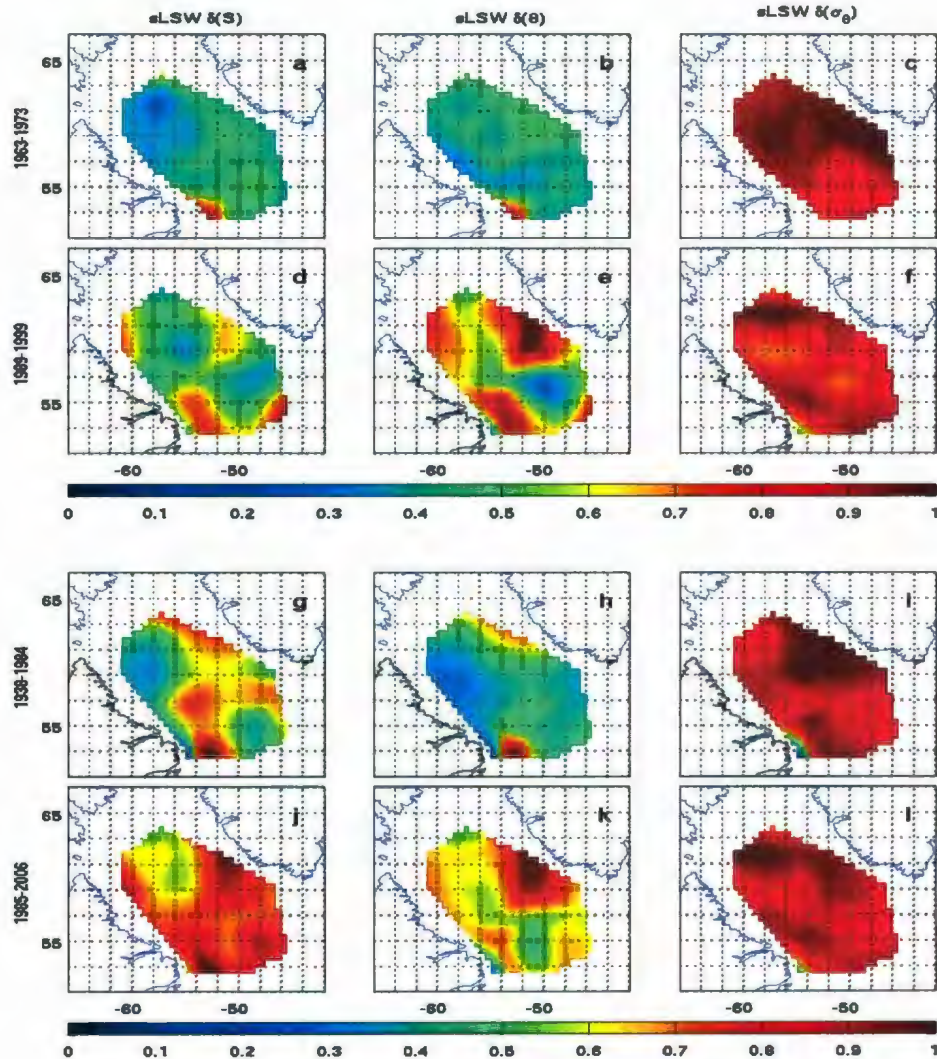


Figure .3. Standard deviation ( $\delta$ ) of sLSW layer anomalies for salinity (first column), potential temperature (second column) and potential density (third column). The time periods are 1963-1973 (first row), 1989-1999 (second row), 1938-1984 (third row), and 1985-2006 (fourth row). Each  $\delta$  map has been normalized by its maximum value.

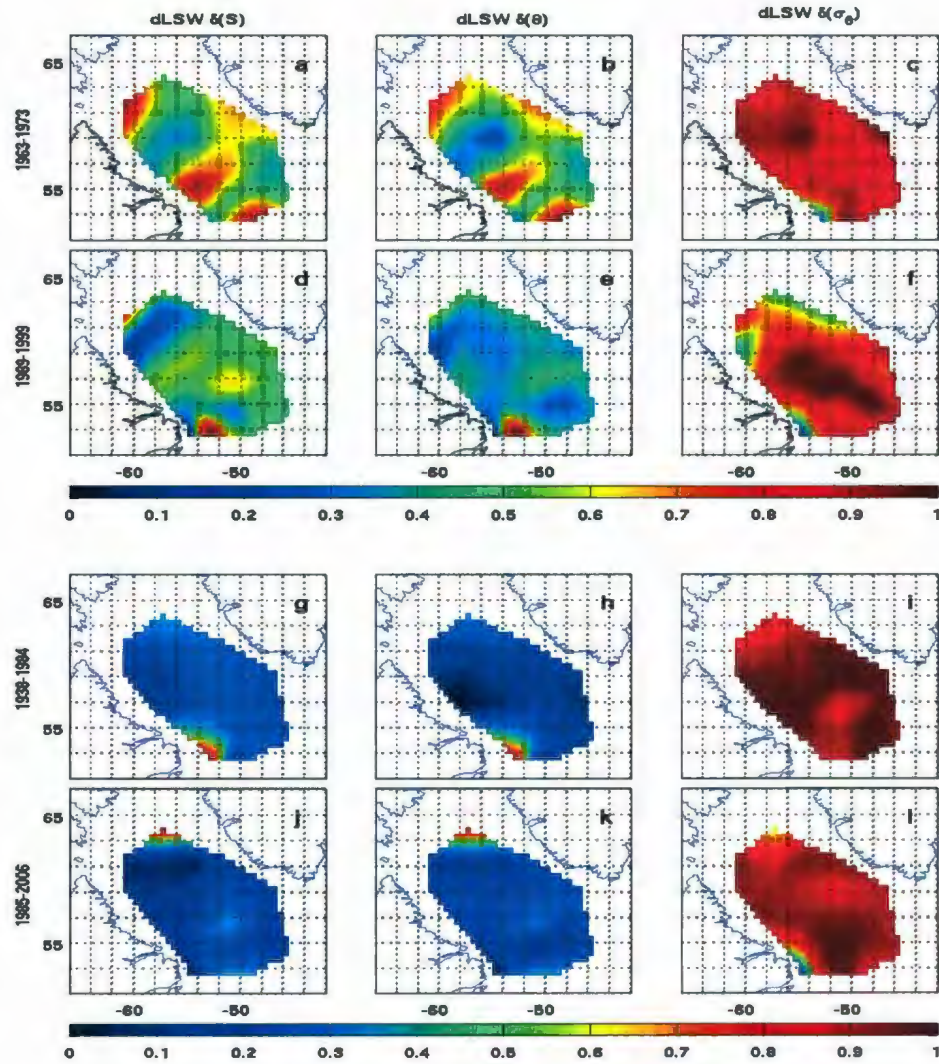


Figure 4. Standard deviation ( $\delta$ ) of dLSW layer anomalies for salinity (first column), potential temperature (second column) and potential density (third column). The time periods are 1963-1973 (first row), 1989-1999 (second row), 1938-1984 (third row), and 1985-2006 (fourth row). Each  $\delta$  map has been normalized by its maximum value.

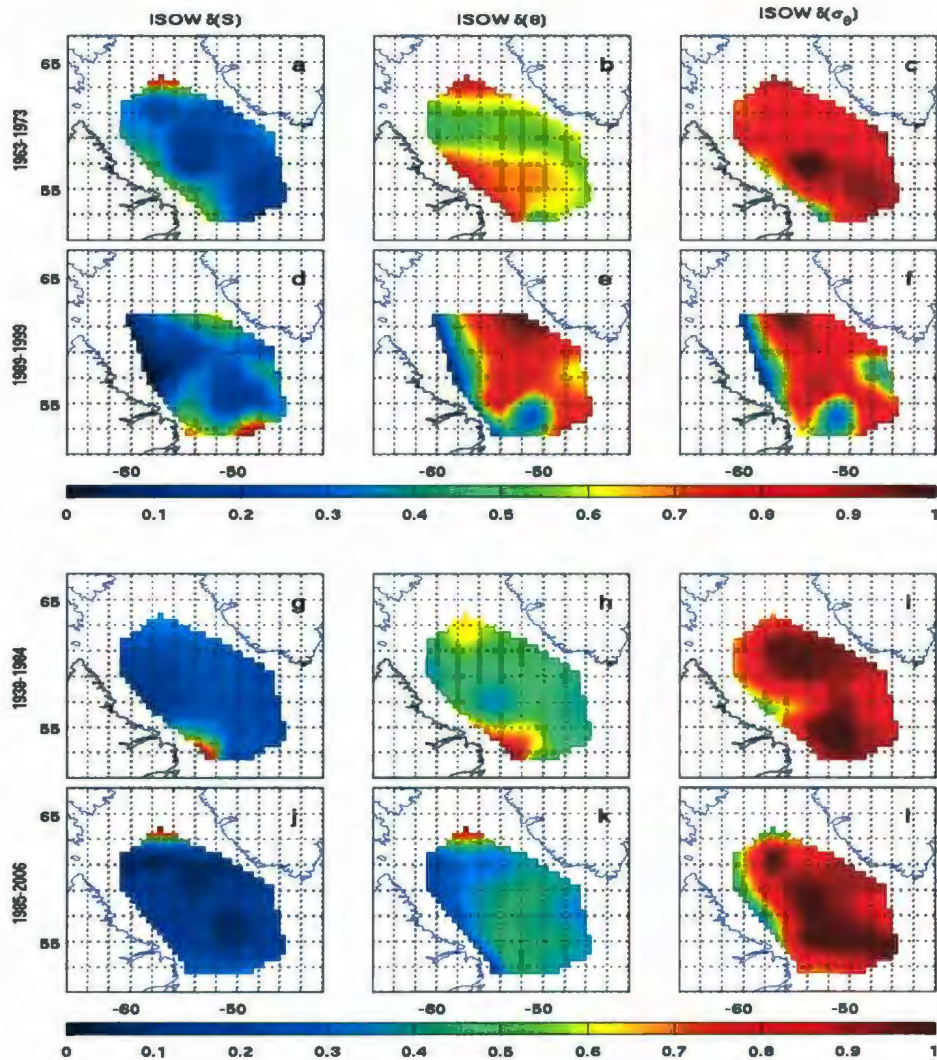


Figure .5. Standard deviation ( $\delta$ ) of ISOW layer anomalies for salinity (first column), potential temperature (second column) and potential density (third column). The time periods are 1963-1973 (first row), 1989-1999 (second row), 1938-1984 (third row), and 1985-2006 (fourth row). Each  $\delta$  map has been normalized by its maximum value.

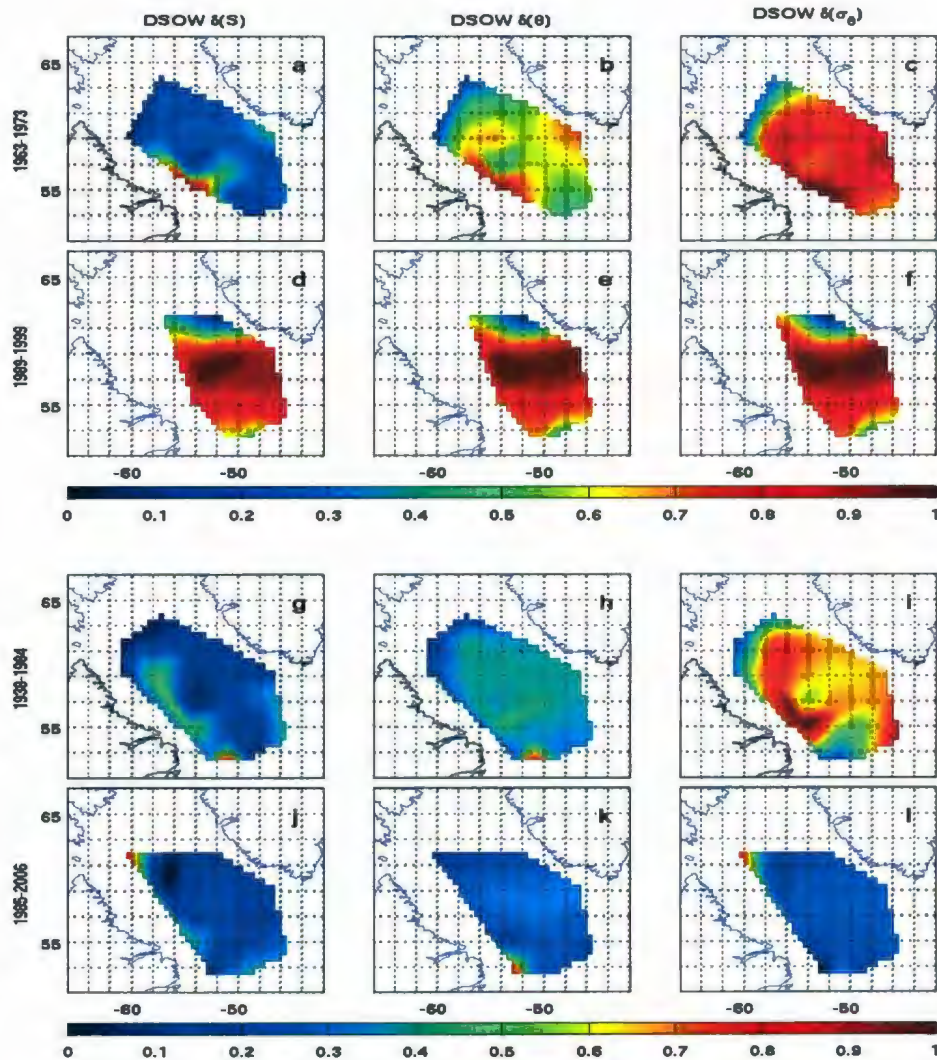


Figure .6. Standard deviation ( $\delta$ ) of DSOW layer anomalies for salinity (first column), potential temperature (second column) and potential density (third column). The time periods are 1963-1973 (first row), 1989-1999 (second row), 1938-1984 (third row), and 1985-2006 (fourth row). Each  $\delta$  map has been normalized by its maximum value.

	Normalized $\delta$	1963-73			Normalized $\delta$	1989-99		
		$\delta(S)$ (psu)	$\delta(\theta)$ ( $^{\circ}C$ )	$\delta(\sigma_{\theta})$ ( $kg/m^3$ )		$\delta(S)$ (psu)	$\delta(\theta)$ ( $^{\circ}C$ )	$\delta(\sigma_{\theta})$ ( $kg/m^3$ )
Surface	0	0.1585	1.1782	0.1736	0	0.1124	0.8293	0.1866
	1	1.6506	4.2836	1.6289	1	0.8958	2.4949	0.8680
IW	0	0.0360	0.3603	0.0130	0	0.0178	0.0682	0.0122
	1	0.1034	0.7523	0.0309	1	0.0594	0.4918	0.0314
sLSW	0	0.0183	0.1969	0.0148	0	0.0114	0.0654	0.0094
	1	0.0710	0.6737	0.0219	1	0.0340	0.3098	0.0203
dLSW	0	0.0096	0.0518	0.0020	0	0.0000	0.0000	0.0000
	1	0.0298	0.2338	0.0092	1	0.0388	0.3131	0.0093
ISOW	0	0.0061	0.1821	0.0079	0	-0.0006	0.0000	0.0000
	1	0.0542	0.4452	0.0275	1	0.0300	0.3101	0.0268
DSOW	0	0.0000	0.0000	0.0000	0	0.0000	0.0000	0.0000
	1	0.0542	0.5894	0.0250	1	0.0139	0.3598	0.0177

Table .1. Maximum and minimum 1963-1973 and 1989-1999 standard deviation of  $S$ ,  $\theta$  and  $\sigma_{\theta}$  anomalies corresponding to the normalized standard deviation extrema.

	Normalized $\sigma$	1938-84			Normalized $\sigma$	1985-06		
		$\sigma(S)$ (psu)	$\sigma(\theta)$ ( $^{\circ}\text{C}$ )	$\sigma(\sigma_{\theta})$ ( $\text{kg}/\text{m}^3$ )		$\sigma(S)$ (psu)	$\sigma(\theta)$ ( $^{\circ}\text{C}$ )	$\sigma(\sigma_{\theta})$ ( $\text{kg}/\text{m}^3$ )
Surface	0	0.1533	1.0641	0.2007	0	0.0932	1.0580	0.1940
	1	1.2759	3.0251	1.2239	1	0.8651	1.9802	0.7219
IW	0	0.0341	0.2275	0.0156	0	0.0176	0.0674	0.0120
	1	0.0820	0.7884	0.0296	1	0.0644	0.4547	0.0298
sLSW	0	0.0000	0.0000	0.0000	0	0.0133	0.0654	0.0094
	1	0.0509	0.5271	0.0211	1	0.0265	0.3382	0.0205
dLSW	0	0.0084	0.0149	0.0073	0	0.0000	0.0000	0.0000
	1	0.0829	0.7927	0.0092	1	0.0846	0.6187	0.0092
ISOW	0	0.0084	0.1813	0.0118	0	0.0040	0.0297	0.0070
	1	0.0829	0.5319	0.0252	1	0.0789	0.5985	0.0242
DSOW	0	0.0000	0.0246	0.0020	0	0.0000	0.0717	0.0000
	1	0.0960	0.8440	0.0278	1	0.0603	1.0917	0.0636

Table .2. Maximum and minimum 1938-1984 and 1985-2006 standard deviation of  $S$ ,  $\theta$  and  $\sigma_{\theta}$  anomalies corresponding to the normalized standard deviation extrema.

## Appendix

### Appendix D: Skewness of Anomalies

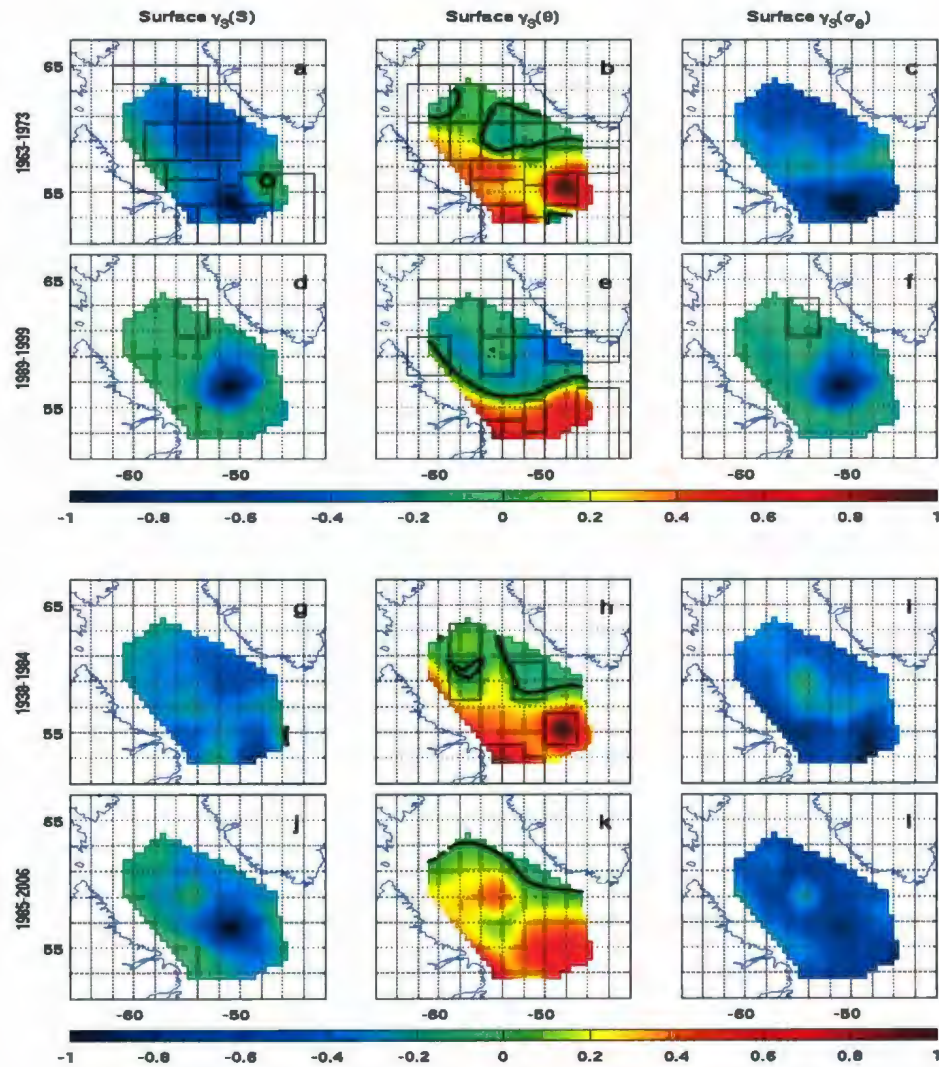


Figure .1. Skewness ( $\gamma_3$ ) of surface layer anomalies for salinity (first column), potential temperature (second column) and potential density (third column). The time periods are 1963-1973 (first row), 1989-1999 (second row), 1938-1984 (third row), and 1985-2006 (fourth row). Each  $\gamma_3$  map has been normalized by its maximum value. Zero contours are thickened black lines. Regions in which the skew is statistically not significantly different from zero are outlined.

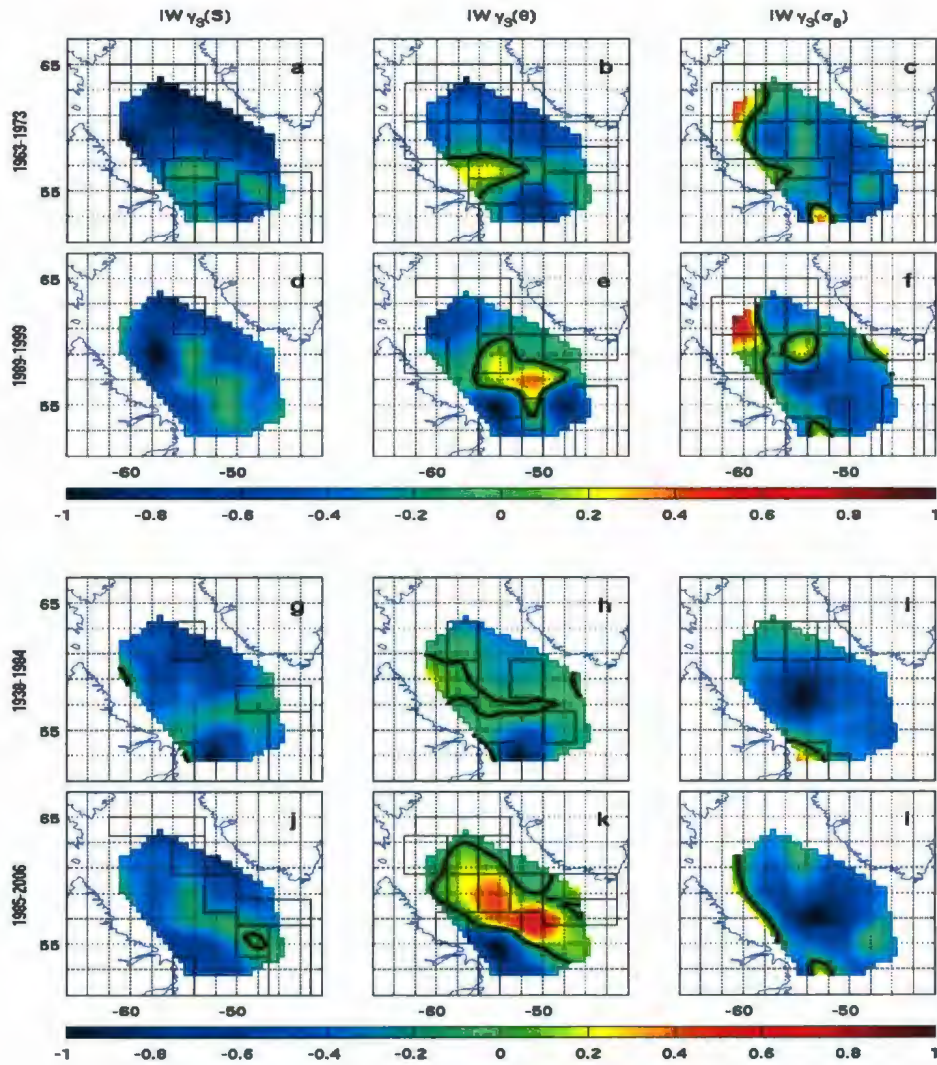


Figure .2. Skewness ( $\gamma_3$ ) of IW layer anomalies for salinity (first column), potential temperature (second column) and potential density (third column). The time periods are 1963-1973 (first row), 1989-1999 (second row), 1938-1984 (third row), and 1985-2006 (fourth row). Each  $\gamma_3$  map has been normalized by its maximum value. Zero contours are thickened black lines. Regions in which the skew is statistically not significantly different from zero are outlined.

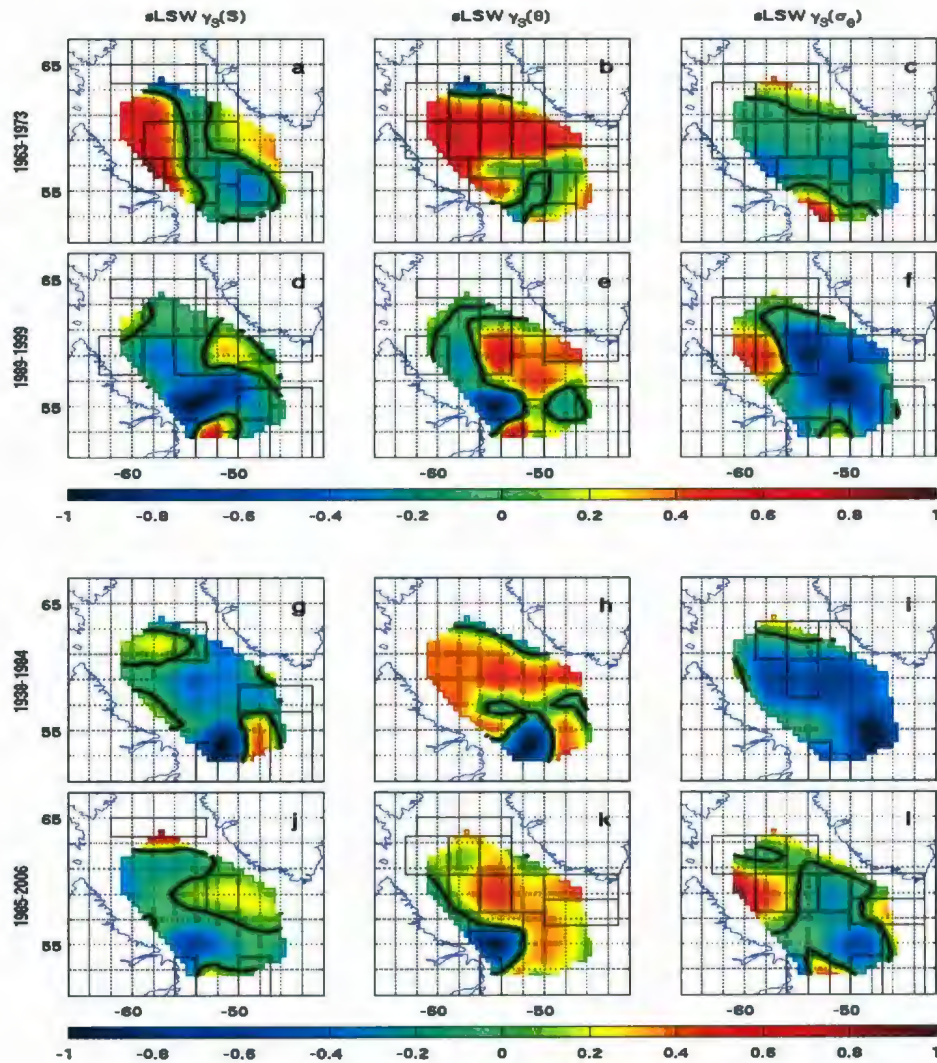


Figure .3. Skewness ( $\gamma_3$ ) of sLSW layer anomalies for salinity (first column), potential temperature (second column) and potential density (third column). The time periods are 1963-1973 (first row), 1989-1999 (second row), 1938-1984 (third row), and 1985-2006 (fourth row). Each  $\gamma_3$  map has been normalized by its maximum value. Zero contours are thickened black lines. Regions in which the skew is statistically not significantly different from zero are outlined.

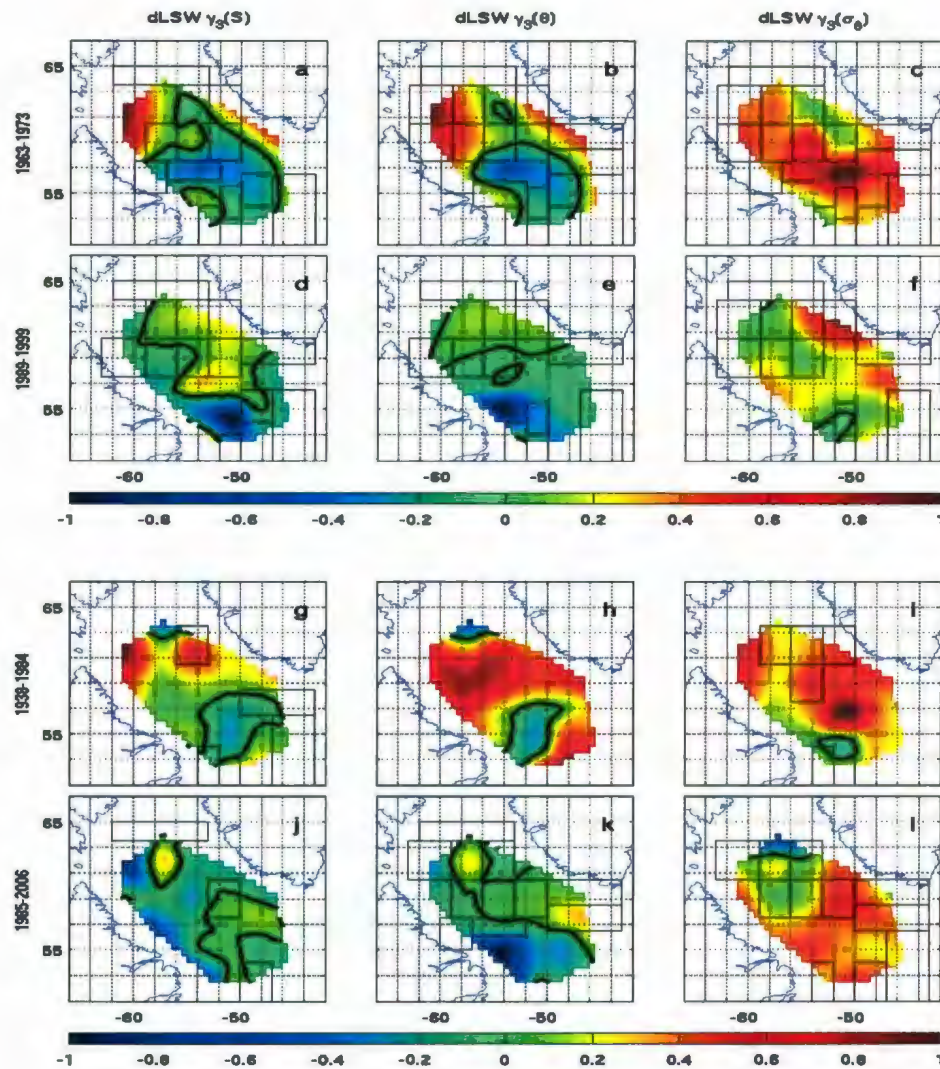


Figure .4. Skewness ( $\gamma_3$ ) of dLSW layer anomalies for salinity (first column), potential temperature (second column) and potential density (third column). The time periods are 1963-1973 (first row), 1989-1999 (second row), 1938-1984 (third row), and 1985-2006 (fourth row). Each  $\gamma_3$  map has been normalized by its maximum value. Zero contours are thickened black lines. Regions in which the skew is statistically not significantly different from zero are outlined.

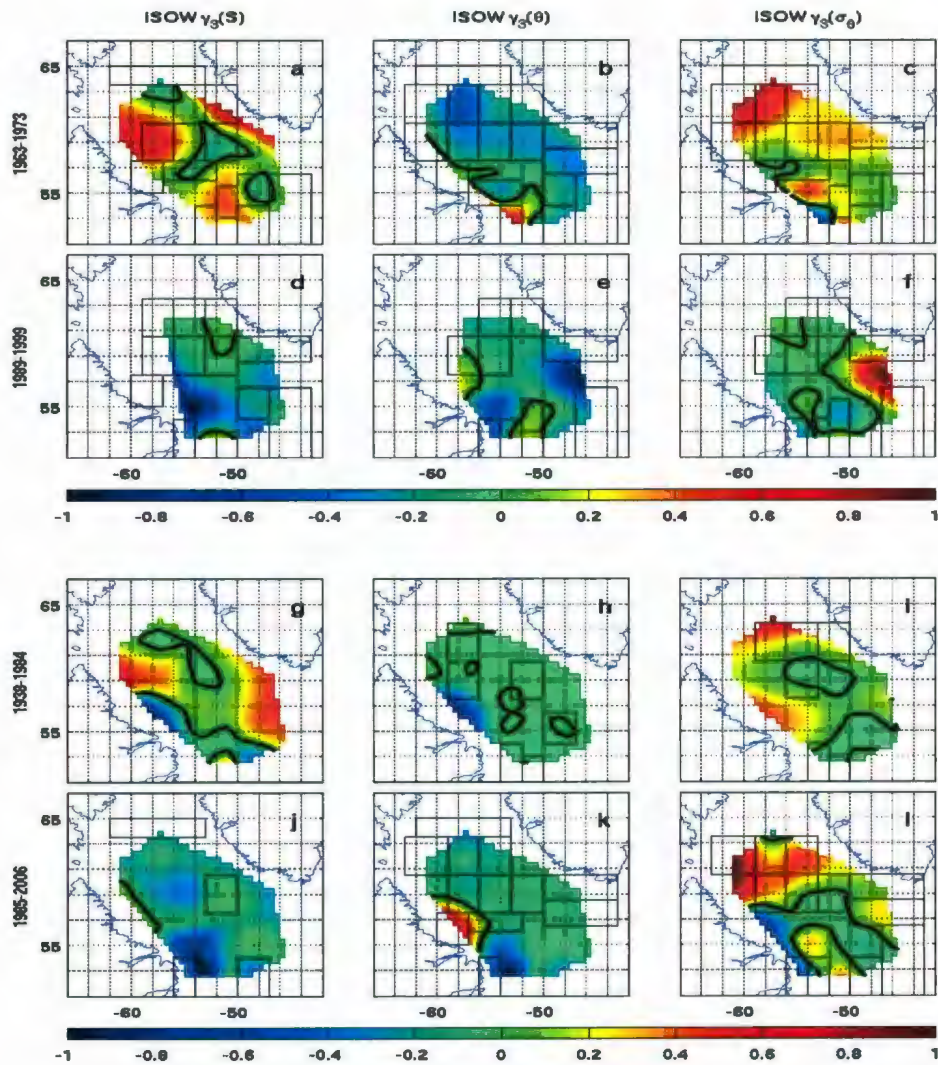


Figure .5. Skewness ( $\gamma_3$ ) of ISOW layer anomalies for salinity (first column), potential temperature (second column) and potential density (third column). The time periods are 1963-1973 (first row), 1989-1999 (second row), 1938-1984 (third row), and 1985-2006 (fourth row). Each  $\gamma_3$  map has been normalized by its maximum value. Zero contours are thickened black lines. Regions in which the skew is statistically not significantly different from zero are outlined.

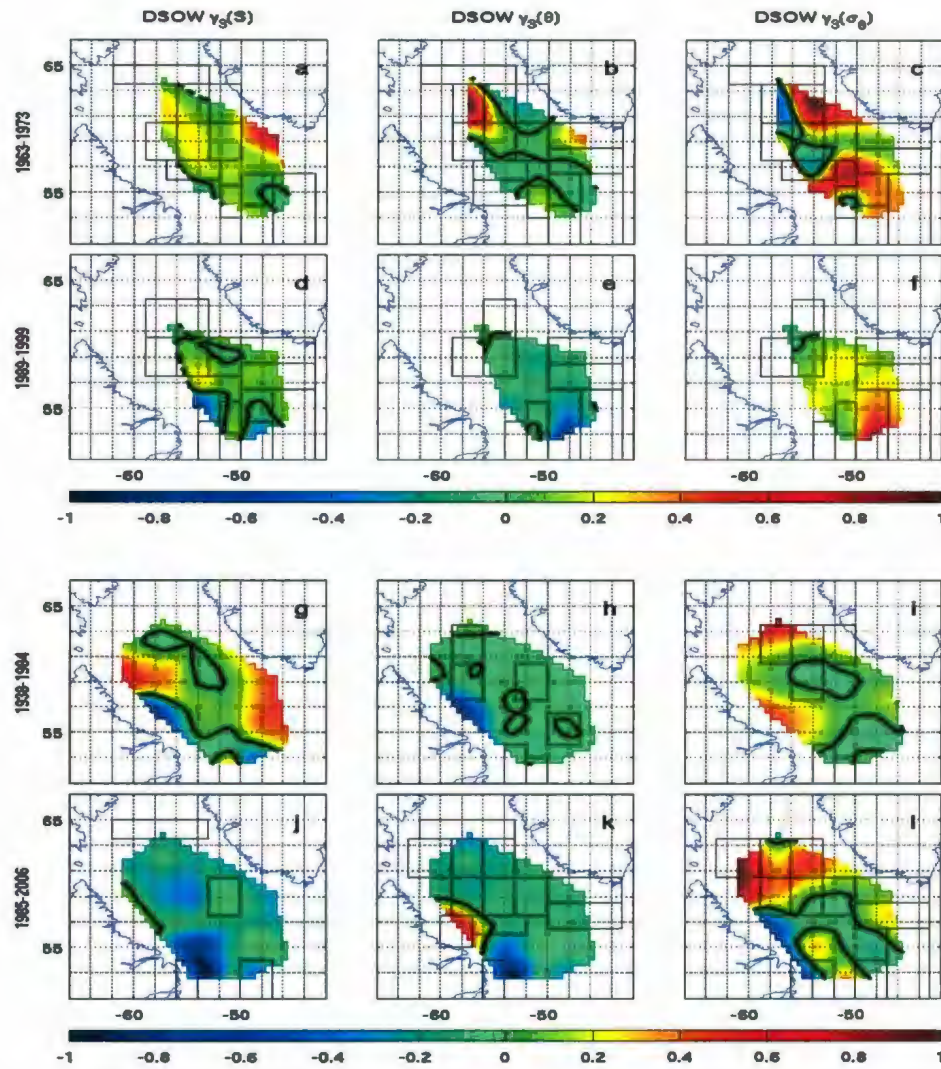


Figure .6. Skewness ( $\gamma_3$ ) of DSO layer anomalies for salinity (first column), potential temperature (second column) and potential density (third column). The time periods are 1963-1973 (first row), 1989-1999 (second row), 1938-1984 (third row), and 1985-2006 (fourth row). Each  $\gamma_3$  map has been normalized by its maximum value. Zero contours are thickened black lines. Regions in which the skew is statistically not significantly different from zero are outlined.

## Appendices

	Normalized $\gamma_3$	1963-73			Normalized $\gamma_3$	1989-99		
		$\gamma_3(S)$	$\gamma_3(\theta)$	$\gamma_3(\sigma_\theta)$		$\gamma_3(S)$	$\gamma_3(\theta)$	$\gamma_3(\sigma_\theta)$
Surface	-1	-2.3737	-0.6538	-2.2389	-1	-8.7765	-0.9575	-6.7082
	1	0.0331	1.9951	-0.2283	1	-0.0539	1.7239	-0.2272
IW	-1	-1.6138	-1.8086	-0.7713	-1	-2.2799	-1.5297	-0.8655
	1	-0.0073	0.4577	0.4520	1	-0.0779	0.5846	1.0208
sLSW	-1	-1.5630	-1.1330	-0.5081	-1	-2.9761	-2.5738	-1.4955
	1	1.8176	0.8731	1.0044	1	2.0928	2.2955	0.7918
dLSW	-1	-1.5246	-1.5261	0.0000	-1	-2.8197	-5.9205	-0.3633
	1	3.4145	2.8272	1.0184	1	1.0046	1.0777	3.4712
ISOW	-1	-1.1030	-0.6718	-1.1547	-1	-5.9060	-2.6527	-1.1308
	1	4.5487	1.1547	1.0332	1	1.8535	0.6425	2.6836
DSOW	-1	-0.7793	-0.3911	-0.6620	-1	-2.1981	-1.8536	-0.3903
	1	3.1230	1.3775	1.0098	1	0.5739	0.1547	1.5495

Table .1. Maximum and minimum 1963-1973 and 1989-1999 skewness of  $S$ ,  $\theta$  and  $\sigma_\theta$  anomalies corresponding to the normalized skewness extrema.

	Normalized $\gamma_3$	1938-84			Normalized $\gamma_3$	1985-06		
		$\gamma_3(S)$	$\gamma_3(\theta)$	$\gamma_3(\sigma_\theta)$		$\gamma_3(S)$	$\gamma_3(\theta)$	$\gamma_3(\sigma_\theta)$
Surface	-1	-3.7658	-0.2540	-2.8144	-1	-6.1048	-0.4572	-2.3704
	1	0.1507	1.6533	-0.3668	1	-0.0315	2.0358	-0.3413
IW	-1	-1.6549	-3.1973	-1.1388	-1	-1.6807	-1.1973	-0.7515
	1	0.2980	0.8270	0.4632	1	0.0566	0.8165	0.2732
sLSW	-1	-2.3515	-2.3708	-0.7206	-1	-1.6154	-1.7745	-0.6249
	1	1.1102	1.7618	0.2706	1	2.5447	0.9411	0.9008
dLSW	-1	-2.6008	-3.3880	-0.1502	-1	-2.9922	-2.5803	-0.9239
	1	3.7662	3.5831	0.8439	1	0.8689	0.8806	0.5982
ISOW	-1	-7.7141	-10.2537	-0.1851	-1	-5.8964	-3.5601	-1.1308
	1	5.3262	1.3686	1.5376	1	1.0668	2.9965	1.1737
DSOW	-1	-1.5113	-0.7274	-0.8642	-1	-6.2694	-2.2247	-1.9756
	1	12.2895	0.8603	14.4368	1	3.7745	1.9913	3.9230

Table .2. Maximum and minimum 1938-1984 and 1985-2006 skewness of  $S$ ,  $\theta$  and  $\sigma_\theta$  anomalies corresponding to the normalized skewness extrema.





